DEFORMATION MEASUREMENTS OF 3D PRINTED LATTICE-STRUCTURED MATERIALS THROUGH IMAGE ANALYSIS

By

Ebsana Saria

Thesis submitted for the degree of
Master of Science by Research and Thesis



Mechanical Engineering, School of Engineering,
University of Kent,
Canterbury,
CT2 7NT,
United Kingdom

January 2025

Abstract

Measuring the deformation under loading conditions is a crucial part of any material characterization. Image analysis is a robust technology that determines the full-field deformation of a structure without interfering with its properties. These measurements are significantly challenging for lattice-structured materials due to the detailed geometries involved in the region of measurements. Furthermore, despite the advancements in Digital Image Correlation (DIC) techniques, there is a need for comprehensive performance analysis of different DIC software and alternative deformation measurement model development for complex geometric materials such as 3D-printed lattice-structured materials. Therefore, this research aims to investigate the deformation measurement of 3D-printed lattice-structured materials under compressive load using advanced image analysis techniques through validation and comparison of results.

This study encompasses the performance analysis of a well-known commercial DIC software, an open-source DIC software, and a proposed Imaging Technique-based deformation analysis model for the full-field deformation measurement of 3D-printed lattice-structured materials. The results obtained from these techniques are compared with Finite Element simulations to validate their accuracy. The study also incorporates image segmentation for pre-processing images to improve the results. Five lattice types (Cubic, FCC, FCCZ, BCC and BCCZ) fabricated from PLA and TPU materials have been used to analyse their mechanical response under compressive loading.

Results demonstrate that DIC analysis accurately portrays each material's unique deformation pattern. The commercial DIC software is efficient with a 7% deviation from the testing machine data for deformation in the Y direction, while the proposed Imaging Technique-based model shows a 6% deviation. In addition, the performance of the open-source DIC software improves after incorporating pre-processed images. This research also investigates the influence of several factors on the results, including speckle pattern on the surface, image resolution, background information, and illumination.

This research establishes a unique dataset for lattice-structure deformation analysis and demonstrates the effectiveness of image-based measurement techniques for complex geometric materials. The findings highlight the potential of advanced image analysis techniques in

improving the accuracy of deformation measurements and contribute to the development of more reliable and efficient DIC methods.

Keywords: Additive Manufacturing, Lattice-structured Material, Digital Image Correlation, Image Analysis, Finite Element Analysis, Deformation Measurement.

Acknowledgements

The author acknowledges her heartfelt gratitude towards Dr. Amir Hosein Sakhaei for his unwavering support, patience and knowledge throughout the research period. His invaluable cooperation, continuous guidance and encouragement at every level are gratefully recognized. The author feels greatly privileged to have completed this MSc by research under his guidance.

The acknowledgement is extended to Dr. Sajid Rafiq for his support, advice and encouragement. The author is also thankful to Dr. Sanaul Hoque, the chair of the review panel, for his insightful feedback and constructive critiques.

Sincere thanks go to the members of the University of Kent's Mechanical research group, the technical service team and fellow students, whose time, help and expertise were crucial in completing the experiment and research.

Finally, the author would like to thank her wonderful parents and sister for their inspiration and blessings at every step of the way. She is deeply indebted to her husband for his invaluable support, care, and academic contribution amid the challenges of his own PhD journey. The constant motivation and love from her friends and peers have also been instrumental in her success.

Ebsana Saria, January 2025.

Table of Contents

Abstract i

Acknowledgements iii

Table of contents iv

List of Figures viii

List of Tables xi

Chapter 1: Introduction 1

1.1 3D-printed Lattice-structured Materials 1

1.2 Deformation Analysis of Materials 2

1.3 Aim and Objectives of the Research 5

1.4 Research Contribution 6

Chapter 2: Literature Review 8

2.1 Lattice-structured Materials 8

2.2 Deformation Measurement Techniques for Materials 10

2.2.1 Contact Methods 10

2.2.2 Non-Contact Optical Methods 11

2.2.3 Moiré Method 12

2.2.4 Multi-point Pattern Matching 13

2.2.5 Photogrammetry 14

2.3 Digital Image Correlation (DIC) 17

2.3.1 2D DIC Technique 18

2.4 DIC for Lattice Structures 23

2.4.1 DIC Analysis with Segmentation on Lattice Structures 25

2.5 Digital Image Correlation and Finite Element Analysis 26

2.6 Conclusion 28

Chapter 3: Technical Approach 30

3.1 Methodology 30
3.2 DIC Concept 31
3.2.1 Shape Function 33
3.2.2 Correlation Criterion 34
3.2.3 Interpolation 36
3.2.4 Local and Global DIC 36
3.3 Verification of DIC framework 37
3.4 Design of the Sample 38
3.5 Additive Manufacturing of Lattice-structured Materials 41
3.5.1 Simple Cubic Grid Lattice with Cylindrical Struts 41
3.5.2 Simple Cubic Grid Lattices with Square Cross-sectional Struts 42
3.5.3 Face Centred Cubic (FCC) and FCC Reinforced (FCCZ) Lattices 43
3.5.4 BCC, BCCZ, FCC and FCCZ Lattices 44
3.5.5 Speckle Pattern 46
3.6 Compression Test Setup 48
3.7 Image Acquisition 51
3.7.1 Camera Specifications 51
3.7.2 Minimizing Reflection 53
3.7.3 Pre-processing of Images 55
3.7.3.1 Greyscale Conversion and ROI Identification 55
3.7.3.2 Background Subtraction 57
3.8 Finite Element Analysis (FEA) 58
3.9 Conclusion 60
Chapter 4: Deformation Measurement through Image Analysis Techniques 61
4.1 DIC with Open-Source Software 61
4.1.1 Background Subtraction in DIC with Ncorr 63
4.2 DIC with Commercial Software 66
4.2.1 Performance Evaluation of the Software 67

4.3 Calculation of Deformation through Imaging Technique 70
4.3.1 Fixed-Points-Based Deformation Analysis 70
4.3.1.1 Fixed Point Selection and Tracing 71
4.3.1.2 Deformation Calculation 73
4.3.2 All-Points-Based Deformation Analysis 75
4.3.2.1 Find All Locations 76
4.3.2.2 Deformation Calculation 77
4.4 Conclusion 79
Chapter 5: Validation and Result Comparison 81
5.1 FEA of Lattice Structures 81
5.2 Result Summary 82
5.2.1 Effects of Deformation Direction on Results 85
5.2.2 Value of Deformation at Midpoints of the Edge 87
5.2.2.1 Point Deformation in Y Direction 88
5.2.2.2 Point Deformation in X direction 91
5.2.3 Average Deformation on the Edge 93
5.2.3.1 Average Deformation in Y direction 93
5.2.3.2 Average Deformation in X direction 96
5.2.4 Poisson's Ratio 98
5.3 Effects of Speckle Pattern on Result 102
5.3.1 Deformation Analysis without Speckle Pattern 102
5.3.2 Deformation Analysis with Speckle Pattern 103
5.4 Effects of Out-of-Plane Struts 107
5.5 Effects of Cameras 110
5.6 Effects of Background and Illumination 112
5.7 Discussion 115
5.7.1 Discussion on Ncorr 115
5.7.2 Discussion on Zeiss Correlate 115
5.7.3 Discussion on Imaging Technique Model 116

5.8 Conclusion 117
Chapter 6: Conclusions and Future Work 118
6.1 Conclusions 118
6.2 Recommendations for Future Work 121
References 122
Appendices 137

List of Figures

Figure 1.1: Common unit-cell designs for AM strut-based lattices [4] 1
Figure 1.2: Schematic compression stress-strain curve of lattice structure [9] 3
Figure 2.1: Principle of sampling moiré method for measuring in-plane displacement [43] .. 12
Figure 2.2: Flowchart of vision-based displacement measurement of multiple points for Multi-point Pattern Matching Technique [44]. 14
Figure 2.3: Four steps of image registration: top row—feature detection (corners were used as the features in this case). Middle row—feature matching by invariant descriptors (the corresponding pairs are marked by numbers). Bottom left—transform model estimation exploiting the established correspondence. Bottom right—image resampling and transformation using appropriate interpolation technique [46]. 15
Figure 2.4: The imaging models, systems and applicability of three typical DIC techniques [24] 18
Figure 2.5: Step-by-step workflow of 2D DIC technique using Ncorr software [75] 20
Figure 2.6: Experiment setup of [84] with optical strain gauge incorporated with Automatic Digital Image Correlation (ADIC) technique 22
Figure 2.7: Graphical abstract of image analysis characterization of AM lattice-structured material [91] 26
Figure 3.1: Proposed methodology for deformation measurement of 3D-printed lattice-structured materials through image analysis 31
Figure 3.2:Schematic diagram of DIC technique (inspired from [39]) 32
Figure 3.3: Comparison between local DIC and global DIC [74] 36
Figure 3.4: Results from (a) py2DIC, (b) py2DIC smoothed result using Gaussian filter, (c) Ncorr, (d) Vic-2D, (e)DICe from research by [67] and (f) validation test with Ncorr in this research for deformation in Y direction (U_y). 37
Figure 3.5: Strain ε_{xy} results obtained from (a) DIC analysis in [74] using different techniques and (b) validation test with Ncorr in this research 38
Figure 3.6: 3D-printed lattice-structured samples 40
Figure 3.7: Design and prints Cubic Grid with cylindrical struts 42
Figure 3.8: Design(a)-(b) and prints(c)-(d) of Cubic Grid with square struts 43

Figure 3.9: Design(a)-(b) and prints(c)-(d) of FCC and FCCZ 44
Figure 3.10:Fusion 360 models and 3D prints for BCC, BCCZ, FCC and FCCZ 45
Figure 3.11: Speckling through spray paint 47
Figure 3.12: Speckling through marker pen 48
Figure 3.13: Universal Testing Machine Zwick Roell Z050 49
Figure 3.14: Schematic diagram of the experiment 50
Figure 3.15: The experimental setup and specimens before and after compression test (a), (c)-specimen before starting the test, (d) test setup, (b), (e)- deformed specimens after test 50
Figure 3.16: Canon EOS 850D DSLR Camera 52
Figure 3.17: Logitech C920 HD Pro Webcam 52
Figure 3.18: Tripod attached with (a) DSLR Camera and (b) Webcam 53
Figure 3.19: The approaches to minimize the light reflection during image acquisition 54
Figure 3.20: Image pre-processing flowchart 55
Figure 3.21: (a) Before and (b) after pre-processing of image 57
Figure 3.22: (a) Before and (b) after background subtraction 58
Figure 3.23: Boundary Conditions and meshed samples of different materials on FEA.....59
Figure 4.1: Ncorr Main GUI 62
Figure 4.2: Deformation in Y direction results obtained from Ncorr (without segmentation) 62
Figure 4.3: Deformation in X direction results obtained from Ncorr (without segmentation) 63
Figure 4.4: Effects of background subtraction on the U_y results of DIC analysis in NCorr....64
Figure 4.5: Zeiss Inspect Correlate GUI 66
Figure 4.6: Performance evaluation of Zeiss without segmentation for U_y.....67
Figure 4.7: Performance evaluation of Zeiss with and without segmentation for FCCZ 68
Figure 4.8: Comparison of DIC Analysis without speckle patterns.....69
Figure 4.9: Workflow of deformation analysis through Fixed Points.....70
Figure 4.10: Fixed Points for deformation analysis.....72
Figure 4.11: Flowchart of tracing all the fixed points.....73
Figure 4.12: Results of deformation analysis through Fixed Point Imaging Technique.....75
Figure 4.13: Workflow of deformation analysis through Tracing All Points.....76
Figure 4.14: Deformation matrix reconstruction 77
Figure 4.15: Deformation analysis through Imaging Technique (Tracing All Points) 78
Figure 4.16: Deformation illustration in Imaging Technique Model.....78

Figure 4.17: Comparison of U_y of Cubic sample through image analysis techniques 80
Figure 5.1: Deformation map of samples from FEA 82
Figure 5.2: Deformation in Y direction for all materials 83
Figure 5.3: Deformation in X direction for all materials 84
Figure 5.4: Selected (a) points and (b) area for deformation calculations 85
Figure 5.5: Deformed images of Cubic Grid samples 86
Figure 5.6: DIC Analysis results of U_x for Cubic Grid samples 87
Figure 5.7: Deformation in Y direction at the middle point of the top edge of samples 90
Figure 5.8: Point U_x at the midpoints of left and right vertical edges 92
Figure 5.9: Average deformation (Y direction) of different samples at the top edge 95
Figure 5.10: Average U_x at the left and right vertical edges 97
Figure 5.11: Poisson's ratio for deformation at the middle points of the sample edges 101
Figure 5.12: Poisson's ratio for average deformation along the edges of each sample 101
Figure 5.13: Deformation analysis of samples without speckle patterns 103
Figure 5.14: Deformation analysis with speckle pattern 104
Figure 5.15: Deformation map of samples with speckle pattern through Imaging Technique 106
Figure 5.16: DIC analysis in BCCZ lattice-structured materials with out-of-plane struts 108
Figure 5.17: Results of deformation analysis on samples with out of plane struts in All-Points-Model (Imaging Technique) 109
Figure 5.18: Images of Cubic Grid (TPU) samples during compression acquired through different cameras 111
Figure 5.19: U_y of Cubic Grid (PLA) sample through I.T Model 111
Figure 5.20: Deformation analysis in Imaging Technique Model of images acquired through webcam 112
Figure 5.21: Effects of background on results in Imaging Technique Model 113
Figure 5.22: Results in Imaging Technique of samples after elimination of background effect and illumination 114
Appendix Figure 1: Deformations of Cubic TPU sample using all approaches (including fixed-point model) 138

List of Tables

Table 3.1: The fundamentals of DIC....32
Table 3.2: Sampling matrix....39
Table 3.3:Camera specifications....52
Table 3.4: Image extraction and ROI identification....56
Table 5.1: Results of deformation in X and Y from Finite Element Analysis....81
Table 5.2: U_y at the midpoint of the top surface of the samples....88
Table 5.3: Deviation Percentage of U_y (Top Middle) Compared to Testing Machine....89
Table 5.4: U_x at the midpoints of left and right edge- Cubic samples....91
Table 5.5: U_x at the midpoints of left and right edge- FCC and FCCZ samples....91
Table 5.6: Average U_y at the top surface of the samples....94
Table 5.7: Deviation percentage of U_y (top surface average) compared to testing machine....94
Table 5.8: Average U_x at the left and right edge- Cubic....96
Table 5.9: Average U_x at the left and right edge- FCC and FCCZ samples....97
Table 5.10: Poisson's ratio calculated from point deformation and mean deformation....99
Table 5.11: Standard deviation of Poisson's Ratio (point and average) for all samples....100

Chapter 1: Introduction

1.1 3D-printed Lattice-structured Materials

Additive Manufacturing (AM), also known as 3D printing, has emerged as an innovative manufacturing technique for creating complex, high-value parts. It is a material-oriented manufacturing technology that can generate complex geometric structures while ensuring minimal waste and environment friendly products design. The number of industries that use AM has accelerated during the last decade [1]. The process of AM involves creating objects by adding layer-by-layer material based on 3D model data. This method stands out from traditional manufacturing techniques. This process can generate low-volume, customized and complex shaped material quickly with cost-efficiency [2].

A lattice-structured material is an interconnected network of repeating unit cells. These unit cells are combination of struts or beams connected at nodes, arranged in 2D or 3D space. These materials possess diverse mechanical properties such as customizable mechanical strength and stiffness as well as good energy and impact absorption capability. Moreover, the lightweight properties, optimizable geometry and versatile application potential have gained significant attraction from researchers in recent years [3].

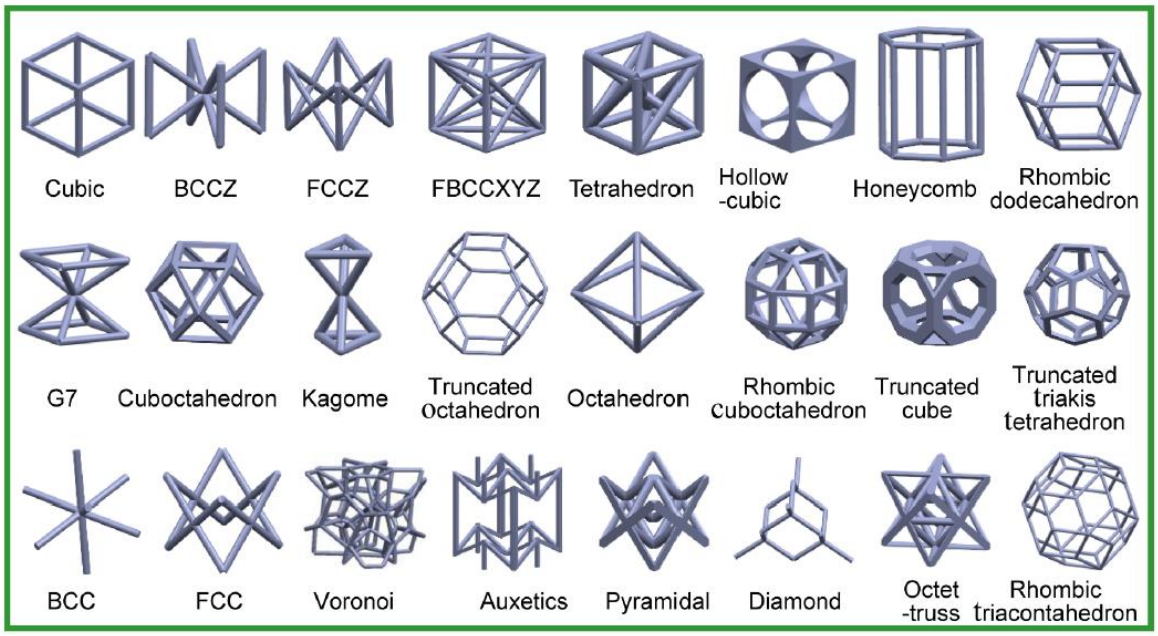


Figure 1.1: Common unit-cell designs for AM strut-based lattices [4]

Figure 1.1 illustrates some of the common unit cell designs that are available for additive manufactured lattice-structure parts. The unit cell design of lattice-structured materials can provide combinations of density, mechanical properties or functionalities that are not possible with solid materials alone [4]. A regular assessment of structural integrity of these AM lattice-structured parts in terms of age, usage and high-force tolerance level is necessary to ensure safety, product maintenance, quality control, durability, economic feasibility, etc.

The potential integration of image analysis methods to AM lattice-structured materials will enable them gain continuous sensing and material characterization capabilities. Deformation measurement is a crucial part of material characterization. Moreover, due to the compact size, complex shape and strong damping of AM lattice-structured materials, it is not desirable to use invasive techniques for deformation measurement [5], thus a non-invasive and low-cost method needs to be developed.

1.2 Deformation Analysis of Materials

Material characterization of AM lattice-structured materials is crucial for analysing and measuring different properties of these materials prior to their applications in many fields, such as medical and biomedical engineering, aviation, automation and robotics [6]. Different techniques and tools are available to gather physical, chemical, mechanical and thermal properties of the materials. This information is later used for material characterisation. One key aspect of material characterisation is deformation behaviour analysis, which is related to structural composition, durability, load bearing capability etc. of a material. Understanding deformation behaviour is also important for characterising high-value small-scale structures such as AM lattice-structured materials. These materials have a wide deformation pattern range, which is sometimes unpredictable due to their complex geometrical structure. A clear understanding of these materials' deformation behaviour is desirable due to their potential to be tailored for specific applications in multiple fields.

Deformation is the change in geometry of a material or structure due to external influences which can be caused by stress, temperature variation or pressure change. Deformation analysis of a material is the study of changes in size, shape or position of an object subjected to external forces or environmental conditions. It is the process of quantifying the change to ensure the safety and efficiency of structures and mechanical components [7]. For lattice structures, the

deformation behaviour can be classified into 3 stages: (a) linear elastic deformation, (b) plastic deformation and (c) compacting. The deformation behaviour can be identified based on the type of deformation mode within the plastic deformation regions [8]. Figure 1.2 shows the schematic stress-strain diagram of these deformation modes [9]. Deformation analysis is essential in the field of engineering for designing of material and ensuring structural safety and functionality.

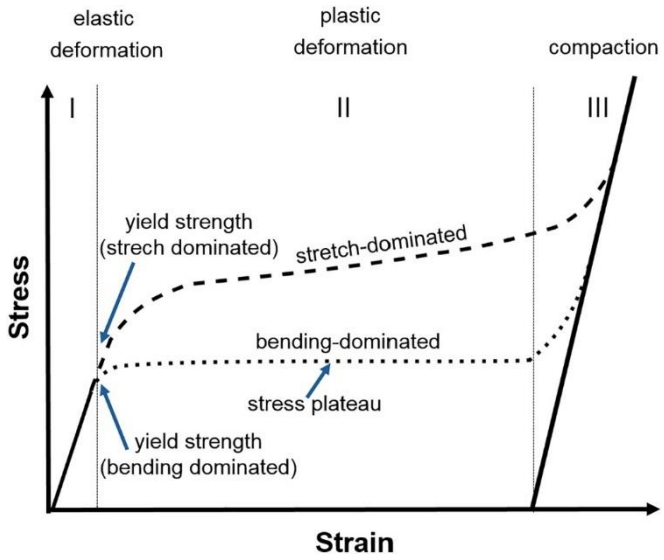


Figure 1.2: Schematic compression stress-strain curve of lattice structure [9]

The deformation is measured through a range of established contact and non-contact methods. The contact method's tools need to be installed on the surface of the structure which interfere with the structure's shape or integrity. Different contact based wired or wireless sensors (i.e. accelerometers, strain gauges, fibreoptic sensors, piezoelectric sensors, ultrasonic waves, displacement sensors etc.) can often present challenges in terms of installation and maintenance feasibility. These measurement tools are susceptible to environmental condition and full-field deformation is difficult to measure in small-scale structures like lattice-structured parts. Moreover, these sensors typically provide intermittent data limited to the specific points where they are installed or applied. These tools such as strain gauge [10] are mostly effective for point deformation measurement and on large structures, such as bridges [11].

On the other hand, non-contact measurement methods such as Digital Image Correlation (DIC), photogrammetry and Moiré interferometry can be reliable options for inspecting the actual

condition of the structure without damaging it. The non-contact optical method is a robust non-invasive technology for non-destructive evaluation of structure. Furthermore, the techniques in this method effectively ensure damage detection in large infrastructures or structures in a difficult-to-reach location (i.e., large bridge, high-rise building, structure underwater or space). These methods are also suitable for full-field deformation measurement of AM lattice-structured materials. Hence, a paradigm shift has occurred in deformation measurement approaches in the recent years with the advancement of non-contact-based sensors including optical sensors, drones, robots, as well as enhanced image processing techniques. These non-contact optical methods are often portable, cost-effective, easy to install, capable of automated assessment and provide long-distance measurement; therefore, they are more effective compared to conventional approaches [12], [13], [14].

Although, the field of material characterization covers the overall condition assessment, performance monitoring, and damage detection of the structure, a specific focus on the shape changes or displacement of AM lattice-structured materials is required. Therefore, this research focuses exclusively on deformation measurement techniques for these structures. Moreover, these complex geometry materials have unpredictable deformation, which cannot be measured with intrusive sensors or tools like strain gauges alone. Thus, visual assessment through optical sensors (non-contact, non-interferometric optical method) is an optimal choice for the deformation measurement of AM lattice-structured materials.

Among the known non-contact non-interferometric optical methods, DIC is a powerful technique for full-field measurement of deformation. DIC is versatile to be used in both 2D and 3D analysis. 2D DIC technique is favoured for this research in terms of assessing deformation in the planar surface as well as computational and economic feasibility. The 2D DIC is applied directly to determine the deformation field quantitatively and to characterize the deformation mechanism of various materials subjected to mechanical loading, thermal loading or other loading. The behaviour of diverse systems under 2D DIC has been studied, such as biological materials [15], [16], metal alloys [17], shape memory alloys [18], porous metals [19], polymers [20] and polymer foams [21],[22]. Significant advances have been made in image-based deformation measurement techniques such as DIC, but limited research has been found on AM lattice-structured parts [23]. Moreover, comprehensive performance evaluation and a

comparative analysis among different DIC software platforms and methodologies remain crucial for establishing standardized measurement protocols.

1.3 Aim and Objectives of the Research

The main aim of this study is to analyse the deformation of 3D-printed lattice-structured materials through imaging and image processing techniques.

The core objectives of this study are:

- To review and define the state-of-the-art in 3D-printed lattice-structured materials. Existing techniques for the characterisation of lattice structured materials and their deformation analysis through digital imaging and image processing techniques will be reviewed and gaps that require further research in the field identified.
- To record images of the compression tests on 3D-printed lattice-structured materials of different lattice types, designs, and sizes, and to create a dataset of it.
- To process the visual information by scaling of deformation through different 2D DIC analysis software.
- To develop a model using imaging technology for deformation measurement of 3D-printed lattice-structured materials.
- To compare the performance of different DIC software and the proposed model based on Imaging Technique.
- To validate the accuracy of the system with experimental data and through Finite Element Analysis (FEA).
- To investigate the effect of imaging setup parameters and image preprocessing variables, such as the camera configuration, patterns on materials, segmentation and other related factors, on the image analysis process and results.

This study compares image analysis technology-based low-cost deformation measurement systems for AM lattice-structured parts, where multiple common unit cell designs for lattices such as Cubic, BCC, BCCZ, FCC and FCCZ are used to fabricate these parts. The parts are then deformed using a mechanical tensile machine and reference deformation parameters including stress/strain are acquired from the machine. The entire deformation process is also recorded through a camera sensor from a reference point. Hereafter, the deformation of the

materials under loading is calculated through image analysis techniques, such as DIC and the proposed model based on Imaging Technique. The performance of the proposed methodology is evaluated based on the reference readings obtained from the tensile machine. There is also scope for improvement in combining DIC software with simulation tools such as Finite Element Model (FEM) software to obtain more accurate results [24].

1.4 Research Contribution

This study focuses on 2D DIC and novel Imaging Technique models for measuring the deformation of 3D-printed lattice-structure materials through image analysis. The image analysis results are compared and validated against the numerical analysis results.

Most of the research conducted on 3D-printed lattice structures has focused on the mechanical properties, the material and design optimization, manufacturing techniques or applications of the structures. The comparative studies on different image analysis techniques for deformation measurement of 3D-printed lattice-structured parts are found to be limited. Moreover, some of the properties of the lattice structure (i.e., full-field deformation) can only be measured visually rather than with a measuring tool. Therefore, this research aims to enhance the field of deformation analysis of 3D-printed lattice-structured parts by utilizing a range of image analysis techniques.

DIC is being used as a reliable source to validate the results from Finite Element Analysis of lattice structures [25]. Nonetheless, the DIC analysis results of different software can vary due to differences in algorithms, image processing techniques and user-defined parameters. Hence, it is important to compare the results from different software with each other and with the FEA results. This methodology will quantify the extent of deviation among different DIC approaches and ensure the reliability of the measurement.

Furthermore, this research intends to evaluate potential improvement in results by incorporating different approaches within established DIC software. In addition, an algorithm based on Imaging Technology is developed for analysing the deformation of lattice structures, as a novel approach to improve accuracy and reliability of measurements in the related fields.

Additionally, this research builds a comprehensive dataset of images of 3D-printed lattice-structured materials under loading conditions. Limited datasets exist on comprehensive images

of 3D printing lattice structure's compression testing. While previous studies have relied on the DIC challenge dataset [26] or synthetic data, this research creates an extensive experimental dataset of 16 distinct samples across five different lattice structure types. The experiments also include two types of 3D printing materials: Polylactic Acid (PLA) and Thermoplastic Polyurethane (TPU) with different configurations, providing a robust foundation for deformation analysis. These two materials exhibit differing load bearing properties and behaviour which is beneficial for the comparative analysis required in this research. This initiative is particularly valuable given that existing studies often suffer from insufficient sample sizes and limited material variations [27]. The creation of this substantial dataset not only supports the current research but also establishes a foundation for future investigations in the field of lattice structure deformation analysis. This attempt addresses a critical research gap for a highly sophisticated and specialized field of deformation analysis of 3D-printed lattice-structured parts.

Chapter 2: Literature Review

As mentioned in the previous section, additive manufactured lattice-structured materials have garnered significant attention due to their special geometry, lightweight properties, and load-bearing capacities. An efficient monitoring system is necessary to guarantee the long-term performance and safety of this material. Furthermore, these structures are susceptible to deformation and failure under loading conditions. Therefore, a reliable deformation measurement technique is needed for deformation analysis and early failure detection. Some of the existing deformation measurement techniques are initially explored in this chapter. The general idea behind deformation measurement techniques for materials, several contact and non-contact methods for measuring deformation under it, and the current research on the Digital Image Correlation (DIC) methodology are all included in this. The DIC technique implemented on additive manufactured lattice-structure materials is discussed as well.

2.1 Lattice-structured Materials

Lattice structures represent a significant advancement in engineering design by offering unique combinations of material properties and exceptional architecture. The integration of AM technology to this structure type enables the fabrication of complex geometric patterns that are impossible in traditional manufacturing. Combining with an extensive range of materials, such as polymers, metals, composites and functionally graded materials facilitates structures tailored to specific applications [28].

3D-printed lattice structures have broad applicability in engineering and manufacturing [29]. This lattice-structured material can be used in the unmanned aerial vehicles (UAV) as an internal support for wings [30]. In structural engineering, it can be incorporated within the individual struts of trusses to improve stress distribution, strength and manufacturability [31].

AM lattice-structured materials have prospects in the biomedical field as bone scaffold implants. Hulme et al. [32] investigated the mechanical properties of lattice structures for bone scaffold applications, focusing on their compressive strength characteristics. While their research demonstrated the structural viability of lattice designs for supporting surrounding tissue, the study was limited to strength analysis without exploring methodologies for measuring and characterizing deformation behaviour under loading conditions.

Additive Manufacturing has promising potential in creating biodegradable composite filaments for lattice structures. Qin et al. [33] fabricated a PLA-based biodegradable composite material that has good energy absorption capacity and high structural stability. The study fabricated lattice-structured parts with this new composite material and conducted a compression test to investigate the characterization of the material. One of the main challenges of lattice-structured parts is investigating the deformation in the inner layers of the structure. In this research, the deformation behaviour of the internal structure was identified through computed tomography (CT). While CT scans are effective for observing inner deformation, they are less suitable for small-scale research due to budget constraints, limited availability, and the specialized expertise required to operate the tool.

Modir et al. [34] explored the loading change of additively manufactured small polymer parts using piezoelectric elements. Their research integrated deep learning approaches, specifically Convolutional Neural Networks (CNN), to estimate compressive loading conditions. Their methodology successfully demonstrated the potential of combining structural health monitoring with artificial intelligence for structural integrity assessment of additively manufactured components. However, their scope was limited to load estimation without investigating the associated deformation behaviour of the components under applied forces.

Bahrami Babamiri et al. [35] has investigated the deformation mechanisms and post-yielding behaviour of AM lattice-structured materials using the volumetric hardening model (VHM). This model is suitable for describing the mechanical behaviour of materials with different responses under compression and tension, such as lattice structures. This research develops a modified VHM to explore damage initiation and evolution as well as the global stress-strain response using FEA. However, it is a complex technique with limited applicability only effective for specific materials. It also requires significant computation resources, whereas the DIC technique is more straightforward with wide applicability and verified accuracy.

Firsov et al. [36] conducted research to characterize the material properties of 3D-printed steel lattice structures. This study focused on the spatially temporal patterns of localization of deformation in this material. The deformation localization is observed using DIC. One of the major findings of this research is that 3D-printed lattice-structured samples lose the plasticity, and the Poisson's ratio increases 1.3-2 times compared to solid materials. Therefore, this

structure type demands dedicated research to comprehensively study the manufacturing-induced variations in material properties.

Most deformation analyses of lattice structure studies use FEA to calculate the full-field deformation in lattice structures numerically. However, the full-field deformation results from the experiment are also required to validate the numerical investigation. DIC is a robust technique to attain that experiment results for 3D-printed lattice structures. More research works incorporating DIC into different lattice-structured materials are discussed in section 2.4.

2.2 Deformation Measurement Techniques for Materials

One of the motivations of this research is that minimal work has been found on the deformation measurement of 3D-printed lattice-structured parts through image-based techniques. A review paper [12] discusses the recent advances in structural health monitoring (SHM) for deformation, including DIC, using optical devices, computer vision, and image processing. All the research works discussed here are conducted on bridges, walls, buildings or other structures. Additionally, the research discussed in this review address the vibration estimation, displacement estimation, damage detection and cracks on surface.

Deformation measurement of large structures, such as bridges, can be effectively conducted using 3D DIC. In a study by Ngeljaratan et al. [37], target-tracking DIC was employed in a large-scale laboratory setting to observe the response of a bridge structure. This method identified various modal properties, including natural frequency, damping ratio, and mode shapes.

This section first examines the existing methodologies for deformation analysis to initiate the discussion on DIC analysis of 3D-printed lattice structures. Then, the chapter delves into the literature on the DIC technique and its application to lattice structures.

2.2.1 Contact Methods

Deformation measurement techniques can be categorized into contact and non-contact methods. Contact methods involve direct physical interaction, with the structure while non-contact methods allow remote monitoring without physical contact.

Understanding a structure's strain distribution and deformation under loading is crucial for optimum structure design. Many contact methods are used to measure surface deformation. One of the oldest and most used devices for such is strain gauge, which generates precise results. However, the traditional strain gauges only measure points, necessitating a large number of sensors or measuring locations. These sensors are expensive, and the installation is time-consuming as well [38].

Other contact methods include accelerometers, displacement sensors, fibre optic sensors, piezoelectric sensors etc. Even though contact methods provide highly accurate and precise results on specific points of interest, these methods have several disadvantages in the material characterization of lattice structures. Contact sensors need to be physically attached to the structure, which can be challenging for the complex and intricate design of lattice structures. These sensors also provide localized measurements, have installation complexity and the installation may interfere with the structural behaviour. These limitations highlight the need for non-contact methods, such as DIC, which can provide comprehensive and non-intrusive monitoring of lattice structures.

2.2.2 Non-Contact Optical Methods

In experimental solid mechanics, one important task is to measure deformation of a structure under different loadings, which can be conducted using non-contact optical methods. The non-contact optical methods for measuring deformation can be interferometric or non-interferometric.

Interferometric techniques such as holography interferometry, speckle interferometry and moiré interferometry require a clear light source and vibration-isolated optical platform in the laboratory. Furthermore, these techniques operate by measuring the phase difference of dispersed light waves from the test object surface before and after deformation.

On the other hand, the non-interferometric techniques, including grid method and DIC, are generally lenient in conditions for experimental settings. These techniques identify deformation by measuring the variation of an object's grey scale intensity before and after deformation. Among these, DIC is one of the influential and flexible tools for surface deformation measurement based on digital image processing and numerical computing [39]. A few of the

prominent non-contact interferometric and non-interferometric methods are discussed in the following subsections.

2.2.3 Moiré Method

Moiré method is one of the non-contact, high-sensitivity optical techniques used for displacement measurement in materials. In this method, a reference or master grating is attached to undeformed reference and another grating is attached to the deformed specimen with slightly different pitches. While these two grids or gratings are superimposed, a moiré pattern of light and dark band appear which is sensitive to small deformations. There are different types of this method such as: geometric moiré [40], moiré interferometry, microscope moiré method, digital moiré method [41], sampling moiré method [42]. Ri et al. [38] suggests a sampling moiré method for accurate and fast measurement of small deformation. This method is found to be robust due to it being non-sensitive to lighting unlike other optical methods.

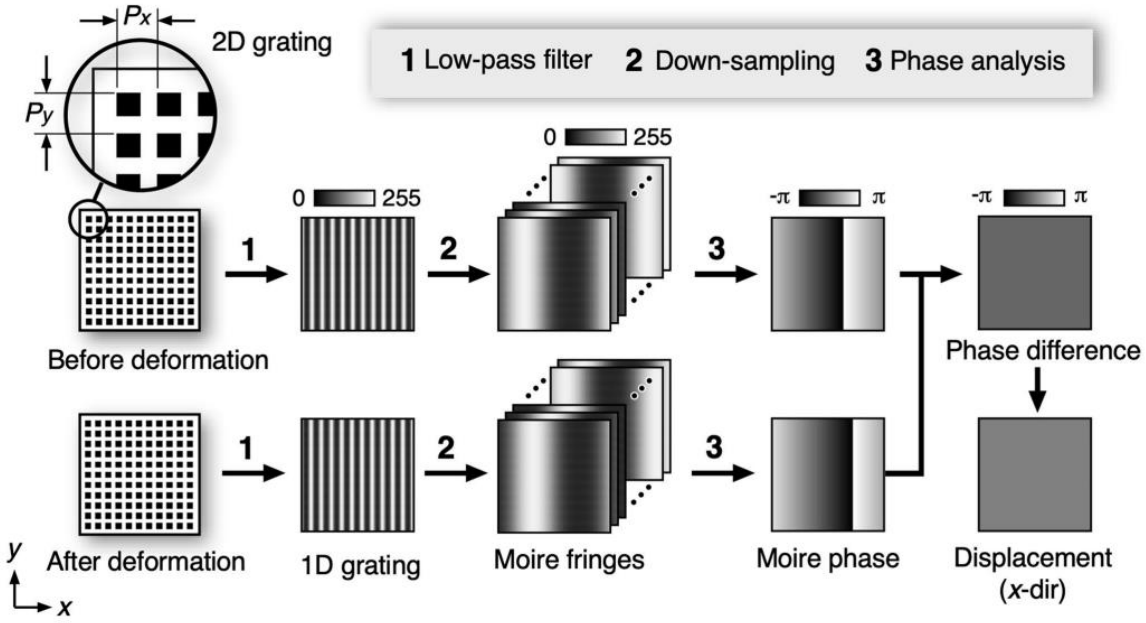


Figure 2.1: Principle of sampling moiré method for measuring in-plane displacement [43]

Figure 2.1 depicts the basic principles of the sampling moiré method where the displacement distribution in the x-direction utilizes a repeated pattern. The phase difference of the moiré fringe before and after deformation determines the in-plane displacement. This method uses phase information of the low frequency of a repeated pattern. This approach is suitable for field experiments [43]. However, this method requires precise measurement of the grating, which

calls for a complex setup process. It also requires a high-resolution camera to maintain spatial resolution and for micron-level study [38], [40].

2.2.4 Multi-point Pattern Matching

Dong et al. [44] proposed a non-contact, high-resolution technique which is alternative to conventional accelerometers and other contact-based methods for effectively monitoring structural displacement. This vision-based, dynamic displacement measurement method relies on a multi-point pattern matching algorithm to track targets in each image by matching predefined patterns. It calculates a scale ratio (r) from the actual distance (D_i) and pixel coordinates (x_0', y_0') and (x_i', y_j') use normalised correlation coefficients to determine target positions and structural displacements. Figure 2.2 depicts the flowchart used in this study. They also used Fast Fourier Transform (FFT) to find the natural frequencies of simply supported rectangular steel beams. This study compares these results with accelerometer results to verify, and it shows 6-15% error compared to the theoretical model of the beam. However, this study only uses three modal points to track the displacement instead of measuring deformation for all points on the surface plane. This method is rather suitable for large infrastructure than small-scale structures.

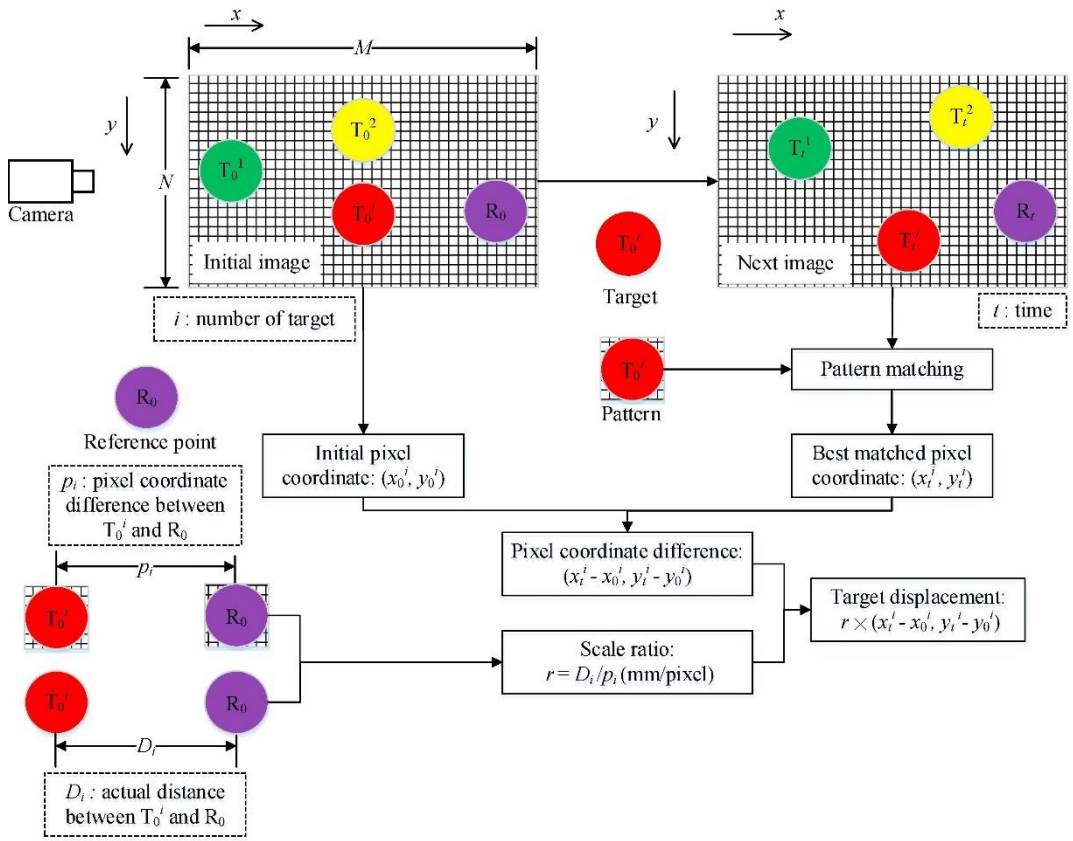


Figure 2.2: Flowchart of vision-based displacement measurement of multiple points for Multi-point Pattern Matching Technique [44].

2.2.5 Photogrammetry

Image matching is elementary process for automatic orientation in digital photogrammetry. One of the fundamental processes in photogrammetry is image registration which involves aligning two or more images of a scene from different views and dates [45]. This method is useful in combining images that are captured with different sensors or at different time.

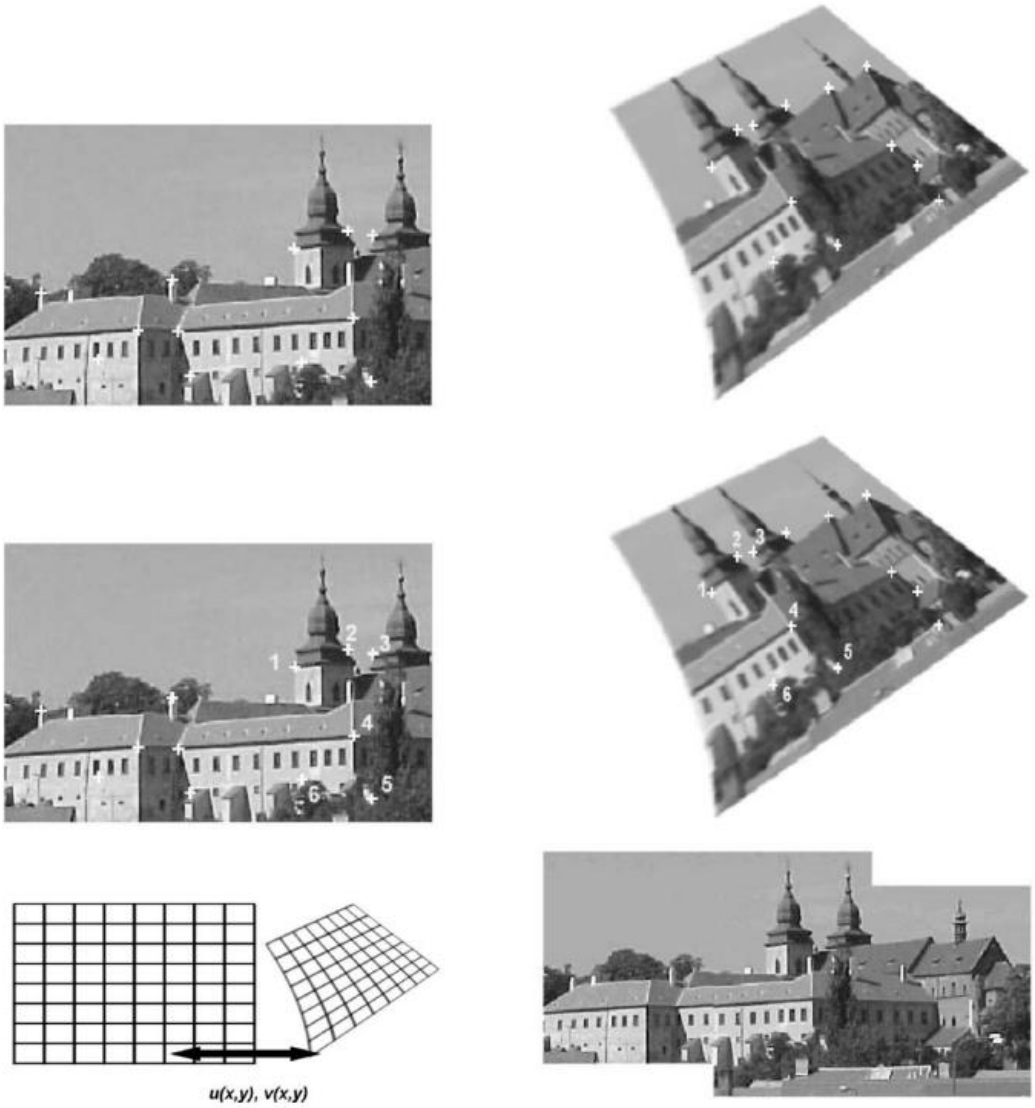


Figure 2.3: Four steps of image registration: top row—feature detection (corners were used as the features in this case). Middle row—feature matching by invariant descriptors (the corresponding pairs are marked by numbers). Bottom left—transform model estimation exploiting the established correspondence. Bottom right—image resampling and transformation using appropriate interpolation technique [46].

Image registration is divided into two categories: area-based methods and feature based methods. Additionally, most of the image registration methods follow these four steps of (i) feature detection, (ii) feature matching, (iii) transform model estimation and (iv) image resampling and transformation [46].

The unregistered image is compared with source image's points of interest. The points of interest are obtained by different area-based approaches such as- normalised cross correlation (NCC) and discrete cosine transform (DCT) used in [47] for satellite images. Another high accuracy area-based image registration technique is Fourier-based image correlation based on similarity model through image information and operation in frequency domain [48].

In feature based matching approach, methods like Scale-Invariant Feature Transform (SIFT) [49], Speeded Up Robust Features (SURF) [50] are used to identify and match points of interest across images. These methods are useful in real-time applications; however, one of the drawbacks is that the similarity measure maxima are flat in correlation-based methods. Therefore, it is difficult to measure displacement in object with high self-similarity like 3D-printed lattice-structured parts [46]. The similar problem occurs with feature-based matching of SIFT in lattice structures which is observed in this research during implementation of the proposed deformation measurement algorithm.

DIC stands out as one of the most widely used techniques in the field of experimental mechanics and computer vision alongside image registration or matching methods. A comparative study on image registration and DIC has been conducted by Wang et al. 2015 [51]. This study discusses the similarities and dissimilarities of these two techniques. Both techniques have image matching feature detecting same physical points in two or more images and camera calibration is an important step for both techniques. On the other hand, the differences between these two techniques mainly lie in pattern and area-based matching. DIC uses artificial random speckle patterns and specific Region of Interest (ROI) based matching to complete the analysis. Alternatively, image registration technique uses the natural texture of the object with both area and feature based matching to complete the analysis. Even though DIC technique's processing is slower, it provides results higher in accuracy than image registration technique. This study also emphasizes on incorporating image registration technique into DIC technique to improve the efficiency and reduce computational time.

Deformation analysis of small-scale structures is difficult due to target size and visibility compared to normal sized structures or large structures. These require extremely high-resolution imaging and precise tracking method. Moreover, these small-scale structures are more sensitive to lighting conditions and vibrations. Small-scale structures with gaps between

the beams such as lattice-structured materials require more precision while determining deformation through image analysis. Therefore, a consistent, high-precision, non-contact deformation analysis system is required for 3D-printed lattice-structured materials used in this research. DIC has garnered acceptance for being able to detect displacement at a microscopic scale and it has been widely used with structures of different materials and sizes.

2.3 Digital Image Correlation (DIC)

In the past two decades, DIC systems have established dominance in the experimental mechanics community, surpassing interferometric optical techniques such as electronic speckle pattern interferometry (ESPI) and Moiré interferometry (MI). This has also facilitated their widespread application in diverse fields, including material science, biomechanics, civil engineering, geotechnical engineering, and aerospace engineering [24].

The availability of numerous and diversified image processing algorithms has enabled researchers to choose according to the requirement of an application [52]. The DIC technique is a rapid, steadfast, economically feasible and non-contact NDT method [53]. DIC is flexible in processing 2D and 3D datasets for acquiring displacements and deformation measurements in a structure [54]. This optical technique is also versatile with different materials, sizes, loading conditions and experimental location or condition. The displacement and strain field obtained from DIC are utilized for characterization, identification and cross-validation. There are three broad categories of DIC- 2D DIC, 3D or Stereo DIC and Digital Volume Correlation (DVC) [24]. The three main categories of DIC techniques with their experimental setup, imaging system and applicability are visually elaborated in Figure 2.4. In terms of computational complexity and economic feasibility, 2D DIC technique is more favourable than the others.

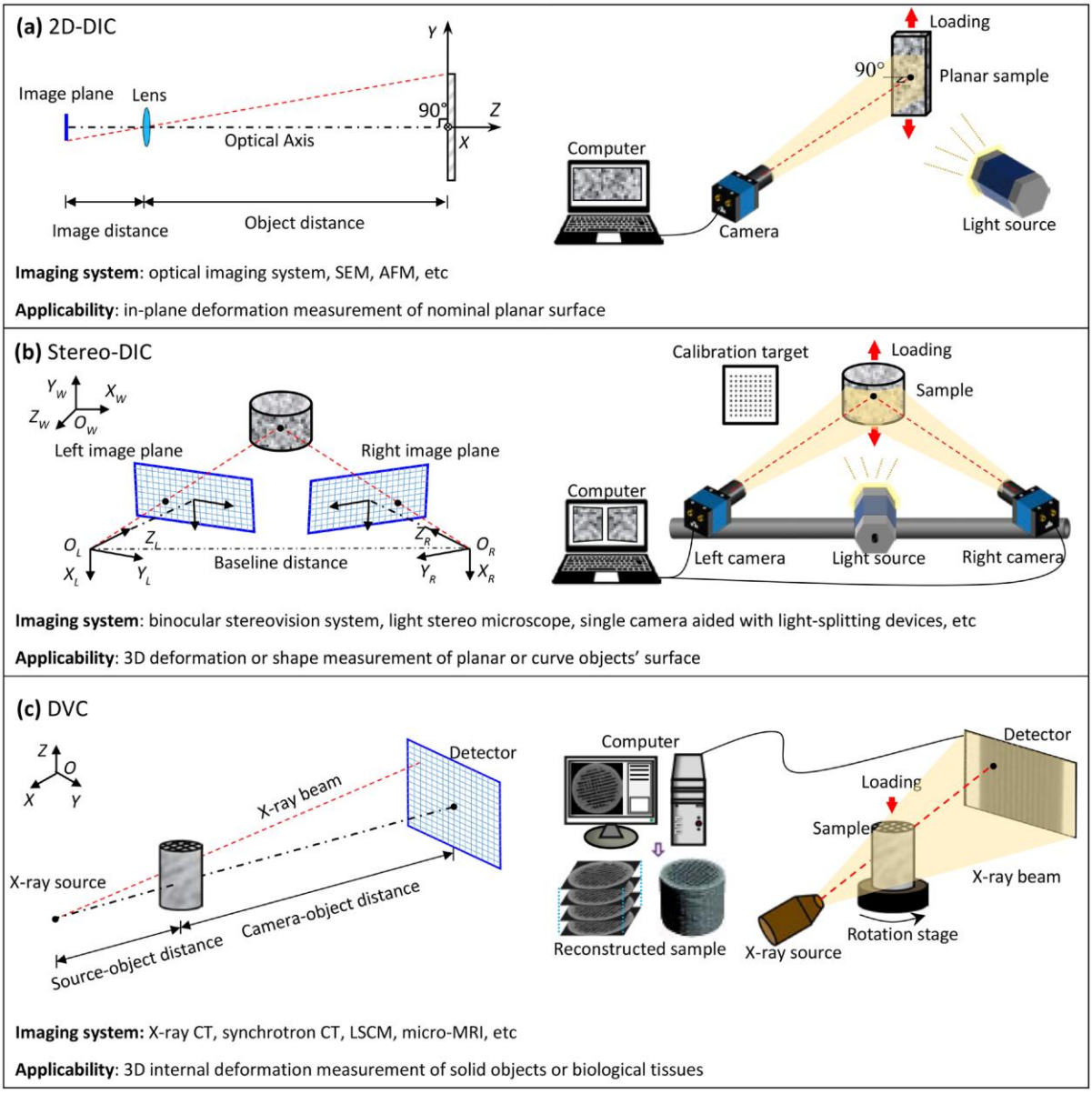


Figure 2.4: The imaging models, systems and applicability of three typical DIC techniques [24]

2.3.1 2D DIC Technique

Some of the advantages that make 2D DIC special and attractive are its requirement of simple experimental setup and specimen preparation. Only a single fixed camera is needed to acquire the digital images of the test specimen before and after deformation. The test specimen surface requires random speckle patterns which can be obtained by spraying paint on the surface. There are also low requirements in case of environmental conditions while taking measurements in

2D DIC. For instance, a white light or natural light source can be used for image acquisition instead of a laser source in the experimental setup. Thus, the experimental requirement suits both laboratory and real-life conditions [39]. 2D DIC also has a wide range of measurement sensitivity and resolution. 2D DIC can be combined with optical microscopy [55], laser scanning confocal microscope (LSCM) [56], scanning electron microscopy (SEM) [57], atomic force microscopy (AFM) [58] and scanning tunnelling microscope (STM) [59] to perform microscale to nanoscale deformation measurement. Likewise, the rapid deformation measurement can be attained by analysing the dynamic sequence of digital images recorded with high-speed digital image recording equipment using the 2D DIC method [60]].

Even though being easy to implement, one of the major limitations of 2D DIC is that it can be used only to determine in-plane deformation of nominal planar surface [24]. However, out-of-plane motion in test planar samples due to different conditions exists in practical field, such as: out-of-plane motion caused by loading and sample deformation, out-of-plane motion in a sensor plane caused by temperature variation of the camera, the unavoidable lens distortion, as well as ambient light variations and ambient vibrations [61], [62] . Moreover, adverse effects such as lens distortion [63], non-perpendicular camera alignment [64], self-heating effect of digital cameras [65], and ambient light variations [66] are also needed to be considered during 2D-DIC measurement [24].

Currently several commercial and open-source software are available for implementing DIC [67]. GOM Correlate or Zeiss Inspect [68], MatchID [69], VIC-2D (Correlated Solutions) [70] and ARAMIS (GOM) [71] are some of the commercially available software for implementing DIC. There are also several open-source or open access codes available which require a licensed platform to execute [72] such as Matlab-based Ncorr [22], Python based py2DIC [67], iCorrVision-2D [72] etc. Among these, MATLAB-based NCorr software is versatile to suit a wide range of applications, cost-effective and easy to implement [22].

Figure 2.5 illustrates the step-by-step workflow of DIC analysis software Ncorr which is used in this research. This software developed by Blaber et al. [22] have been verified and compared with other 2D DIC Software and found to obtain competitive results [67], [73], [74], [75].

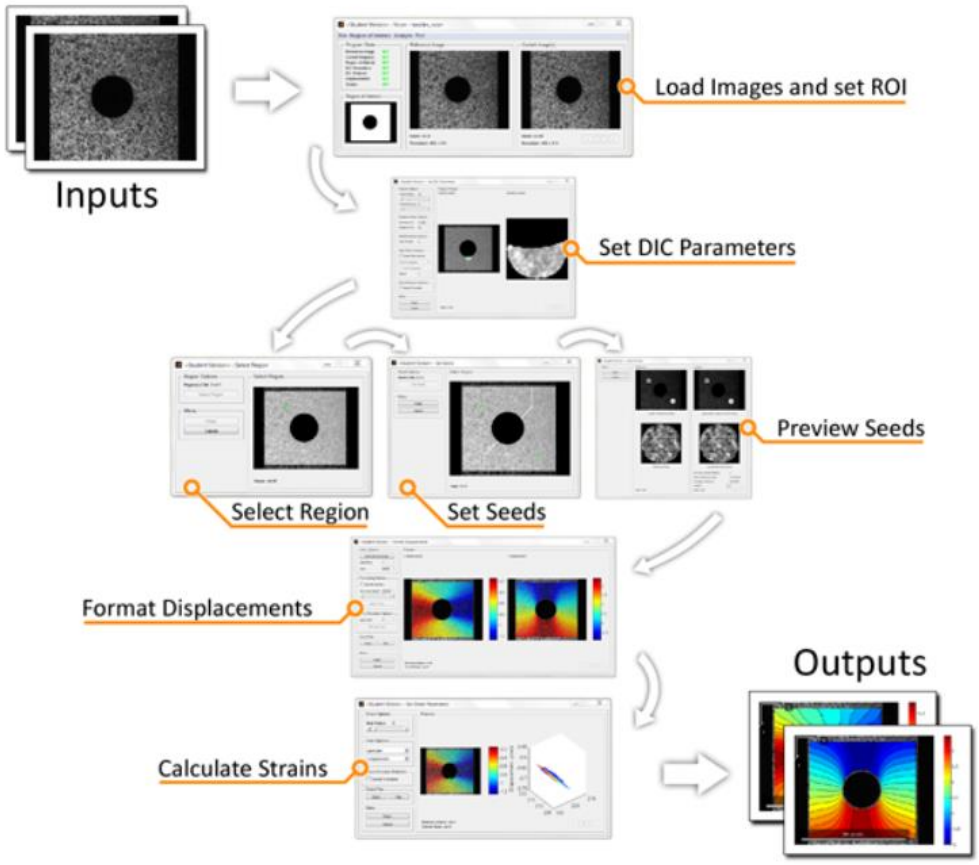


Figure 2.5: Step-by-step workflow of 2D DIC technique using Ncorr software [76]

Among the commercial software, Zeiss Inspect Correlate (formerly known as GOM correlate) is a well-known software that has been used as reliable tool for strain measurement [77]. Among the previous research works, DIC analysis results from Zeiss/GOM correlate have been found in visually good agreement with other software results for simple materials [78], [79].

DIC technique has been used in large structures as part of Structural Health Monitoring (SHM) of those structures. Displacement measurement using DIC has been proved to require less time, effort and equipment in terms of monitoring large structures like bridges. Winkler et al. [80] conducted research to determine the in-situ stress condition of light railway bridge using DIC as cost effective and non-interferometric option.

The study by Kalaitzakis et al. [81] introduces the use of a DIC stereo vision system mounted on an Unmanned Aerial Vehicle (UAV) for the structural assessment of prestressed railroad ties under continuous loading conditions. This innovative approach is validated using moving

cameras, facilitating more rapid and precise inspections in remote locations. Future improvements involve the integration of the DIC system with UAV avionics and the development of a specialized drone. According to this study, the major drawbacks of DIC analysis with UAV are lacking accuracy in results or requiring human intervention to operate.

2D DIC has been incorporated as well with unmanned aerial vehicle (UAV) to measure the strains and displacements at inaccessible locations of structures by Kumarapu et al. [75]. This research implemented DIC technique on a Reinforced Cement Concrete (RCC) bridge girder in laboratory and a rail over bridge in real life condition. The open source 2D DIC software Ncorr successfully measures the strains and deformation of the samples.

Mousa et al. [82] have reviewed research on vision-based approach by using the DIC technique on different bridge infrastructures. For non-contact, non-destructive, long-distance and high-precision qualities, this study favours a vision-based approach like DIC. It can also monitor multiple targets and is free from electromagnetic interference This study also concludes that DIC technique is adaptable enough to pair with various modern techniques and tools. When conventional monitoring methods are ineffective, the DIC methodology offers an alternative. Results using the DIC technique have been found to be competitive with results using conventional metrological tools like Linear Variable Differential Transformer (LVDT) [83], strain gauges and numerical simulation. According to this study, DIC could also detect damage such as fractures and spalling besides structural elements including vibration, deflection, and rotation. Nevertheless, there have been some variations in results attributed to illumination and flickering, camera instability and speckle pattern quality. In line with the results of this research, the study also states that image quality and speckle pattern contrast are crucial for DIC analysis.

To attain full-field deformation measurement, an optical strain gauge is incorporated with Automatic Digital Image Correlation (ADIC) technique for concrete cylinders by Huang et al. [84]. The optical strain gauges are recommended due to being more flexible than fixed-size compress meters.



Figure 2.6: Experiment setup of [84] with optical strain gauge incorporated with Automatic Digital Image Correlation (ADIC) technique

Research by Harilal et al [73] compares the results of DIC analysis with Ncorr and Vic-2D for a ring sample under compression and a beam sample under four-point bending. The results are found to be a close match with each other, thereby validating the performance of the open-source software. Both of the research mentioned here are conducted to validate a self-developed open-source DIC software which has been tested on samples of simple geometric shapes. In this regard, there is a need to evaluate the performance of the existing DIC software objectively for more complex structure such as 3D-printed lattice structures.

Some other researches have been conducted on comparing multiple open-source and commercial DIC software. But the experimental images used are from tensile tests on plate hole sample and Glass Fiber Reinforced Polymer sample. Ravanelli et al.[67] developed a free and open-source DIC software named Py2DIC and compared the outcome from DIC analysis of the same samples with other software. DIC analysis results from commercial software Vic-2D and two open-source software Ncorr and DICe have been compared against Py2DIC, and they have been found to be in a good agreement among themselves.

Another comparative study on three specialized DIC software i.e. Digital Image Correlation Engine (DICe), Ncorr and GOM Correlate software (Zeiss) on elastomer with different hole shapes has been conducted by Jorge et al. [85]. The stress concentrator values from different hole shapes for specimen under tensile load are compared among the DIC software results, theoretical results and FEA results. The outcome confirms good agreement of results within

the theoretical and experimental (DIC) data. The research also concludes GOM correlate (Zeiss) having the least error values with respect to the analytical result. Research is needed on more intricate samples, such as lattice structures, subjected to various loading conditions, including compressive loads.

Pan et al. [83] developed an advanced video deflectometer for non-contact, real-time measurement of bridge deflection using DIC. This study uses Gauss-Newton algorithm for sub-pixel accuracy in motion tracking and incorporated a calibration method to convert pixels to physical measurement in millimetres. This study also suggests that DIC technique is quantifiable and precise compared to conventional measuring techniques. However, there are systematic error attributed to image noise and intensity interpolation, which can be compensated by using higher order interpolation algorithms and pre-filtering of images.

Even though 3D DIC is used for large infrastructure in literature, 2D DIC is found to be more suitable for in-plane full-field deformation measurement of AM lattice-structured materials. Since a single camera can track the deformation of these types of structures, 2D DIC is cost-effective and requires less computational time. Therefore, 2D DIC is chosen for this research due to cost and time effectiveness.

2.4 DIC for Lattice Structures

As highlighted in the previous section, DIC is a powerful tool to numerically calculate the deformation field and to analyse the deformation mechanism of different materials under loading. Studies have applied 2D DIC to wide range of materials including biological materials, metal alloys, shape memory alloys, polymers, polymer foams etc.

Additive Manufactured (AM) or 3D-printed lattice structures are being widely used due to the better material qualities and high strength-to-weight ratios. The mechanical properties of this material can be customized as well. To guarantee these materials' performance and structural integrity under a range of loading scenarios, deformation analysis is crucial. Deformation analysis of 3D-printed lattice structures through image analysis techniques like DIC are especially preferred for their compact size, intricate forms, and unique deformation pattern. Studies have been conducted on different 3D-printed lattice-structured parts to assess the deformation behaviour and mechanical performance accurately using 2D DIC [86], [87], [88],

[89]. One of the main goals of these analysis is to ensure reliability and safety in practical applications. These studies found 2D DIC analysis technique to be credible for the deformation and strain analysis of AM lattice-structured parts.

A study on closed-cell aluminium foam by Wang et al. [86] used DIC technique to clarify the distinct deformation behaviours under varying impact speeds. The strain results from DIC were able to show the transition from uniform deformation to localised failure as impact speed increased. However, this study faced this limitation of DIC not being able to analyse the zone of complete failure effectively. Therefore, this study focused more on the areas that have been interpreted by DIC.

Speckle pattern on the surface of the sample is one of the most essential elements of DIC analysis. There has been research on multi-material 3D printing to create speckle patterns for DIC analysis in the field of aerodynamic measurement by Pankonien et al. [87]. This research used multi-material printing to fabricate high-contrast, high-resolution speckle patterns directly on the samples to improve the accuracy and efficiency in aerodynamic testing. This technique reduces the preparation time and increases the strain measurement precision in complex geometries. However, the opacity of the material affects the accuracy of the strain measurement. Additionally, the patterns cannot be altered after the fabrication, therefore the parts need to be reprinted if the pattern needs to be changed. Furthermore, the accuracy relies on high-resolution printing which is expensive for small budget research and application.

Yu et al. [88] employed DIC as a measurement tool to analyse full-field displacement, strain distribution, and crack propagation during compression tests on Aluminium alloy micro-lattices. This research has addressed the printability, compressive behaviour and failure modes of AlSi10Mg micro-lattices, alongside their structure-property relationship. This research treats DIC as a reliable tool for experimental data and does not criticize the results of DIC analysis on lattices.

The work of Sereshk et al. [89] is focused on the deformation analysis of lattices, utilizing DIC. This study focuses on establishing the necessary test protocols for compression testing of lattice structures in terms of sample geometry, test procedures, data collection and analysis. They state that there should be at least 5-unit cell repetitions in lattice structures to accurately represent the collapse mechanism. The load condition applied here was quasi-static whereas face plates

have been applied to ensure load application consistency. This study established DIC as an appropriate and reliable tool for lattice structures operational displacement analysis with predetermined subset size and distance between them.

DIC is applied using various software across different materials. However, there is a lack of studies comparing different deformation measurement techniques for lattice-structured parts. Consequently, this research aims to compare various deformation measurement techniques for 3D-printed lattice-structured components

2.4.1 DIC Analysis with Segmentation on Lattice Structures

One of the primary challenges in analysing the deformation of strut-based lattice-structured materials is accurately identifying deformation that occurs solely on the struts during image analysis. DIC analysis yields reliable results for conventional materials. However, in porous materials such as lattice structures, DIC sometimes erroneously detects deformation within the pores, which are not part of the structural framework. This can introduce errors in the results. Therefore, segmenting the struts of the materials in the images enhances the identification of the region of interest, leading to more accurate results.

One study by Vanderesse et al. [90] has addressed this issue by performing the segmentation process prior to DIC analysis. They utilized Fiji [91] for image segmentation and conducted the DIC analysis using OpenDIC [92]. The graphical abstract of that paper is shown in Figure 2.7, where the image of the front surface of the material is segmented before analysis. However, they follow complicated steps in the pre-processing stage before DIC analysis. This research proposes to establish a simpler segmentation process in the pre-processing stage of DIC analysis.

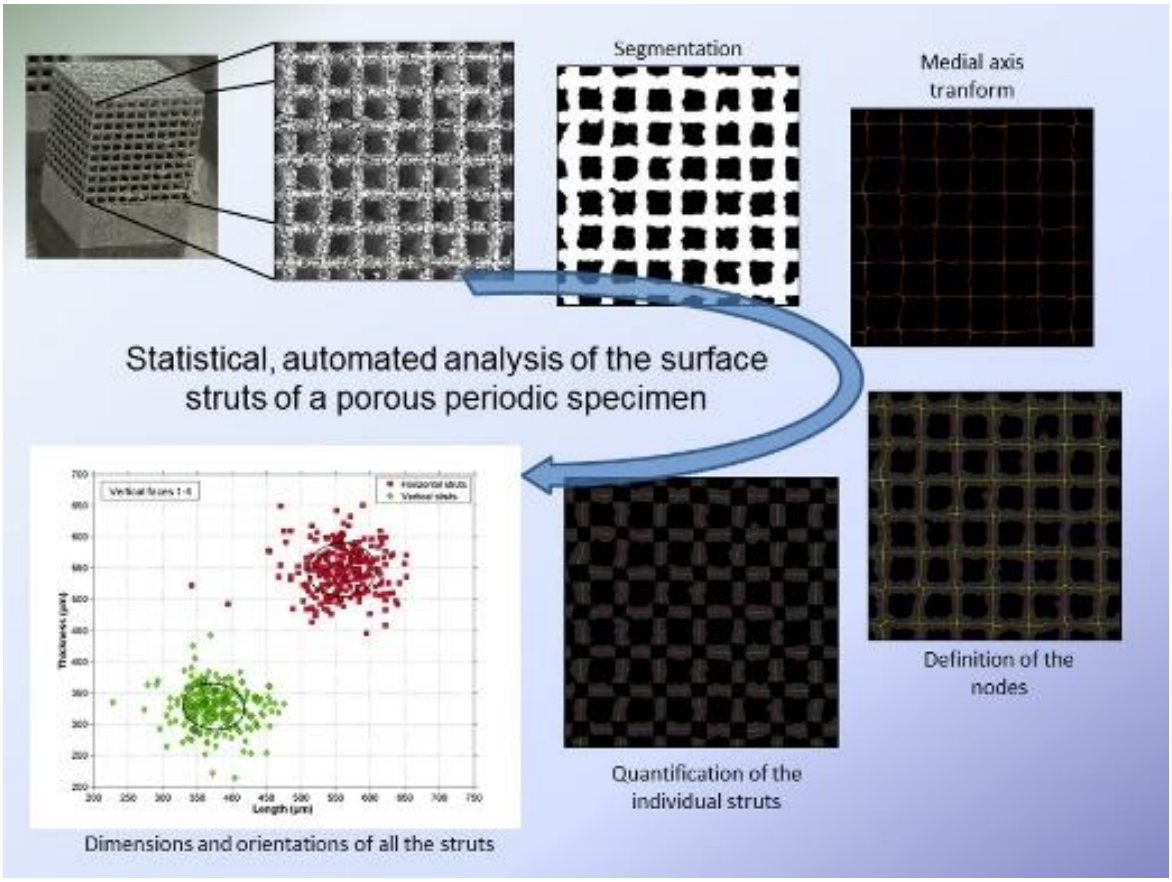


Figure 2.7: Graphical abstract of image analysis characterization of AM lattice-structured material [90]

Another study by Vanderesse et al. [93] implemented DIC on different porous lattice materials such as Cubic, Body Cubic Centred Reinforced (BCCZ) and diamond structures for potential use in orthopaedic applications. The structures were compressed until failure and the strain maps generated through DIC analysis were analysed. This study focused on the deformation behaviour of the lattice structures rather than the performance of the DIC analysis technique or software. To date, no other research has been found that performs segmentation of lattices for DIC analysis using an imaging-technique based algorithm and Ncorr software.

2.5 Digital Image Correlation and Finite Element Analysis

Several studies on the deformation analysis of lattice structures utilize Finite Element Analysis (FEA) to numerically calculate the full-field deformation. However experimental full-field deformation results are required as well to validate the numerical investigation. Literature indicates that DIC is a robust technique to attain experiment results for 3D-printed lattice

structures [94], [95]. FEA is incorporated in this research to analyse deformation through both numerical and experimental techniques, allowing for a comprehensive comparison of the results.

Boniotti et al. [94] conducted research on Aluminium alloy AlSi10Mg micro-lattices subjected to compressive load. Micro-lattices are network of interconnected complex micro struts made of metals or polymers. This research measured significant strain concentrations on the surface of Body Centred Cubic (BCC) lattice samples through DIC and later compared the results with the FEA Model results. The results were found to be qualitatively similar, rather lower than the strain concentrations measured with DIC. This study concludes that the FE model based on ideal geometry does not portray the actual behaviour of the printed lattice structure therefore further research is required in this field.

Xiao et al. [96] used DIC to analyse the strain distribution of 3D-printed Titanium alloy Ti-6Al-4V lattice structures under static and dynamic loading. The dynamic response of the lattice structures was simulated with FEA. The study compared DIC and FEA results to validate the accuracy and reliability of the numerical solutions. Both results demonstrate the designed gradient mode and loading direction having no effect on mechanical response of the material within 1000/s strain rate. The sample's deformed shape from FEA was found to be consistent with the result form DIC with error margin of 8% for collapse strength. The FEA was deemed reliable in this study despite inappropriate treatment of strut fractures after failure. The damaged struts were deleted after reaching failure strain in FEA, even though they provide support in real life experiment.

Similar research has been conducted on compressive or tensile behaviour of different 3D-printed lattice-structured materials such as Ti-6Al-4V lattice structures [95], 316L stainless steel [97], cold-formed High Strength Steels (HSS) [98], aluminium 7079 [99]. Both DIC and FEA have been proven to be efficient methodologies for simulation, analysis and validation of experimental results. The paper by Gothivarekar et al. [98] recommends adopting a ground-truth of full field comparison to improve the validation and scrutinize the predictive accuracy of an FE model. Another research by Peshave et al. investigated the performance of uncertainty quantification in DIC during validation with Finite Element Models [100]. Nevertheless,

limited research has been found on preformation evaluation of different DIC analysis software in comparison to FEA model.

2.6 Conclusion

The primary methodology of this research is developed based on the findings of this literature review, which will be discussed elaborately in the next chapter. It is observed from the extensive literature review that non-contact optical methods are good options for the deformation measurement of 3D-printed lattice-structured parts. From the previous studies, it is apparent that DIC is a strong technique for full-field deformation measurement in experimental mechanics. The results of DIC are also a reliable source of experimental data to validate the numerical analysis results obtained through the Finite Element Method.

The literature review reveals a research gap in the performance evaluation of different DIC software applied to 3D-printed lattice-structured materials. There is a scarcity of articles criticizing the DIC analysis technique for deformation analysis in 3D-printed lattice-structured materials, and an alternative method is seldom suggested.

Additionally, research on proposed models based on Imaging Technique for lattice-structured materials is notably limited. Most of the reviewed studies focus on the material's deformation behaviour or the validation of numerical analysis with experimental data. Hence, developing a deformation analysis model that is competitive with existing DIC analysis models could significantly improve the current methodologies. This advancement will also benefit the customization of deformation analysis processes for different materials.

There is a notable deficiency in creating a straightforward algorithm for the segmentation of lattice structures utilizing imaging technology. The existing works with lattices use a segmentation model, which is not imaging-techology-based and is complex too. This study intends to mitigate that gap by developing a segmentation technique specifically for lattice structures. Moreover, most of the research focus on the deformation of the elastic state of materials under loading, whereas this study aims to detect deformation at the failure stage. The deformation analysis in this stage is particularly challenging for porous materials due to material collapse and merging gaps. This approach also demonstrates the efficiency of the model under prolonged compression conditions.

Existing studies on DIC analysis of lattice-structured materials often overlook the details of the speckling process on lattice structures and do not conduct a comparative analysis of different speckling methods on the material. Similarly, various cameras for deformation analysis in lattice-structured materials are not evaluated. This research proposes simple and cost-effective speckle pattern options and cameras to address these gaps.

The studies covered here collectively demonstrate that combining FEA with DIC is effective for analysing and validating the deformation of lattice structures. While FEA provides numerical insights, DIC offers experimental validation. This integrated approach ensures more accurate and reliable results in studying material behaviour under various conditions.

Different commercial and open-source software are available for DIC analysis. Performances of those software in previous research are discussed in this chapter. An open-source DIC software: Ncorr and a commercial DIC software: Zeiss Inspect Correlate (previously known as GOM correlate) are chosen for this research based on their performance and availability. The literature also suggests incorporating computer vision technology into experimental mechanics, such as combining the image registration and DIC technique. Therefore, this study also implements an algorithm for deformation measurement through image analysis. The algorithm developed for this research is based on image registration technique and computer vision-based imaging technology. All the results from the proposed deformation measurement model, DIC analysis and FEA are compared for validation.

Chapter 3: Technical Approach

This chapter presents a comprehensive discussion of the research methodology, including theoretical concepts of Digital Image Correlation (DIC) and its validation through pre-existing datasets. The discussion progresses through the design and fabrication of the sample and details of the experiment. The experimental configuration includes image acquisition and image pre-processing techniques. The chapter concludes with the approach to Finite Element Analysis (FEA), providing a complete framework for this methodology.

3.1 Methodology

The methodology to implement deformation measurement techniques on 3D-printed Lattice-structured materials is illustrated in this chapter. The proposed methodology is divided into several steps: (i) calibration and fabrication of material, (ii) image acquisition through the mechanical test, (iii) pre-processing of images, (iv) region of interest identification, (v) deformation calculation and (vi) result validation. To calculate the deformation in step v, this research follows several approaches including (1) DIC Analysis using an open-source software NCorr, (2) DIC analysis in NCorr through segmentation, (3) DIC analysis in commercial software Zeiss Inspect Correlate, and (4) developing a novel Imaging Technique model for deformation analysis. Furthermore, for validation step (step vi) the Finite Element simulations (approach 5) have been setup for compression loadings on lattice-structures and the deformation results are compared with results from image analysis techniques. Figure 3.1 illustrates the overview of the proposed methodology that has been implemented in this research. Initially the DIC technique is applied to pre-existing dataset for calibration and simultaneously 3D-printed lattice-structured models are prepared for the mechanical test. The models are prepared by putting random speckle patterns on the surface of the parts facing the camera. The speckle patterns are required for analysis in DIC software Ncorr and Zeiss Inspect Correlate. Then, the mechanical test is conducted, and videos are acquired through a digital camera during the testing. Later in the pre-processing stage, the images from the video are extracted and converted to greyscale. The region of interest (ROI) is identified, and the images are cropped according to the ROI. Finally, the analysis is conducted through DIC technique, Imaging technique and Finite Element Method. The deformation of the 3D-printed lattice-

structured parts after the loading is calculated and compared with the tensile machine data for validation.

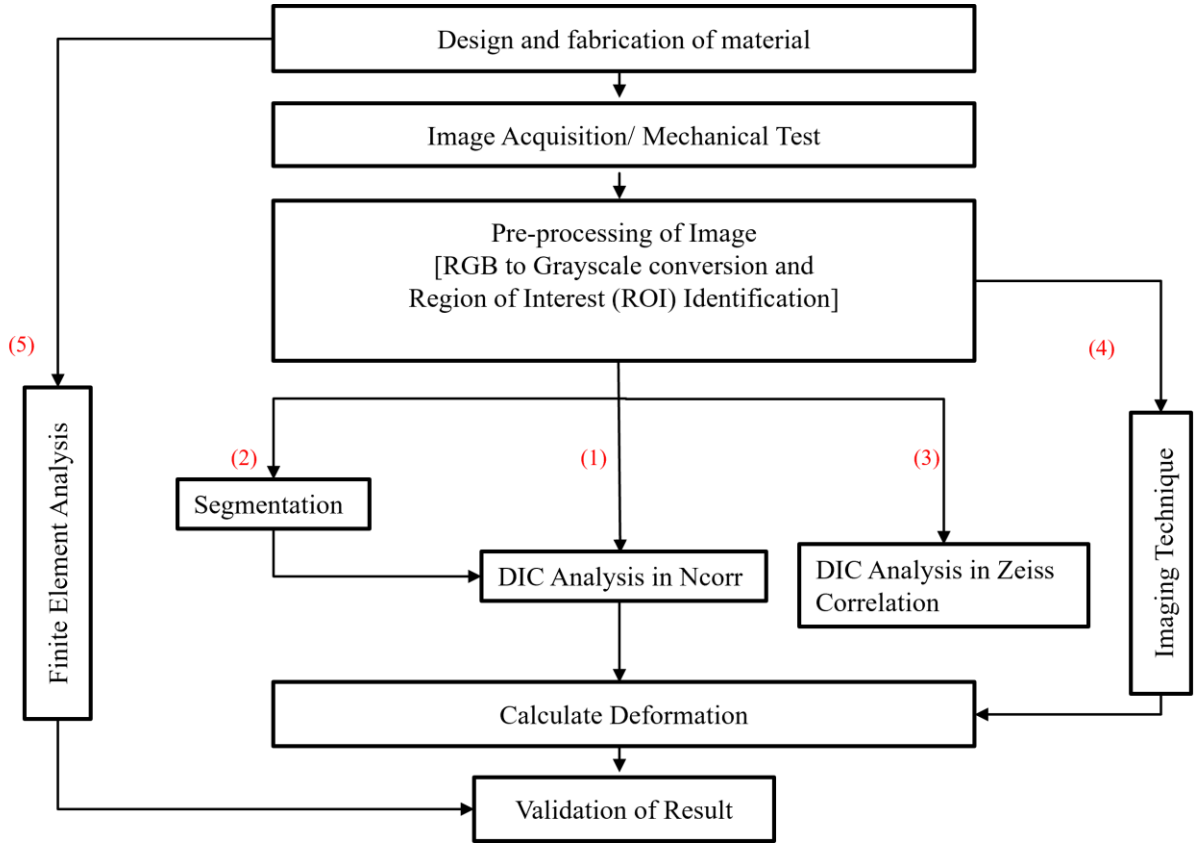


Figure 3.1: Proposed methodology for deformation measurement of 3D-printed lattice-structured materials through image analysis

3.2 DIC Concept

2D DIC technique has been used in this research as one of the major technical approaches to determine deformation in AM lattice-structured materials. The 2D DIC technique is favourable in the case of measuring microscale and nanoscale deformation by incorporating high-resolution image acquisition device [39]. In DIC, the images of a specimen in an undeformed state are taken and it is correlated with the images after deformation. The image before the deformation is named the reference image and the images after the deformation are all named deformed images. In this research, the images of the whole deformation process of the specimen under loading are captured in video and later extracted into images. The first extracted frame of the video that has been captured before the loading starts is considered the

reference image. The images are then divided into small facets or subsets and those subsets are tracked in each image to detect motion and deformation. The analysis and measurement are completed by comparing the subset location (pixel location) between the reference image and the deformed image [26]. Instead of individual pixels, square subsets are chosen due to the uniqueness of each subset for greater range in grey levels. The wider grey level variation in subsets help to distinguish one from the other in the deformed image [39].

The fundamental of the 2D DIC can be described in three steps as shown below:

Table 3.1: The fundamentals of DIC

Fundamentals of digital image correlation	Specimen and experimental preparation
	Recording image of the surface before and after the loading
	Processing image for displacement and strian field calculation

The basic working mechanism of DIC can be seen in Figure 3.2 where the first image depicts a reference image with a reference subset inside it. In the second image, the deformed image can be observed with a deformed subset inside. The length of the side of the subset used for analysis is 2M+1. Here, M represents the number of pixels from the centre of the subset to its edge. 2M+1 ensures the subset has an odd number of pixels along each side which is required for symmetry and accurate centre positioning.

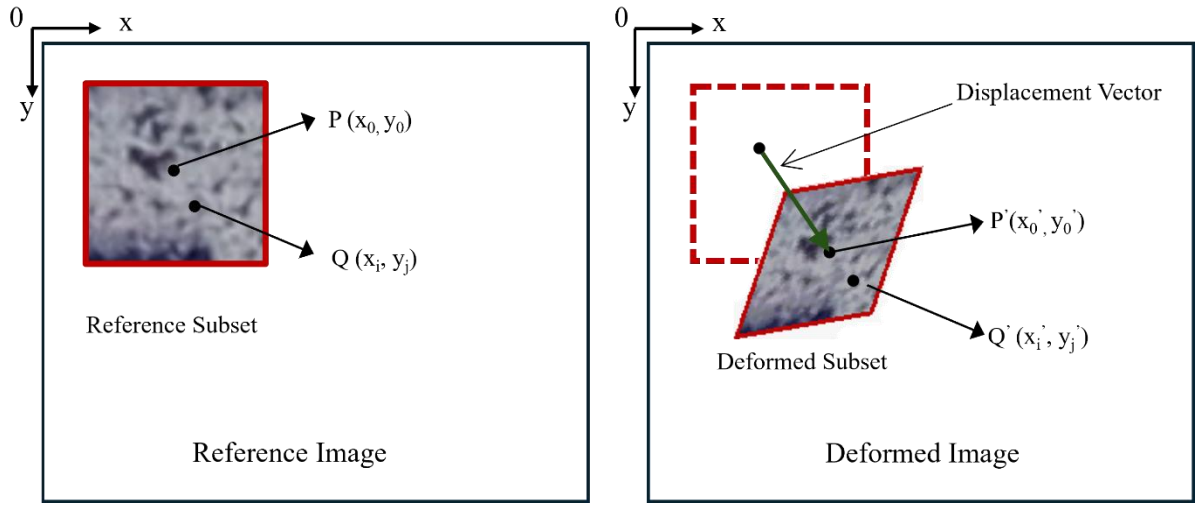


Figure 3.2:Schematic diagram of DIC technique (inspired from [39])

In Figure 3.2, the centre of the square reference subset $P(x_0, y_0)$ yields to $P'(x_0', y_0')$ in the deformed subset with an in-plane displacement Vector. Even though the shape of the reference subsets changes in the deformed image, the set of neighbouring points in the reference subsets can be found in the deformed subset as well. $Q(x_i, y_j)$ is a neighbouring point of P which can be found in the deformed subset at point $Q'(x_i', y_j')$.

To determine full-field displacement and strain, the deformed images can be compared against the reference image. The Region of Interest (ROI), subset size and grid step need to be specified initially to establish the calculation positions. Afterwards, the DIC model traces each point of interest individually in the deformed images. To complete this stage for accurate outcome, a proper shape function and an objective function combining a similarity measure such as a correlation criterion is required to be defined. Subsequently, the defined objective function is optimized through a sub-pixel registration algorithm and a specific interpolation method to determine the deformation vector accurately [24].

3.2.1 Shape Function

The shape function characterizes the deformation of a pixel subset from the reference image to the deformed image. It incorporates translations, rotations and distortions within the subset. According to the shape function [101] or displacement mapping function [102]], the deformed location(x_i', y_j') are:

$$x_i' = x_i + U(x_i, y_j) \qquad (3.1)$$

$$y_j' = y_j + V(x_i, y_j) \qquad (3.2)$$

Where U and V are the displacement components of each subset point and i,j = -M:M.

If the displacements are same for each point in the subsets, zero order shape function is used [101]. However, this shape function is not enough in representing the change in shape of the deformed subset. Therefore, a first order shape function allowing translations, rotation, shear, normal strains and their combinations is used:

$$x_1' = x_0 + U_0 + U_x \Delta x + U_y \Delta y \qquad (3.3)$$

$$y_1' = y_0 + V_0 + V_x\Delta x + V_y\Delta y \qquad (3.4)$$

Where $\Delta x = x - x_0$ and $\Delta y = y - y_0$. The functions can be expanded further using Taylor series expansion to represent deformations that are more complicated in the deformed subset

$$x_2' = x_0 + U_0 + U_x\Delta x + U_y\Delta y + \frac{1}{2}U_{xx}\Delta x^2 + \frac{1}{2}U_{yy}\Delta y^2 + U_{xy}\Delta x\Delta y \qquad (3.5)$$

$$y_2' = y_0 + V_0 + V_x\Delta x + V_y\Delta y + \frac{1}{2}V_{xx}\Delta x^2 + \frac{1}{2}V_{yy}\Delta y^2 + V_{xy}\Delta x\Delta y \qquad (3.6)$$

There are twelve mapping parameters in the equations 3.5-3.6 which in combination can represent a wider range of deformation explicitly [102].

3.2.2 Correlation Criterion

A correlation criterion quantifies the degree of similarity within a reference and deformed subset. The in-plane displacement vector at point "P" in Figure 3.2 is determined by the positional differences between the centres of the reference subset and deformed subset. The correlation criterion needs to be defined ahead for correlation analysis. Based on the mathematical definitions, the correction criterions used for DIC are categorised into four classes: (i) cross-correlation (CC), (ii) sum of absolute difference (SAD), (iii) sum of square difference (SSD), (iv) parametric sum of squared differences (PSSD). Though considering the error caused by mismatching of intensity change model in practical life, zero normalised cross-correlation criterion (ZNCC), zero normalised sum of squared difference (ZNSSD) and PSSD criterion are highly recommended. It has been found in research that these three correlation criteria are equivalent for pattern matching [24]. Among different representations of correlation criterions, Zero Normalised Cross-Correlation ($C_{ZNCC)}$ is used widely [23]. The details of other commonly used cross-correlation criterion and sum of square difference (SSD) correlation criterion are described in [39]. The Zero Normalised Cross-Correlation can be calculated as:

$$C_{ZNCC} = \sum_{i=-M}^{M}\sum_{j=-M}^{M}\left[\frac{\{f(x_i, y_j) - f_m\}\{g(x_i', y_j') - g_m\}}{\Delta f \Delta g}\right] \qquad (3.7)$$

Here, 2M+1 is the length of the subset size and $f(x_i, y_j)$ and $g(x_i', y_j')$ are the reference and deformed images' grey level intensity of the pixel respectively. Besides, f_m and g_m are the mean of selected subsets which can be calculated as:

$$f_m = \frac{1}{(2M+1)^2} \sum_{i=-M}^{M} \sum_{j=-M}^{M} f(x_i, y_j)$$

$$g_m = \frac{1}{(2M+1)^2} \sum_{i=-M}^{M} \sum_{j=-M}^{M} g(x_i', y_j') \tag{3.8}$$

And the Δf and Δg can be calculated as:

$$\Delta f = \sqrt{\sum_{i=-M}^{M} \sum_{j=-M}^{M} [f(x_i, y_j) - f_m]^2}$$

$$\Delta g = \sqrt{\sum_{i=-M}^{M} \sum_{j=-M}^{M} [g(x_i', y_j') - g_m]^2} \tag{3.9}$$

An additional technique to calculate the correlation of the subsets is Zero Normalised Sum of Squared Difference (C_{ZNSSD}) which can be seen below:

$$C_{ZNSSD} = \sum_{i=-M}^{M} \sum_{j=-M}^{M} \left[\frac{\{f(x_i, y_j) - f_m\}}{\Delta f} - \frac{\{g(x_i', y_j') - g_m\}}{\Delta g} \right]^2 \tag{3.10}$$

Here (f_m, g_m) and $(\Delta f, \Delta g)$ are the same as defined in equation 3.8 and 3.9 respectively. From the equations 3.7 and 3.10, it can be noticed that the CC and SSD criteria are related to each other, the ZNCC criterion can be derived from the ZNSSD criterion.

3.2.3 Interpolation

In the deformed subset, some coordinates of point (x_i', y_j') (equation 3.1-3.2) can be located between pixels which is known as sub-pixel location. The intensity of these points should be known to calculate the subpixel displacement. It is necessary for the intensity to be higher to achieve a high correlation value. To determine the intensity of the points in sub pixel locations, interpolation schemes like bilinear interpolation, bicubic interpolation, bicubic B-spline interpolation, biquintic B-spline interpolation and bicubic spline interpolation are used. Images smoothened by B-order spline interpolations are found to have higher accuracy [23], [101], [103].

3.2.4 Local and Global DIC

Based on the fundamental principles of DIC, there are two approaches to implement it named Local DIC and Global DIC. In Local DIC the image is divided into local subset and the correlation is implemented on each subset independently. Some software packages using Local DIC methods are Ncorr [22], VIC 2D [104] etc. On the other hand, every single pixel from the region of interest of the reference image is tracked in the deformed image collectively in the Global DIC method. Global DIC is implemented in the Augmented Lagrangian Digital Image Correlation (ALDIC) [74], P-DIC [105] etc. A schematic diagram on the comparison between Local DIC and Global DIC is shown in Figure 3.3.

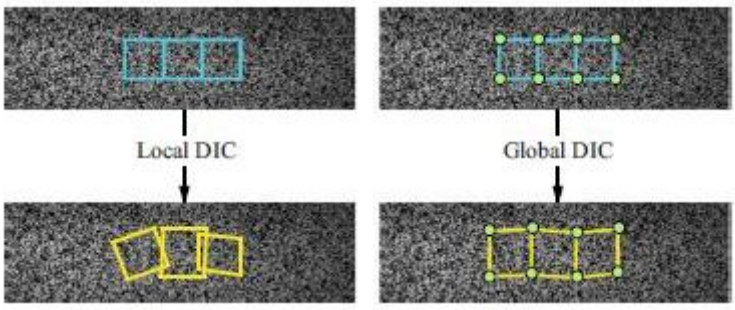
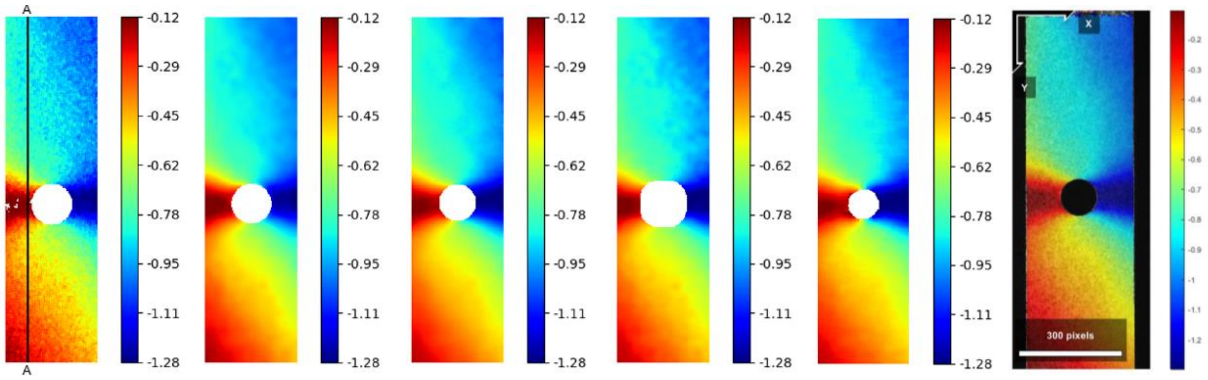


Figure 3.3: Comparison between local DIC and global DIC [74]

3.3 Verification of DIC framework

To verify the accuracy of the proposed DIC framework, it is implemented on some datasets. The datasets used in [67], [74] are some open-source datasets available online. DIC analysis is conducted using the open-source software Ncorr to observe the performance of the software. The results obtained from this verification process match the results of the previous works which verifies the performance of the software. The first example that has been processed is from the Society for Experimental Mechanics (SEM) 2D-DIC challenge simulated dataset [26]. This DIC challenge provides some datasets to validate and verify different DIC software. A "plate-hole" sample image dataset (sample 12) has been processed by Ncorr and the result has been compared with the results from the deformation in Y direction (U_y) analysis in [57] and strain in xy (ε_{xy}) [22]. This sample involves a uniaxial tension of a plate with a hole in the middle. This dataset is used to demonstrate the effectiveness of DIC algorithms in handling complex regions of interests (ROIs). Round-robin type tests are used to compare and validate different DIC analysis codes for this experimental image series.



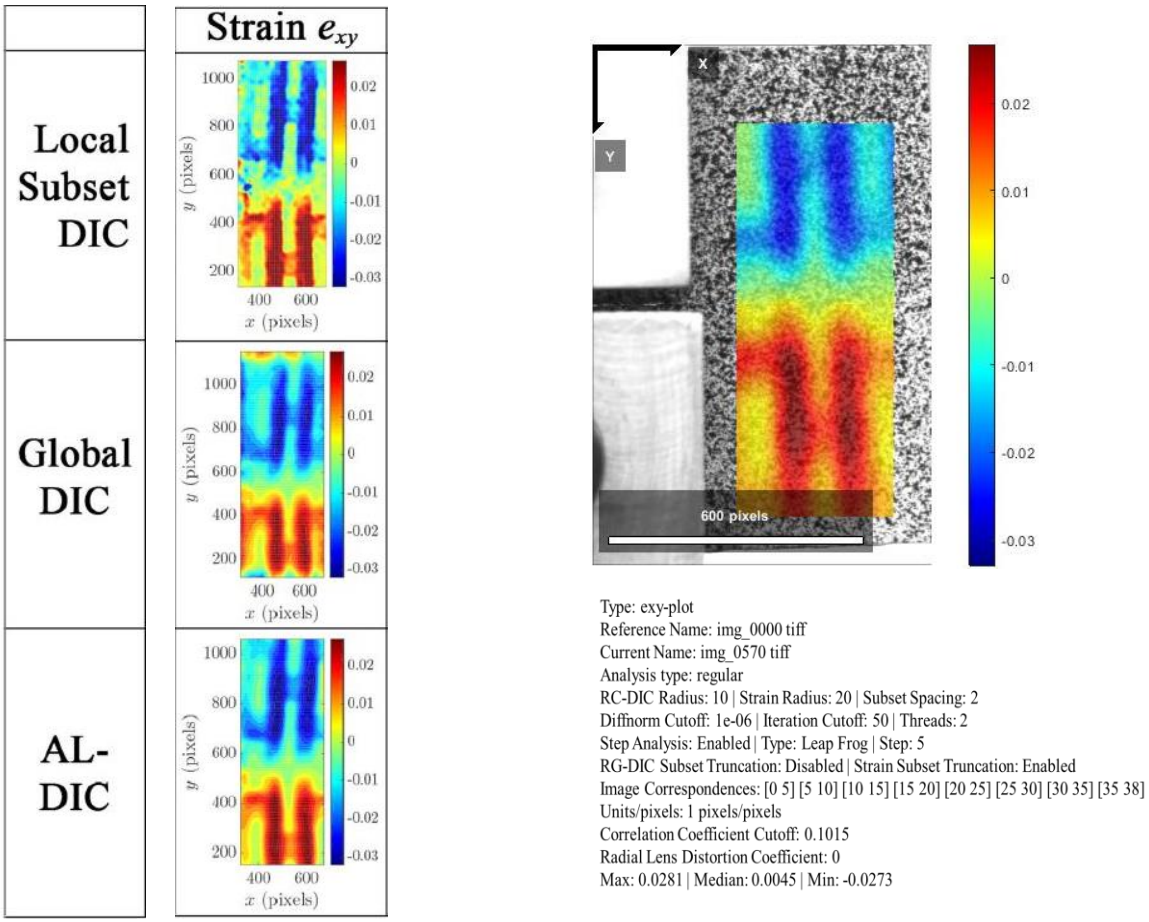
(a) (b) (c) (d) (e) (f)

Figure 3.4: Results from (a) py2DIC, (b) py2DIC smoothed result using Gaussian filter, (c) Ncorr, (d) Vic-2D, (e)DICe from research by [67] and (f) validation test with Ncorr in this research for deformation in Y direction (U_y).

Figure 3.4 depicts the results of DIC analysis by Ncorr in this research and compare it with the results found in [22], [67].

The next analysis is conducted on an image dataset from the experiment of Aveller [106] on the fracture of a heterogeneous material. The 50.8*45.7*9.5 mm specimen is a 3D-printed

compliant acrylic material which is pulled to failure. The results are compared with the results obtained from the research proposing Augmented Lagrangian Digital Image Correlation (ALDIC) [74]. The result comparison is shown in Figure 3.5.



(a) (b)

Figure 3.5: Strain ε_{xy} results obtained from (a) DIC analysis in [74] using different techniques and (b) validation test with Ncorr in this research

The DIC software Ncorr used in this research has been validated by several case studies and methods. The results obtained from the validation tests in this research are found similar to the results in the abovementioned research. Therefore, the model is used for further DIC analysis with the experimental data conducted for this research.

3.4 Design of the Sample

The first step of the experiment is the fabrication of the samples. AM lattice-structured materials are used for this research. 3D models of the samples are prepared in the Fusion360

software and printed through the Fused Deposition Modelling FDM 3D printer. For PLA material printing, FDM-Prusa i3 Mk2.5s-Hopper printer is used with extruder temperature 210ºC and heated bed temperature 60ºC. PLA samples are printed with 0.2mm layer height with 10% gyroid infill pattern and 2.5 shells printed at 60mm/s with standard supports and a skirt-only bed adhesion method. For TPU material printing, FDM-Raise3D E2-Bird printer is used at 60mm/s print speed. These specimens utilize 0.3mm layer height, 100% rectilinear infill and 2.5 shells using PLA supports from a secondary extruder, incorporating a raft bed support. The details of the lattice-structured models sampling can be found in the chart below:

Table 3.2: Sampling matrix

Structure	**Material**	**Size**	**Quantity**	**Speckle**
Cubic	PLA	100mm (5x5x1)	2	No
		50mm (5x5x1)	2	Yes (Spray)
	TPU	100mm (5x5x1)	2	No
		50mm (5x5x1)	2	Yes (Spray)
FCC	PLA	50mm(5x5x5)	1	Yes (Manually)
		100mm (5x5x1)	2	Yes (Spray)
FCCZ	PLA	50mm (5x5x5)	1	Yes (Manually)
		100mm (5x5x1)	2	Yes (Spray)
BCC	PLA	50mm (5x5x5)	1	Yes (Manually)
BCCZ	PLA	50mm (5x5x5)	1	Yes (Manually)

Table 3.2 depicts the sampling matrix of the 3D-printed lattice-structured parts used for this study. Total five lattice structure types were designed and fabricated for this experiment including (i) Simple Cubic Grid structure, (ii) Face Centred Cubic (FCC) lattice structure, (iii) Face Centred Cubic with Z strut (FCCZ) lattice structure, (iv) Body Centred Cubic (BCC) lattice structure and (v) Body Centred Cubic with Z strut (BCCZ) lattice structure. These lattice structures are chosen because the surface of the front struts are normal to the surface and parallel to the camera making them suitable for 2D image analysis. Cubic grid lattices provide baseline deformation behaviour whereas FCC and BCC offer contrasting mechanical responses due to different packing density. At the same time FCCZ and BCCZ demonstrate how structural modifications affect mechanical performance. It is worth mentioning that the decision about the struts dimension, unit cell dimension, and number of repetitions of unit cells in x, y, and z direction are made by considering different factors, including (i) having appropriate image area detected by camera from front surface, (ii) efficiency in material usage as the experiments needed to be repeated several times for different lattice types, and (iii) the consistency of results

between different unit cell repetition in z direction. Following these investigations, the 5*5*1 unit cell dimension is chosen to observe the deformation due to compression in the front plane. The experiment is repeated with 5*5*5 samples to ensure the consistency and reliability. The combination of these samples allows investigation of various failure modes and deformation mechanisms under compression. The images of the samples are provided in Figure 3.6.

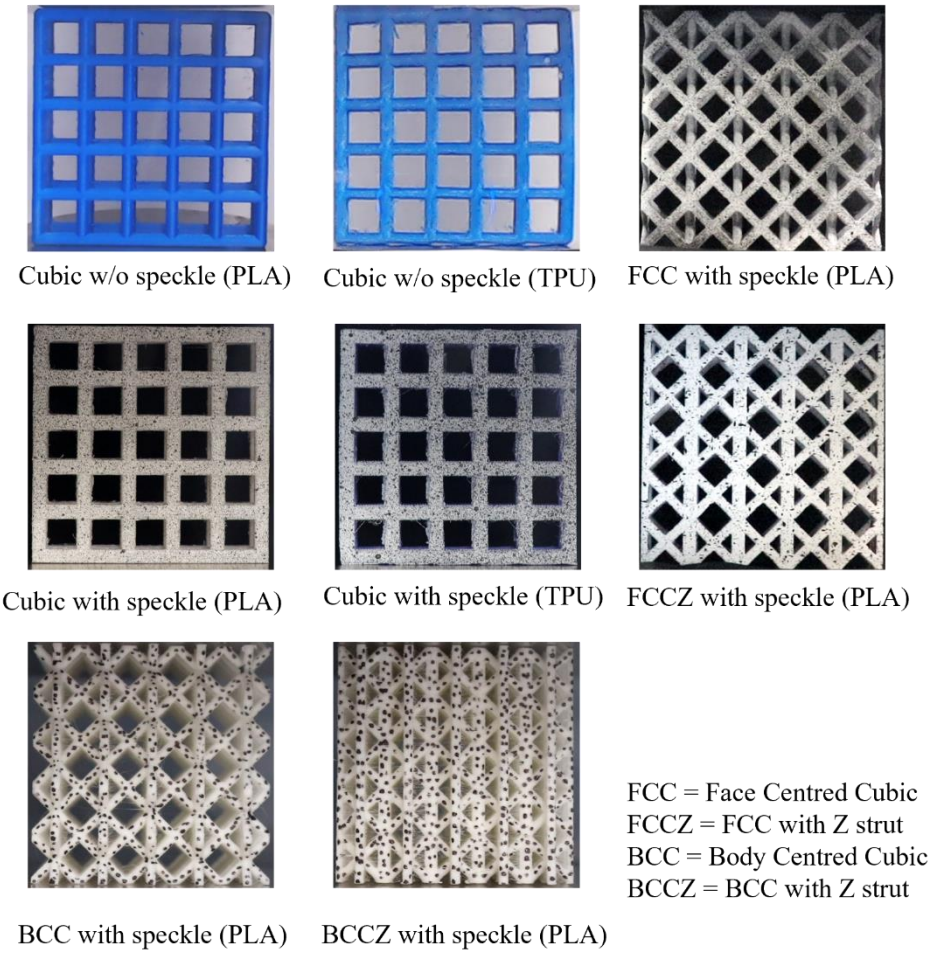


Figure 3.6: 3D-printed lattice-structured samples

All the lattice-structured parts are 3D-printed using Polylactic Acid (PLA) and the simple Cubic Grid lattice-structured parts are printed with Thermoplastic Polyurethane (TPU) materials as well. These two types of materials have different elasticity and load bearing properties. PLA is a thermo-plastic polymer whereas TPU falls under the elastomer category. TPU has lower elastic modulus and is therefore more flexible compared to PLA, which is generally considered as a brittle material with minimal elongation at break [107]. Polylactic Acid (PLA) is a widely

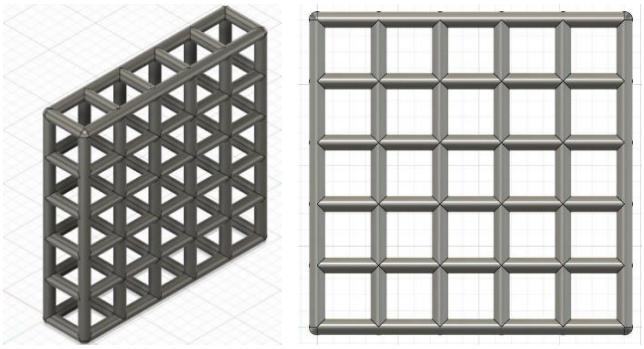
used material for 3D printing because it is environment friendly, economically feasible and easily printable [108], [109]. Thermoplastic Polyurethane (TPU) can be processed as thermoplastic material with hyper elastic and viscoelastic properties as well as rubberlike mechanical performance characteristics [110]. PLA and TPU are chosen for this research due to their contrasting mechanical properties and behaviour, making them ideal for comparative lattice structure analysis. TPU exhibits high flexibility with exceptional elongation of 300-1500%. Whereas PLA is a rigid material with limited elongation of 2-6%. TPU is a semi-soft material which can tolerate large deformation. Therefore, a large deformation can be observed before failure during the experiment. For these reasons, these materials have been chosen to test the accuracy of this proposed methodology on a wider range deformation.

3.5 Additive Manufacturing of Lattice-structured Materials

In this research, four distinct sets of lattice structures were fabricated using AM technology, with each set containing unique geometric configurations and material properties. A total of 16 samples were produced, comprising Cubic, FCC, FCCZ, BCC and BCCZ designs, with each lattice-type containing at least two specimens to ensure experimental reliability and comprehensive analysis of mechanical behaviour. The design and fabrication of the samples are discussed in this section.

3.5.1 Simple Cubic Grid Lattice with Cylindrical Struts

At first, the unit cell of a Simple Cubic structure is designed on Fusion360 and then the lattice is developed with 1 repetition in the x direction and 5 repetitions in both y and z directions. The total dimension of the lattice structure is 24.00mm in the x direction, 100.00mm in the y direction and 100.00mm in the z direction. The struts are cylindrical in shape and the diameter is 5.00mm. Total four samples have been printed with this design out of which two samples are printed with PLA and the other two are printed with TPU. No speckle pattern has been used in this first set of experiments to observe the efficiency of the DIC model on the natural patterns of the sample. The mechanical testing and image acquisition are conducted after the fabrication and preprocessing of the sample.



(a) Cubic Fusion 360 model 3D view (b)Cubic Fusion 360 model front view



(c) Cubic PLA (d) Cubic TPU

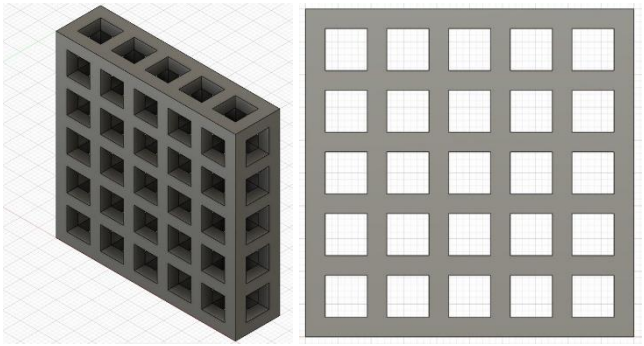
Figure 3.7: Design and prints Cubic Grid with cylindrical struts

3.5.2 Simple Cubic Grid Lattices with Square Cross-sectional Struts

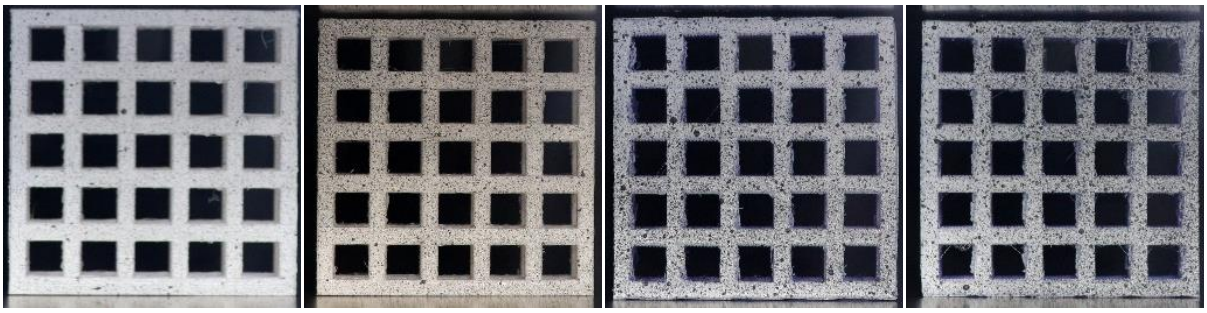
Similar to the first set, the unit cell of the simple Cubic structure is designed first on Fusion360 and then the lattice is developed with 1 repetition in the y direction and 5 repetitions in both x and z directions. The total dimension of the lattice structure is 12.40mm in the x direction, 50.00mm in the y direction and 50.00mm in the z direction. The struts are square in cross-section and the strut thickness is 3.00mm. The difference in dimension from the previous set is to observe the efficiency of the DIC model and other Imaging Technique on different sample sizes and strut types. Total four samples have been printed with this design out of which two samples are printed with PLA and the other two are printed with TPU. Speckle pattern has been used in this set of experiments through black and white spray paints.

In the beginning, the sample is sprayed with white paint to make an even surface for the black speckle pattern. Usually, the surface of the sample is uneven due to 3D printing layers and the drops of the black paint spray create irregular speckle patterns. There is a possibility of smudging, as the black paint accumulates in some spaces on the uneven surface and not dries properly. Moreover, most of the lattice samples were blue in colour and black-white

combination provide a better contrast for the image analysis than combination of blue-white. The white paint creates a blank canvas for the black speckle patterns to be of uniform intensity and create great contrast.



(a) Cubic Fusion 360 model 3D view (b)Cubic Fusion 360 model front view



(c) Cubic PLA (d) Cubic TPU

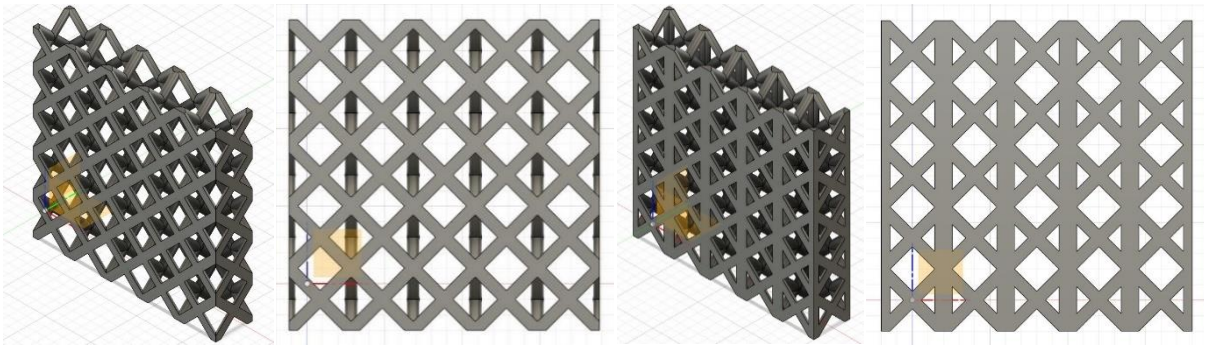
Figure 3.8: Design(a)-(b) and prints(c)-(d) of Cubic Grid with square struts

After the speckle patterns being dried completely, the samples are used for mechanical testing and image acquisition.

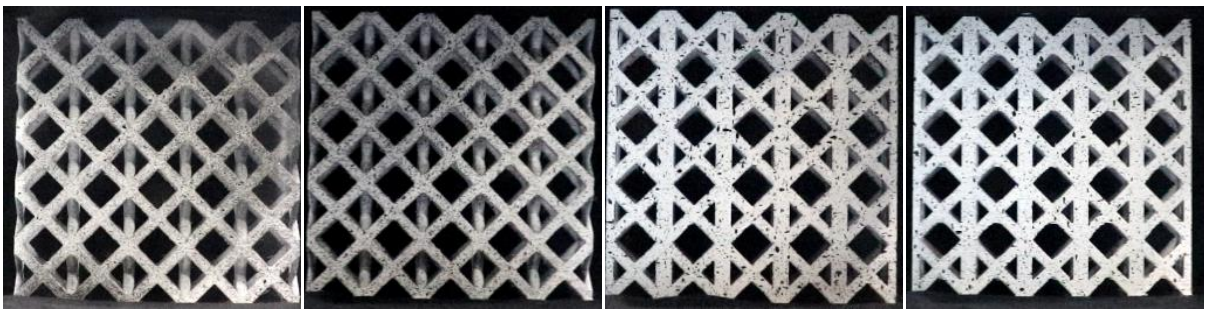
3.5.3 Face Centred Cubic (FCC) and FCC Reinforced (FCCZ) Lattices

To analyse complex deformation patterns, complex geometric structures like Face Centred Cube (FCC) and Face Centred Cube with Z strut (FCCZ) are developed for this research. Initially, the unit cells of the FCC and FCCZ structures are designed on Fusion360 and then the lattices are developed with 5*5*1 repetitions in x, y and z directions. The total dimension of each lattice structure is 100.00mm in the x direction, 20mm in the y direction and 100.00mm in the z direction. The struts are cylindrical in shape and the thickness of the struts in FCC structures are 4.00 mm each. For FCCZ samples, the thickness of the struts at the inside are 4.00 mm each. The thickness of the Z struts on the face are 2.828 mm each. Total four samples

have been printed in this set out of which two samples are FCC lattices and the other two are FCCZ lattices. In this set, PLA is used as material for all the samples. Speckle pattern has been used in this set of experiments through black and white spray paints similar to the previous set of samples. Later, the experiment is conducted on the universal testing machine after the speckle patterns are completely dried out.



(a)FCC fusion 360 model (b)FCCZ Fusion 360 model



(c) FCC Prints (d) FCCZ Prints

Figure 3.9: Design(a)-(b) and prints(c)-(d) of FCC and FCCZ

3.5.4 BCC, BCCZ, FCC and FCCZ Lattices

Four different types of structures have been designed for this set. The types of lattice structures are Body Centred Cubic (BCC), Body Centre Cubic with Z strut (BCCZ), Face Centred Cubic (FCC) and Face Centred Cubic with Z strut (FCCZ). Two samples of each of these lattice-structured parts are 3D-printed and used for the experiment. The unit cells of these lattice-structured parts are repeated 5 times (5*5*5) in x, y and z directions to design these samples in Fusion 360. The dimension of each sample is 50.00 mm in x, y and z directions. The BCC and BCCZ samples are developed to observe the effect of out-of-plane struts on 2D DIC.

The struts are cylindrical in shape except for the ones on the face. The thickness of the BCC, BCCZ and FCC structure struts is 2.00 mm each. For FCCZ structures, the thickness of the Z struts on the face is 1.414 mm. The rest of the strut thickness of FCCZ structure is 2.00 mm. All of the four samples in this set have been 3D-printed with PLA material.

After printing, speckle patterns are provided on the front surface of the samples. Instead of spray painting, black marker pens are used to put on the speckle marks on the samples. Random fine dots are drawn onto the surface of the samples to achieve the speckle pattern. This manual marking technique is used to monitor the effect of a different type of speckle pattern on the image analysis methods used in this research.

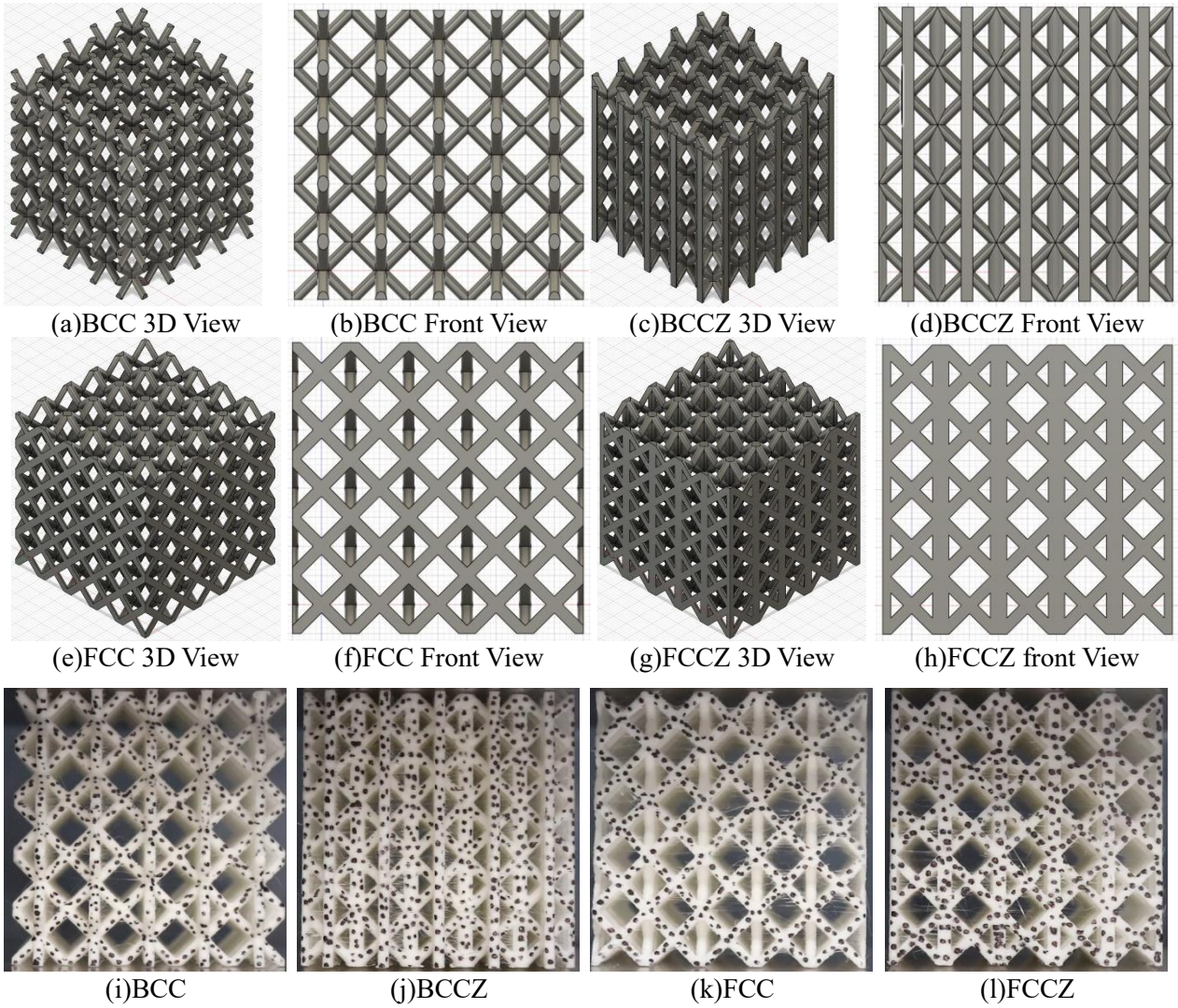


Figure 3.10:Fusion 360 models (a-h) and 3D prints (i-l) for BCC, BCCZ, FCC and FCCZ

Afterwards, the samples are used for mechanical testing and image acquisition.

3.5.5 Speckle Pattern

Speckle pattern has been one of the crucial pre-requisites to conduct DIC on images of deforming structures in this research. For DIC, some random pattern of varying intensity on the surface of the sample is required which creates sufficient contrast and deforms with the sample. If this type of natural texture is absent on the sample surface, some artificial speckle patterns are required to be put on the surface [111], [112]. After the loading, the original surface is deformed and the patterns on the surface move to a new location. Later during the DIC analysis, these unique and random speckle patterns help the model to find the new displaced location of the original point on the surface [113]. Not only the presence of the speckle pattern but also the quality of the speckle pattern affects the accuracy of the DIC results [114]. The speckle patterns should be of high contrast, random, isotropic and should be attached to the sample during the whole experiment. The speckle patterns should also not affect the mechanical properties of the sample [112], [114].

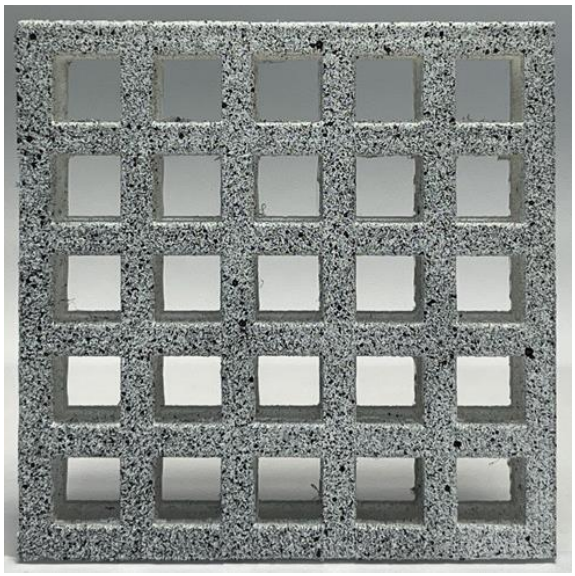
This research has been conducted using both speckled and non-speckled samples to assess the performance of the models used on 3D-printed lattice structured parts. Even though DIC analysis works with natural surface patterns, the patterns need to be distinctive enough for the model to track the ROI. Therefore, one of the purposes of this research is to determine whether 3D printing's inherent texture is suitable for DIC analysis. Furthermore, this research aims to observe the effect of different speckling methods. In this section, the speckling process used during the experiment will be discussed. There are different methods of putting speckle patterns on the sample, such as airbrushing and spraying, spin coating, nanofilm remodelling, lithography, focused ion beam, scratching and abrading, using markers and more. Based on the availability of resources, cost, and usability, spray painting and putting permanent markers have been chosen as speckling techniques here. It is also observed in this research that, while some deformation analysis software relies heavily on the speckle pattern, some of them work well even without the speckle pattern. Moreover, the quality of the speckle pattern also affects the results in some software. Therefore, this research uses samples with three types of patterns. The results of which will be elaborated in Chapter 5.3.

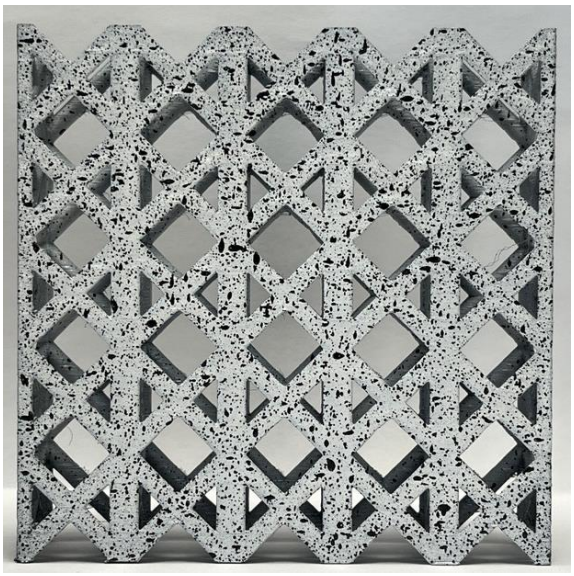


(a) Sample during white painting



(b) Sample during black speckle patterning





(c) Samples after speckling

Figure 3.11: Speckling through spray paint

Spray painting is used on the second and third sets of experiment samples (Cubic Grid with square struts, FCC and FCCZ samples) to create the random speckle patterns. The speckles are approximately 0.1-0.2 mm in size with approximately 0.4-0.5mm spacing. Regular store-bought, inexpensive black and white spray paint cans are used to achieve the desired speckles. Initially, the other surfaces except the front of the sample are covered with masking tape to protect the other parts of the sample from the paint. Only the front surface that would be facing the camera is sprayed with white paint to create a smooth canvas for the black speckles. The

white background also helps establish a high-contrast speckle pattern on the surface. After the white paint is dried out, the black paint is sprayed on the sample to generate the black dots. As the samples are quite small (50mm), the black dots need to be smaller in size as well. Therefore, half of the spray nozzle is covered with tape to control the flow of the spray on the sample. The spraying is conducted from a good distance as well to ensure even distribution.

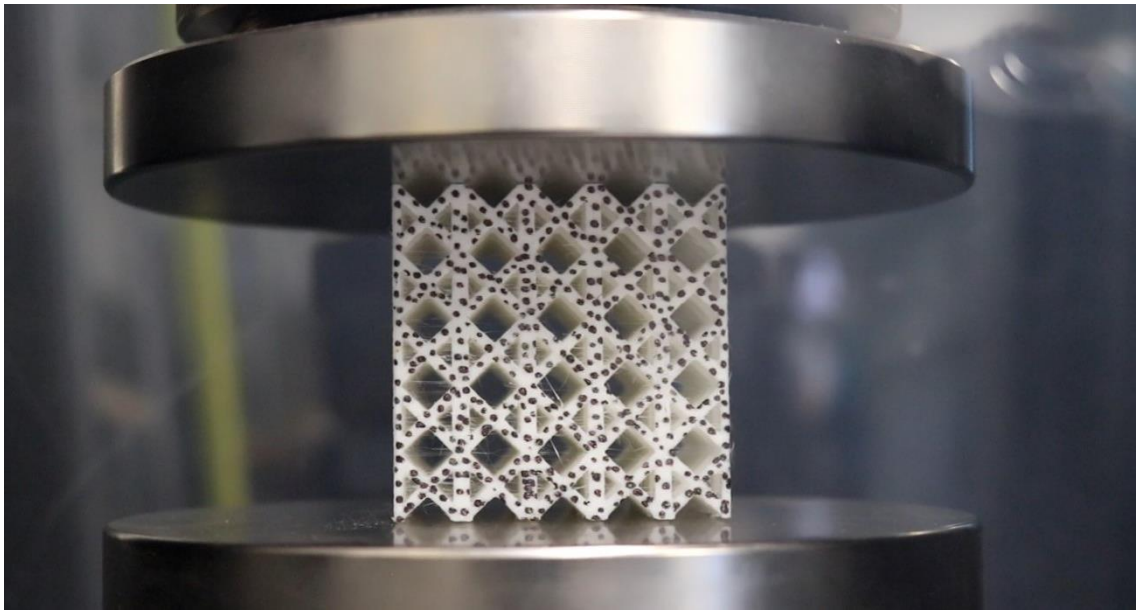


Figure 3.12: Speckling through marker pen

In the BCC, BCCZ, FCC and FCCZ samples with five-unit cell repetition on all axes, black marker pen has been used to put the speckle patterns on the samples. The speckles generated by the marker pens have different size and density which enable the image analysis models to be more dynamic. The marker pens are more cost effective and easy to use as well. The outcome of the speckle pattern through marker pens are shown in Figure 3.12.

3.6 Compression Test Setup

The mechanical compression testing on the samples is completed using Zwick Roell Z050 Universal Testing Machine (UTM). This machine can be used for standardized tests for tension and compression. The maximum load capacity of the machine is 50 kN and the tests are conducted with continuous, static or pulsating load. Compression tests on 3D-printed lattice-structured parts until 10% crush or failure (whichever occurs first) for the first three sets of samples and 60% crush or failure (whichever occurs first) for the BCC, BCCZ, FCC and FCCZ

samples (with 5 unit cell repetition on all axes) are conducted to complete the experiments of this research.

No pre-load is provided at the beginning of the experiment, and 3mm/min speed is used to compress all the samples. TestXpert III testing software is used to obtain the values of the experiment from the machine. The datasheet generated from the software provides the values of crush (%), standard force (N), test time (s) compressive strain (mm) throughout the process.



Figure 3.13: Universal Testing Machine Zwick Roell Z050

After completing the testing machine setup, the experiments are conducted. The sample measurements are noted in the testXpert III software, and the initial distance between the pistons of the compressive tools are specified. The other parameters required for the experiment are also provided before the test starts. Later, the sample is placed inside the machine and the camera is placed in front of the object. The light source is adjusted, and the reflections are mitigated. The details of the image acquisition process will be discussed later in this thesis.

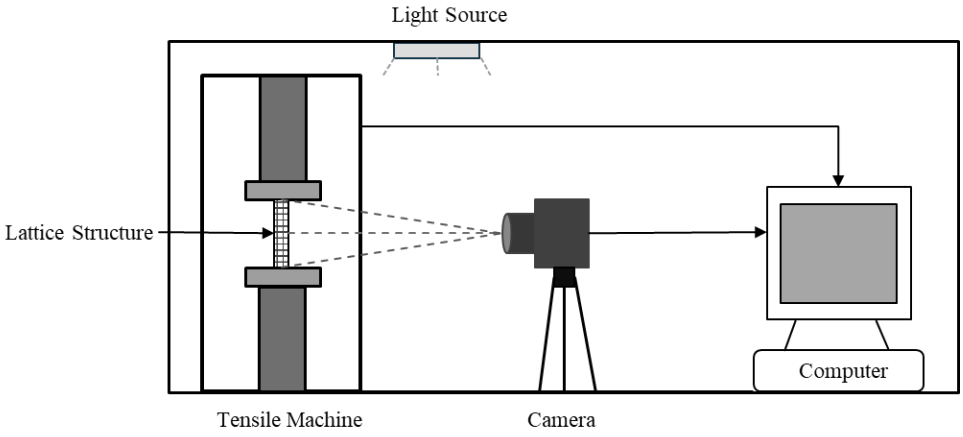


Figure 3.14: Schematic diagram of the experiment

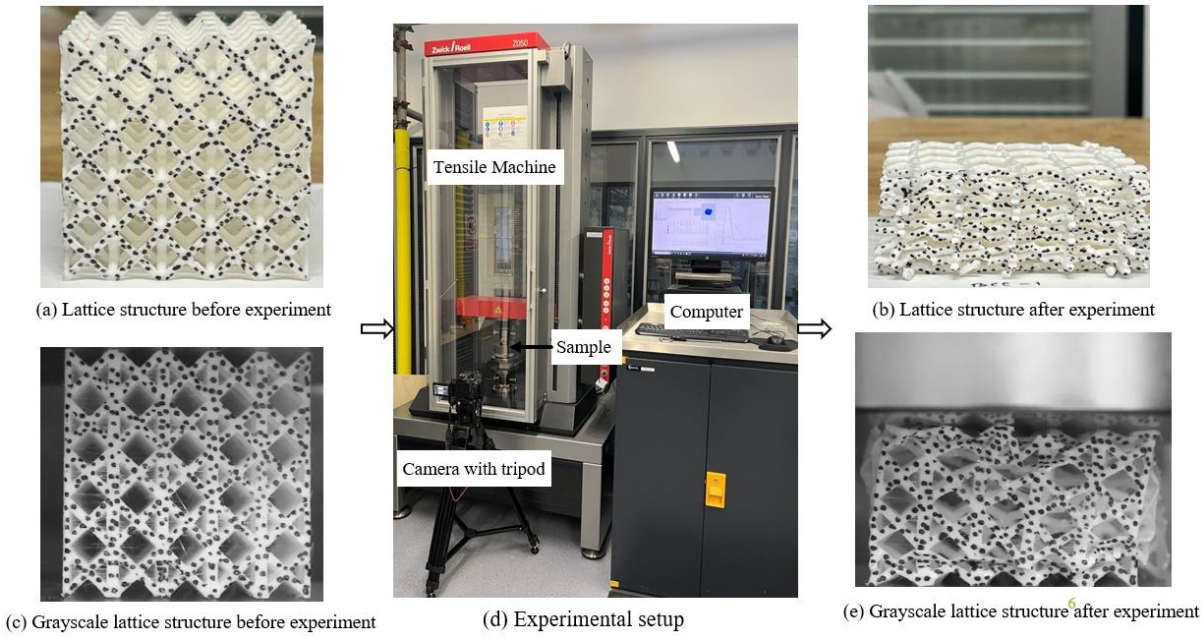


Figure 3.15: The experimental setup and specimens before and after compression test (a)-(c) specimen before starting the test, (d) test setup, (b)-(e) deformed specimens after test

When the test conditions are satisfactory, the experiment is started. The whole compression process is documented through the camera and the loading data are collected through the software. The simple Cubic and FCC, FCCZ samples with 5*5*1 unit cell dimension are subjected to crushing load at 3mm/min speed until 10% crush or the material failure. For materials fabricated with PLA, the failure has occurred before it reached the 10% crush. The samples with 5*5*5 unit cell dimensions have been compressed until 60% crush or failure.

These will be discussed later in the results analysis chapter. The visuals of the samples are documented before and after the test as well. The experimental setup and the specimen condition before and after the experiment are shown in Figure 3.15. The specimen used in this figure is FCCZ lattice-structured material fabricated with PLA having 5-unit cell repetitions in x, y and z directions. This material has been compressed until 60% compressive strain or failure (whichever occurs first) for this research. In this compressed condition, the struts fail randomly in X and Z direction. To avoid this effect on the results, average deformation of left and right edges from the front surface have been used during calculation.

3.7 Image Acquisition

The optical sensors used for image acquisition are digital cameras. The technical details of those cameras, challenges faced during image acquisition process and the pre-processing of images before the analysis will be discussed in this section.

This research aims to establish a comparison between different economically feasible, simple image-based 2D deformation measurement techniques. One of the main objectives here is to evaluate the effectiveness of different 2D DIC approaches which is based on single camera use. As the planer deformation of the samples in x and y directions are considered, use of one camera is appropriate for this study and does not hamper the quality of the results.

3.7.1 Camera Specifications

The image acquisition is conducted using two types of cameras: (i) Canon EOS 850D DSLR camera and (ii) Logitech C920 HD Pro Webcam. The images and specifications of both cameras are given in Table 3.3.

Table 3.3:Camera specifications



Figure 3.16: Canon EOS 850D DSLR Camera



Figure 3.17: Logitech C920 HD Pro Webcam

Brand Name	Canon
Camera Model	EOS 850D DSLR
Screen Resolution	24.1 MP
Display Resolution	4K, 1080p, 720p
Power Source	Battery
Focus	Auto and Manual
Exposure	Auto and Manual
Frame Rate	25-50 fps
Field of View	170 degrees
Dimension	131.0 x 102.6 x 76.2 mm

Brand Name	Logitech
Camera Model	C920 HD Pro Webcam
Screen Resolution	3 MP
Display Resolution	1080p, 720p
Power Source	USB
Focus	Auto and Manual
Exposure	Auto and Manual
Frame Rate	15-30 fps
Field of View	78 degrees
Dimension	43.3 x 94.0 x 71.0 mm

Two types of cameras are used to observe the influence of image quality on the image analysis techniques used in this research. The image resolution of a DSLR camera is much better than the image resolution of a webcam. While the DSLR camera can store the image even without being connected to a computer with the help of a memory card, the webcam needs to be connected to a computer to store the recordings. However, the webcam is cheaper and smaller than a DSLR which increases the acceptability of webcam in regular life.

The cameras are attached to a tripod to stabilise the image acquisition. The tripod allows the camera to move both horizontally and vertically to adjust the position. The height of the tripod is also flexible.

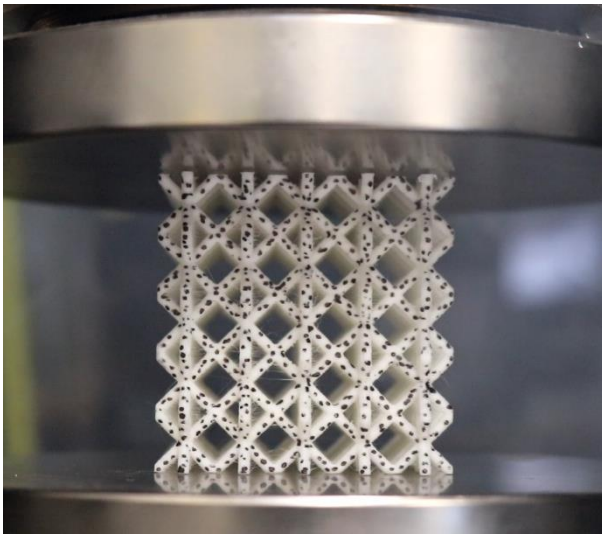


(a) (b)

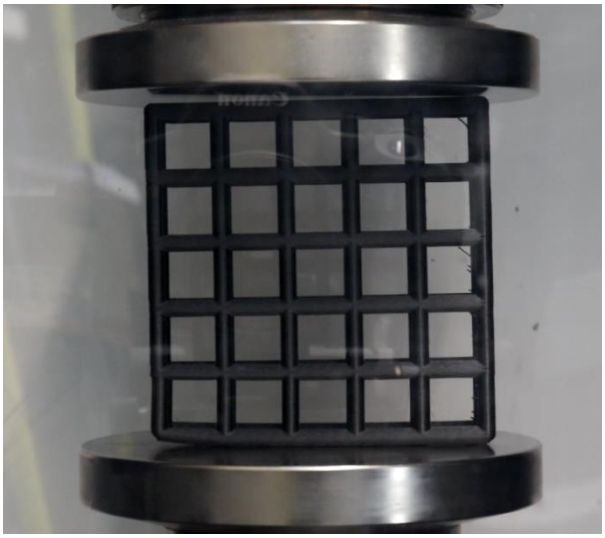
Figure 3.18: Tripod attached with (a) DSLR Camera and (b) Webcam

3.7.2 Minimizing Reflection

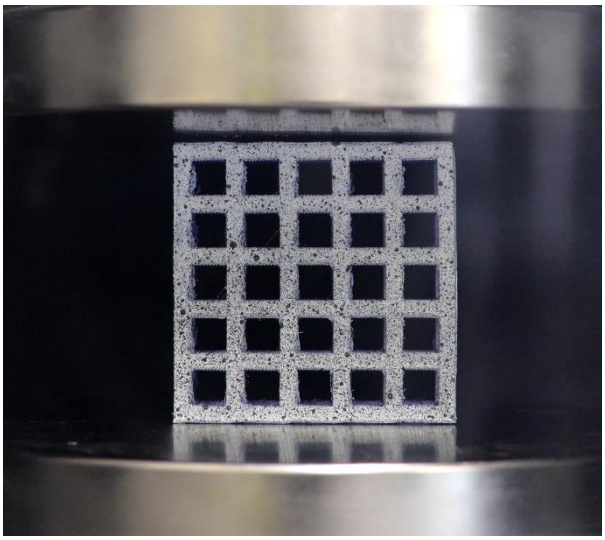
One of the major problems faced during the image acquisition is light reflection. The Universal Testing Machine has glass walls all around which reflects the light and as a result create lighting glare on the images. Besides, the glass door in the front is required to be locked to start the compression test. To mitigate this, white and black backdrops have been used at the back of the machine. Moreover, the stainless-steel compression pistons also reflect a great deal of light which result in error during the image analysis. Black masking tape is used on the pistons to minimize the light reflection from these. However, some illumination remained in the images due to reflection on the front glass door during the image acquisition. These are used to assess the performance of the image analysis models used in this research.



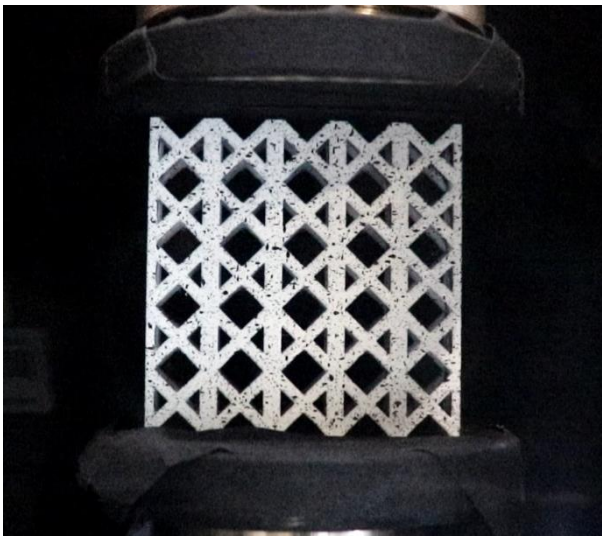
(a) without any backdrop



(b) with white backdrop



(c) with black backdrop



(d) with black backdrop and cover on piston

Figure 3.19: The approaches to minimize the light reflection during image acquisition

As illumination is a common problem, the model needs to be dynamic to address these issues. Therefore, the image acquisition is conducted with the following situations: (a) image acquisition without any backdrop behind the sample, (b) with white backdrop in the background, (c) with black backdrop behind the sample and (d) with black backdrop in the background and black masking tape cover on the compressor piston. A simple white paper is used as a white backdrop at the back of the machine. On the other hand, a piece of black matte cloth is pinned on cardboard to use as the black backdrop behind the sample. The light

reflection on the front glass door is also mitigated in the situation mentioned in (d) with the use of black cloth being held on top of the camera.

3.7.3 Pre-processing of Images

The pre-processing stage of images for this research includes greyscale conversion, region of interest (ROI) identification and background subtraction by segmentation.

3.7.3.1 Greyscale Conversion and ROI Identification

During the experiment, the whole testing process is captured as video footage through the camera. Later the images are extracted from the video at a certain frame interval for each sample. Afterwards, the extracted images are converted to greyscale and then cropped to designate the Region of Interest (ROI). A simple algorithm in MATLAB is used to complete the image pre-processing stage as follows:

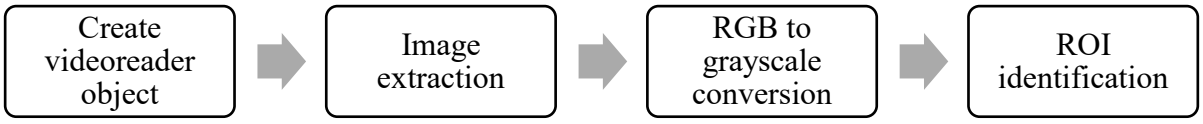


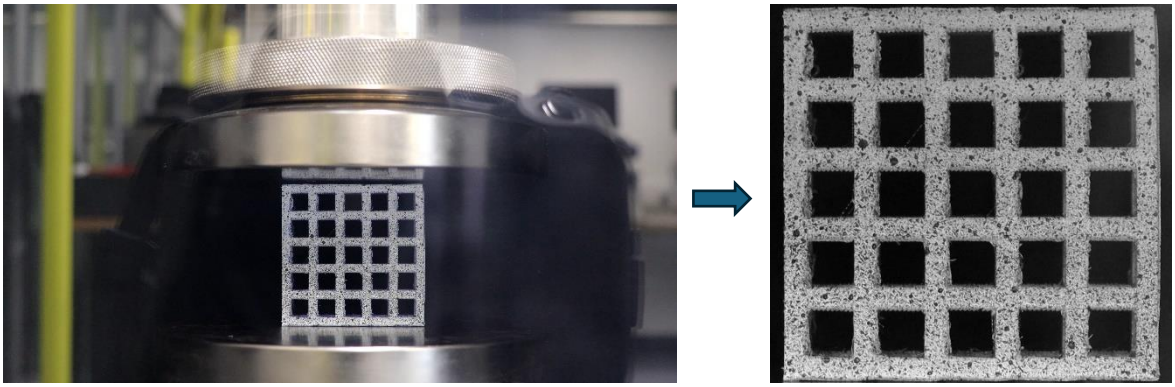
Figure 3.20: Image pre-processing flowchart

An object is created using MATLAB built-in function “Videoreader” containing information about the video file of the experiment. This step is required to read the data from the video file to extract images from that. The duration of the video files varied from 1:00 to 15:00 minutes based on the material properties and types of the lattice structures. As no significant difference has been observed in consecutive frames, each frame of the video is not extracted. Instead, a certain frame interval has been chosen during the image extraction process and the frame interval is determined through a trial-and-error process. The frame interval varied from 60 to 300 depending on the size of the video and the transformation of the object observed with each frame change. Moreover, each frame extraction in the case of larger video files would have resulted in a large number of images. This large number of data would take a longer time to process in the image analysis stage. Table 3.4 shows the details of image extraction and the area for ROI for each sample in the pre-processing stage.

Table 3.4: Image extraction and ROI identification

Sample Name	Camera	Video Duration (minutes)	Total Number of Frames	Extraction Frame Interval	Number of Extracted Frame	ROI Area X*Y (Pixels)
Cubic(PLA)-1	DSLR	02:12	3300	60	53	850, 840
Cubic(PLA)-2	Webcam	02:25	4350	60	66	265, 260
Cubic(TPU)-1	DSLR	04:03	6075	100	60	580, 555
Cubic(TPU)-2	Webcam	04:12	7560	100	64	300, 270
Cubic(PLA)-3	DSLR	01:49	2725	60	44	850, 840
Cubic(PLA)-4	DSLR	01:50	2750	60	44	855, 835
Cubic(TPU)-3	DSLR	02:20	3500	100	34	870, 820
Cubic(TPU)-4	DSLR	02:14	3350	100	33	830, 800
FCC (PLA)-1	DSLR	04:16	12800	200	57	565, 525
FCC (PLA)-2	DSLR	04:11	12550	300	39	560, 525
FCCZ(PLA)-1	DSLR	04:18	12900	200	58	565, 525
FCCZ(PLA)-2	DSLR	04:11	12550	300	39	520, 510
BCC(PLA)	DSLR	11:22	17050	40	185	765, 610
BCCZ(PLA)	DSLR	03:47	5675	30	189	690, 650
FCC(PLA)-3	DSLR	10:32	15800	60	149	650, 530
FCCZ(PLA)-3	DSLR	10:43	16075	60	158	685, 550

After the image extraction, the images are converted to greyscale using MATLAB built in function “rgb2gray”. This function converts the RGB (Red Green Blue) images to greyscale, removing the hue and saturation information and keeping the luminance. Subsequently, the ROI is identified and picked for each sample through the “imcrop” function. The ROI detection process eliminates irrelevant parts of the image, reduces computation time, and decreases unnecessary error [115]. Later, the cropped greyscale images are used for image analysis with or without background removal.



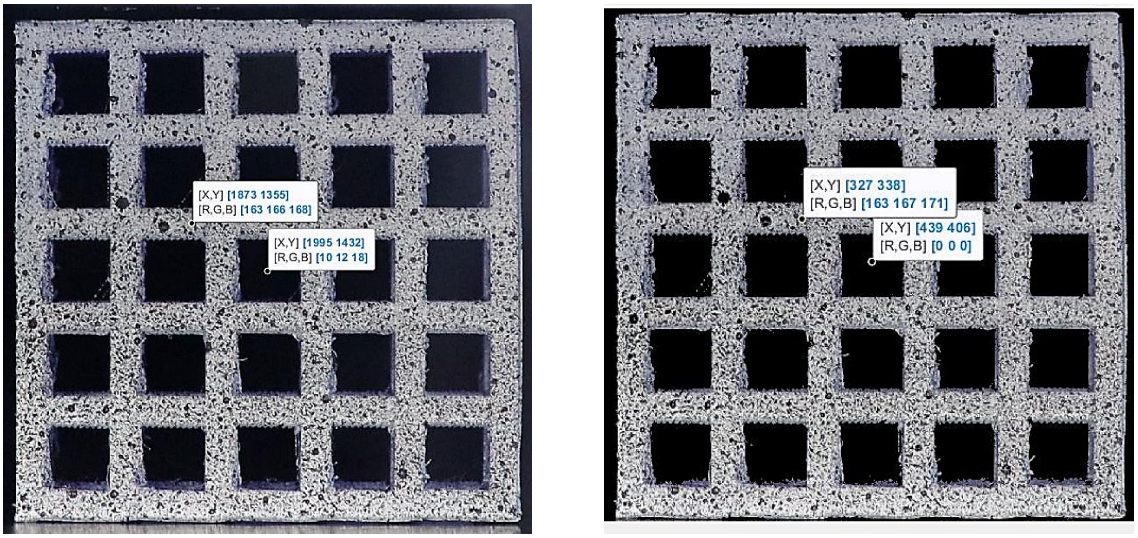
(a) (b)

Figure 3.21: (a) Before and (b) after pre-processing of image

3.7.3.2 Background Subtraction

Instead of having a smooth, solid surface, the samples used in this research have complex shapes with gaps between the struts. Due to this perforated nature of the samples, the background information through the struts of the samples is also detected in the images. However, the purpose of this experiment is to only observe the deformation occurring on the samples due to loading. In this case, this background information creates unnecessary errors during the image analysis. Therefore, one of the approaches of this research is to analyse the images after removing this background information that is being seen through the struts of the lattice-shape structures. The background information is removed from the images using background subtraction.

Background subtraction is the process of eliminating the background information of the image by changing the pixel value below a certain threshold point to zero. The threshold point is determined through trial and error. The threshold value is established by observing the values of the pixels on the sample and the background. Generally, a significant pixel value difference is found between the object and the background. Therefore, a simple MATLAB function is generated to zero those values below the threshold point on the background pixels. During this, the object is localized and converted into greyscale as well.



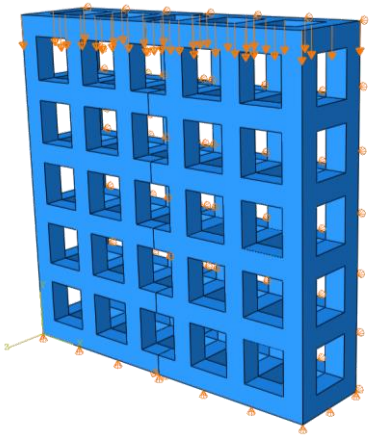
(a) (b)

Figure 3.22: (a) Before and (b) after background subtraction

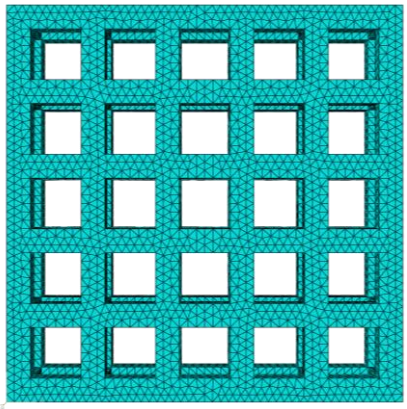
From Figure 3.22, it can be observed that the R, G, B pixel values of the background are 0, 0, 0 after the back subtraction process.

3.8 Finite Element Analysis (FEA)

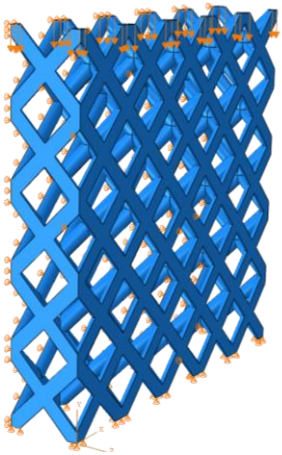
Finite Element Analysis (FEA) has wide application in assessing the mechanical performance and deformation behaviour of lattice structures. It can provide full-field strain and stress distribution through the struts of additive manufactured lattice structures [116], [117], [118], [119]. The FEA is conducted to predict the elastic deformation of the samples and compare them with the results obtained from the image analysis techniques used herein. The simulations are performed in ABAQUS CAE with the models previously prepared in Fusion360. The sample models are entered in Abaqus as 3D deformable parts. Then the appropriate material information (PLA, TPU) is logged in the property module. For PLA, the material behaviour is elastic isotropic, the Young's Modulus is 4107 MPa and the Poisson's ratio is 0.35 [120], [121]. For TPU, the material behaviour is elastic isotropic, the Young's Modulus is 20 MPa and the Poisson's ratio is 0.45 [122]. The model implemented for this FEA is linear elastic. 279962 quadratic tetrahedral elements of type C3D10 and 469599 nodes are employed in the three-dimensional domain. The equation solver used for the analysis is static, general with direct method and full newton solution technique. Four boundary conditions are used for the simulation in Abaqus. The first boundary condition, BC1 is set at the bottom of the structure with 0 mm displacement in the Y direction which works as a fixed support.



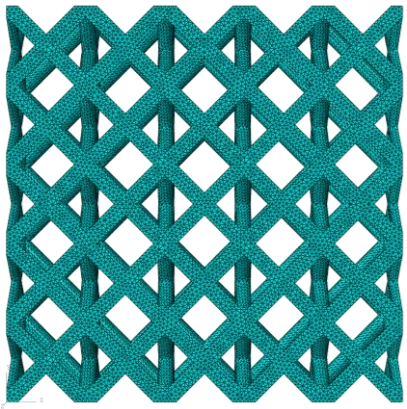
(a) Cubic Grid with boundary condition



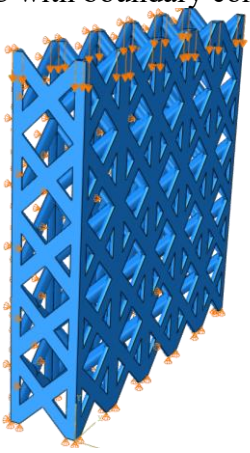
(b) Cubic grid meshed sample



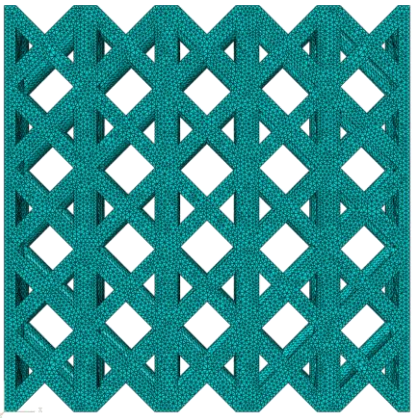
(c) FCC with boundary condition



(d) FCC meshed sample



(e) FCCZ with boundary condition



(f) FCCZ meshed sample

Figure 3.23: Boundary Conditions and meshed samples of different materials on FEA

The second boundary condition BC2 is set with displacement control compression loading in the Y direction at the top of the structure. The third boundary condition BC3 is applied at the

bottom centre of the structure on the symmetrical line to prevent the rigid body motion of the structure in the x direction. As boundary condition BC4, the whole XY plane of the structure is fixed with 0 mm displacement in the Z direction. These parameters are used for all the samples in this research. The boundary conditions and meshed samples are depicted in Figure 3.23 for Cubic Grid, FCC, and FCCZ 3D-printed lattice-structured parts.

3.9 Conclusion

This study's research methodology consists of five technical approaches to measure the deformation of lattice-structured materials that include DIC analysis, imaging technology and FEA. The working principle of DIC, along with the verification of the DIC framework, has been explored in this chapter. The details of material fabrication, experimental process and image pre-processing have been discussed as well. Finally, the finite element parameters are discussed for numerical analysis.

Chapter 4: Deformation Measurement through Image Analysis Techniques

The details of Digital Image Correlation (DIC) and other imaging techniques used in this research to determine the deformation of 3D-printed lattice-structured parts are discussed in this chapter. The results obtained from the analysis are also summarised at the end of this chapter. This research follows 5 technical approaches to determine and compare the deformation occurring on a 3D-printed lattice-structured material under loading. Three analysis techniques including (i) DIC Analysis, (ii) Imaging Technique and (iii) FEA are used to compare and validate the results. The DIC analysis is conducted using two different software. The first is a MATLAB-based open-source software Ncorr and the other is a commercial software Zeiss Inspect Correlation. The analysis in Ncorr is completed using experimental images that have been pre-processed with or without the background subtraction. The details of the experimental setup and pre-processing of the images are already discussed in Chapter 3.

4.1 DIC with Open-Source Software

Ncorr [123] is used in this research due to its easily usable, economically feasible and flexible nature. It is a subset based open-source software suitable for two dimensional DIC analysis. NCorr has gained a lot of interest from the scientific community since its first publication as an open-source software [72]. Ncorr works on a similar principle described in the previous chapter (Section 3.1) by dividing reference images into subsets. The deformation is each subset is presumed to be homogeneous. The coordinate's transformation from reference to deformed subset are considered linear and first order transformation as mentioned in equations 3.3 and 3.4. To find the initial guess and refine the results, two types of correlation criteria- normalised cross correlation criterion (NCC) and parametric sum of squared difference are used respectively. For a nonlinear optimisation scheme, Ncorr uses the Inverse Compositional Gauss-Newton (IC-GN) method. Biquintic B-splines interpolation is also used in this DIC software. The details of the core DIC algorithm and equations can be found in [22]. The subset size (radius) used for the DIC analysis is 10 pixels with subset spacing of 1-2 pixels. The images are required to be in grayscale and in *.tif format before inputting in Ncorr.

The software uses the following workflow: 1) Set Reference Image, 2) Set Current Image(s), 3) Set Region of Interest (ROI), 4) Set DIC Parameters, 5) DIC Analysis, 6) Format Displacement, 7) Calculate Strains. All these stages can be seen on the main GUI of Ncorr in Figure 4.1.

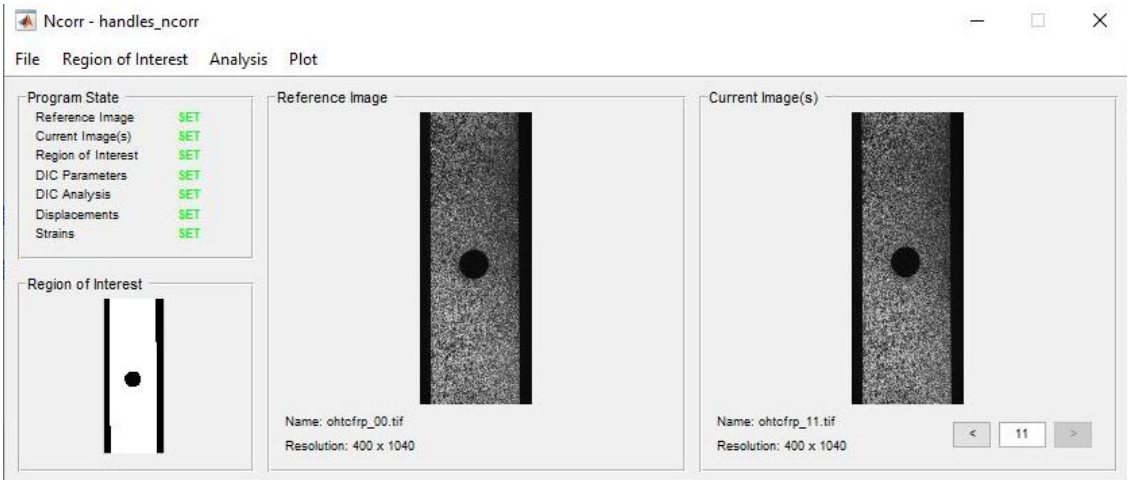
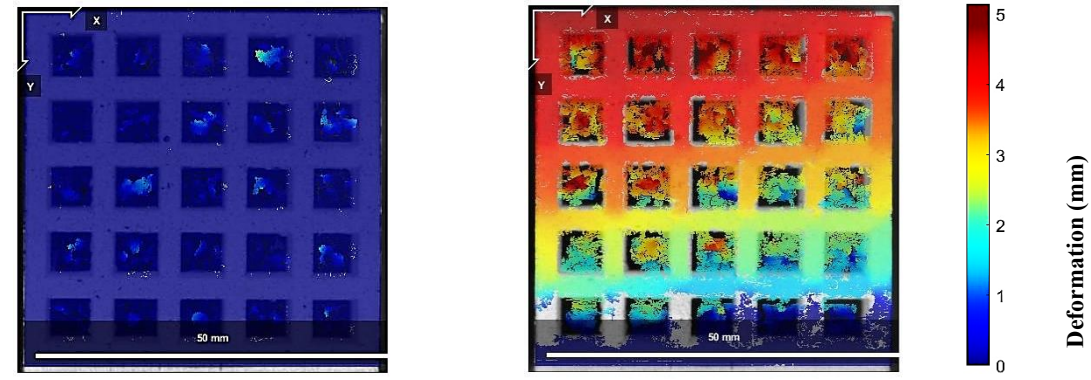
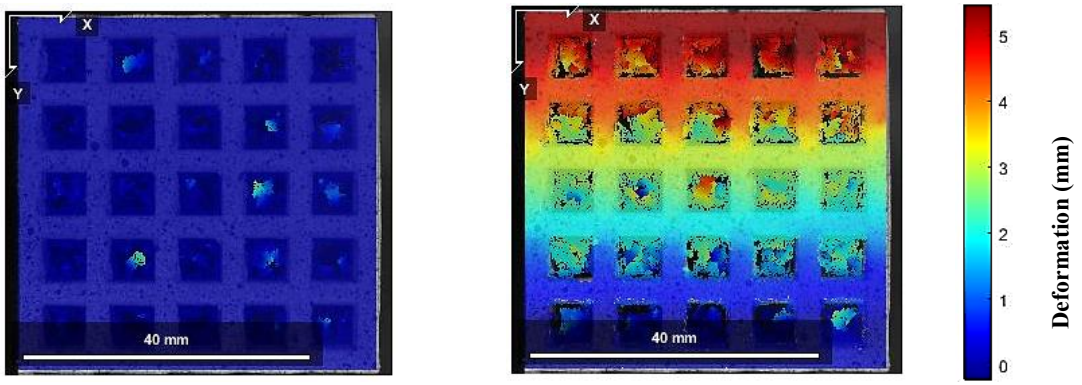


Figure 4.1: Ncorr Main GUI



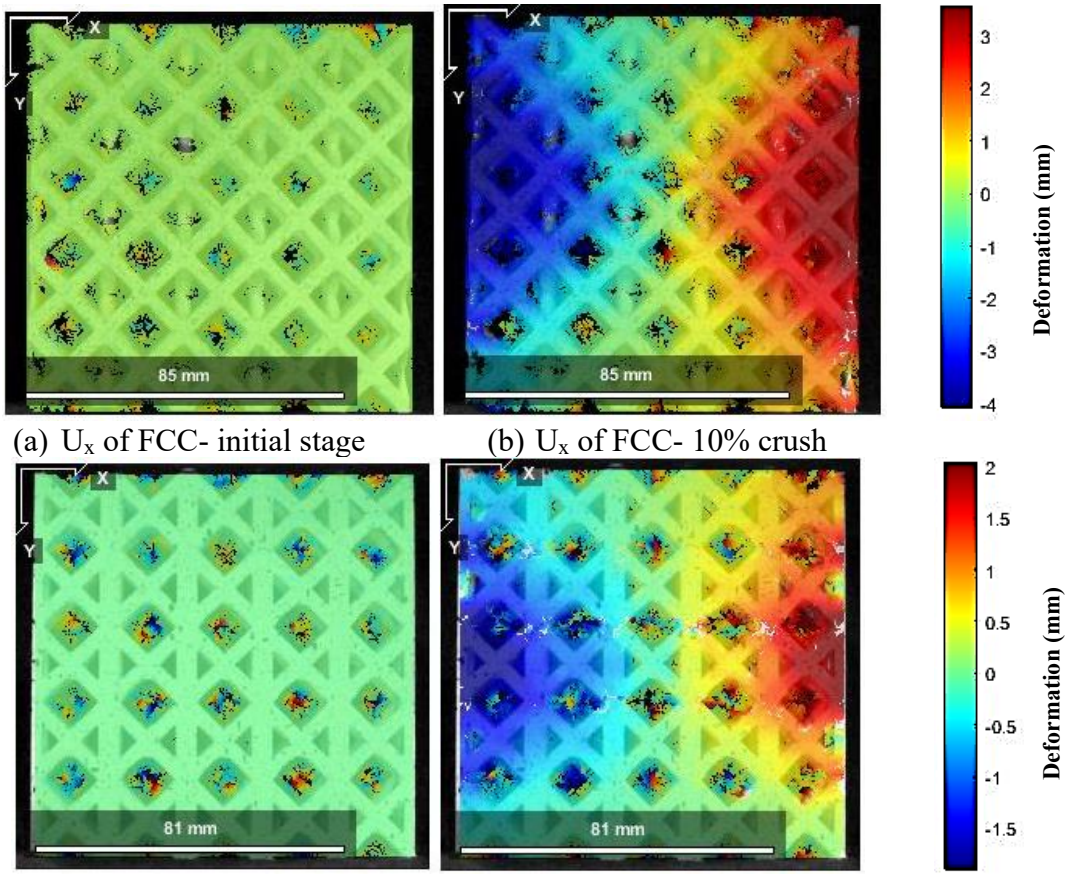
(a) U_y of Cubic (PLA)- initial stage (b)U_y of Cubic (PLA)- 8.3% crush



(c) U_y of Cubic (TPU)- initial stage (d)U_y of Cubic (TPU)- 10% crush

Figure 4.2: Deformation in Y direction results obtained from Ncorr (without segmentation)

The deformation in the Y direction (U_y) results obtained from Ncorr without segmentation are provided in Figure 4.2, and the deformation in the X direction (U_x) results from the same approach in Ncorr are provided in Figure 4.3. The figures portray the reference stage and the final deformed stage of the compression of materials.



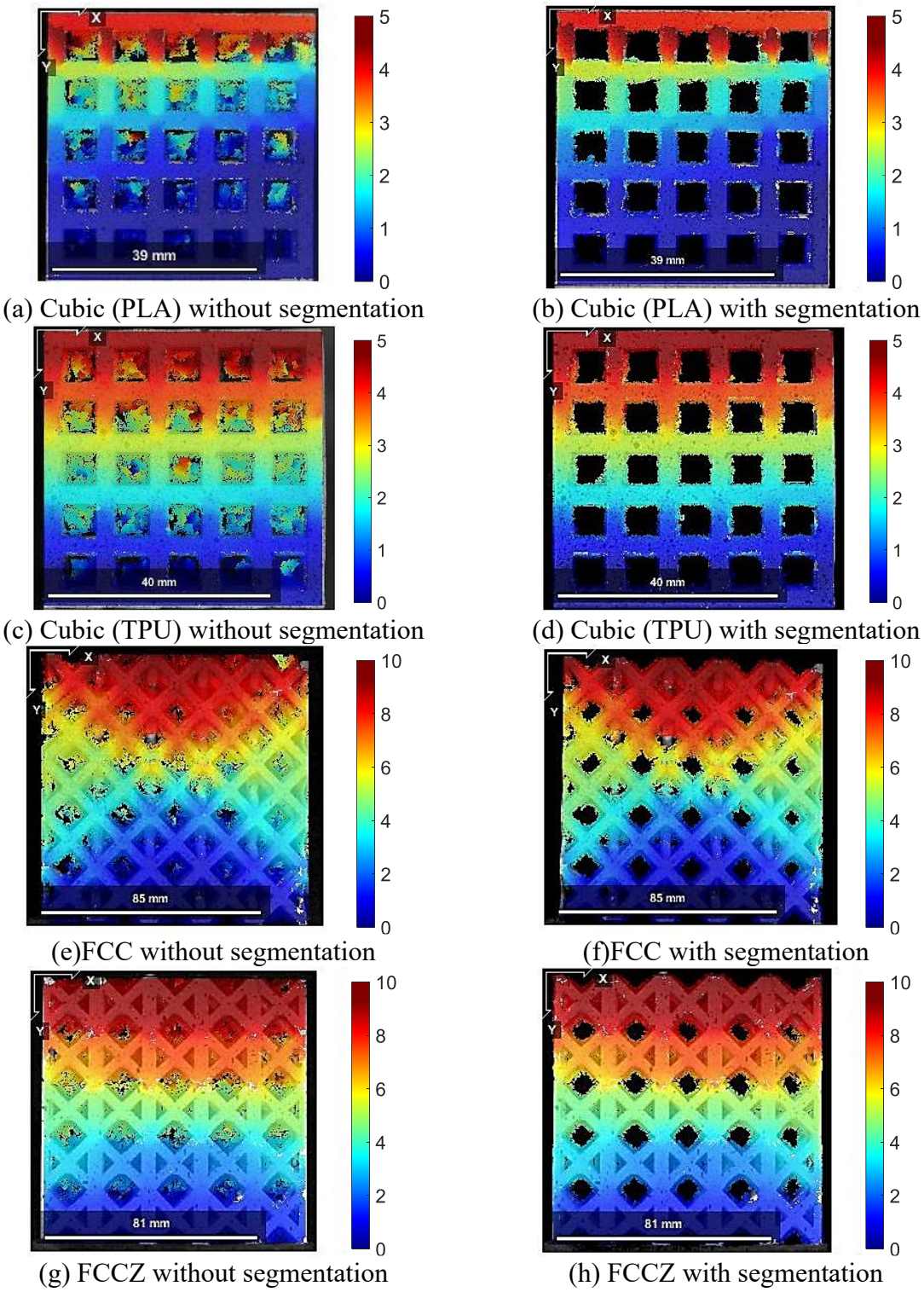
(a) U_x of FCC- initial stage (b) U_x of FCC- 10% crush

(c) U_x of FCCZ- initial stage (d) U_x of FCCZ- 10% crush

Figure 4.3: Deformation in X direction results obtained from Ncorr (without segmentation)

4.1.1 Background Subtraction in DIC with Ncorr

The images are analysed in the software with and without background subtraction to evaluate the efficiency of Ncorr on images of strut-based structures. Strut-based lattice structures have gaps between the struts, and the background is prominent in the images through the gaps. The DIC software needs to be robust enough to distinguish the sample from the background and to be able to detect the deformation on the sample only in lattice structures. Therefore, the effect on results in Ncorr software due to the background subtraction is observed here. The details of the background subtraction process for this research are described in subsection 3.7.3.2. The DIC results in NCorr with and without background subtraction is provided in Figure 4.4.



(a) Cubic (PLA) without segmentation (b) Cubic (PLA) with segmentation

(c) Cubic (TPU) without segmentation (d) Cubic (TPU) with segmentation

(e)FCC without segmentation (f)FCC with segmentation

(g) FCCZ without segmentation (h) FCCZ with segmentation

Figure 4.4: Effects of background subtraction on the U_y results of DIC analysis in NCorr

In Figure 4.4, the displacement plots in the Y direction (U_y) of the samples' deformed images are provided. The deformed images here are the last frames extracted from the video after the loading. In the case of Figure 4.4(a)-(b), it is quite apparent that the background subtraction

process applied in this research significantly improved the results in Cubic Grid structures. For FCC and FCCZ structures in Figure 4.4(c)-(d), the DIC analysis with background subtraction showed adequate improvement in the results than the results without background subtraction.

However, some of the background information through the gaps between the beams of the lattice structure have not been fully eliminated. This is because FCC and FCCZ are complex lattice structures with angled beams. The angled beams in the back layer are more visible through the gaps in FCC and FCCZ lattice structures than the Cubic lattice structures due to the viewing angle. The background information except the pixels of the background beams has been removed through the approach tried in this research. The background beams could not be removed because they have the same pixel values as the beams on the face of the structure. Any attempt to remove those pixels would have resulted in the removal of some of the pixel information of the frontal beams as well. The main focus of this research is to obtain the deformation data of the frontal face of the lattice structure accurately while the main challenge is keeping the background information through the gaps of the lattices at bay. This is why, in FCC and FCCZ structures, the background information could not be completely removed. Nevertheless, DIC analysis in NCorr with the background subtraction model provided better results in all structures than DIC analysis without the segmentation.

DIC analysis in NCorr without background removal is a straightforward process with less pre-processing effort. However, the object detection accuracy in the case of strut-based structures such as lattices is low by comparison. Therefore, background subtraction will be highly recommended for DIC analysis in NCorr.

One of the main advantages of this background subtraction or segmentation process is that it removes unwanted background information in the case of lattice-structured parts. Which in turn makes it easier for the DIC software to detect the deformation of the structure only. The model is quite simple as well, so it takes little time and computational effort to complete the process. However, if the background and the structure have the same pixel value i.e. both having the same colour, the accuracy of the model is limited. The details of the effect of the same pixel values in the background and foreground are discussed in section 5.6.

4.2 DIC with Commercial Software

Commercial Software Zeiss Inspect Correlate [68], formerly known as GOM Correlate Software [124] is used in this research for DIC to investigate the full-field deformation behaviour of 3D-printed lattice-structured materials under compression loading. This software has been chosen for its proven reliability in capturing complex surface deformation and its widespread adoption in the research community. The algorithm of the software is close sourced, and this is the most cited commercial software among the others [72]. The investigation aims to quantify local displacement fields at critical points, specifically the edge midpoints, to validate computational models and understand the mechanical response of different lattice configurations under loading conditions.

The 2D DIC analysis in Zeiss Inspect Correlate is conducted through the following workflow: 1) Import Files (Deformation Image), 2) Define 2D Scale, 3) Create Surface Component, 4) Create Alignment, 5) Inspect All Visual Actual Elements. The main GUI of the Zeiss Inspect Correlate can be seen in Figure 4.5.

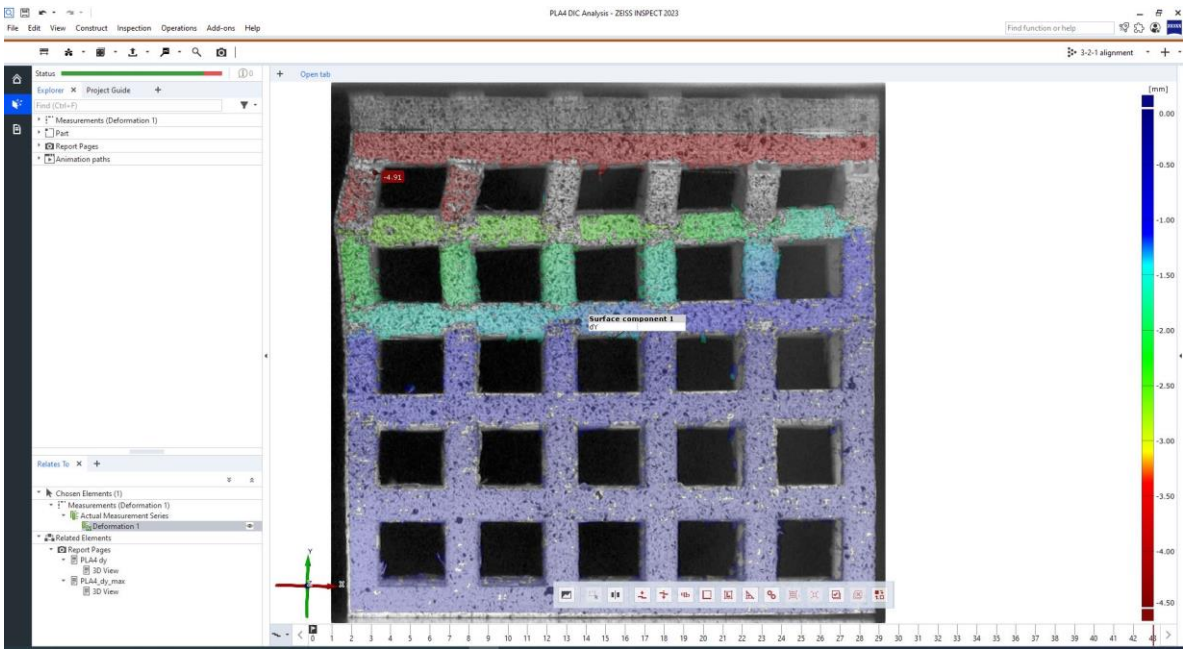
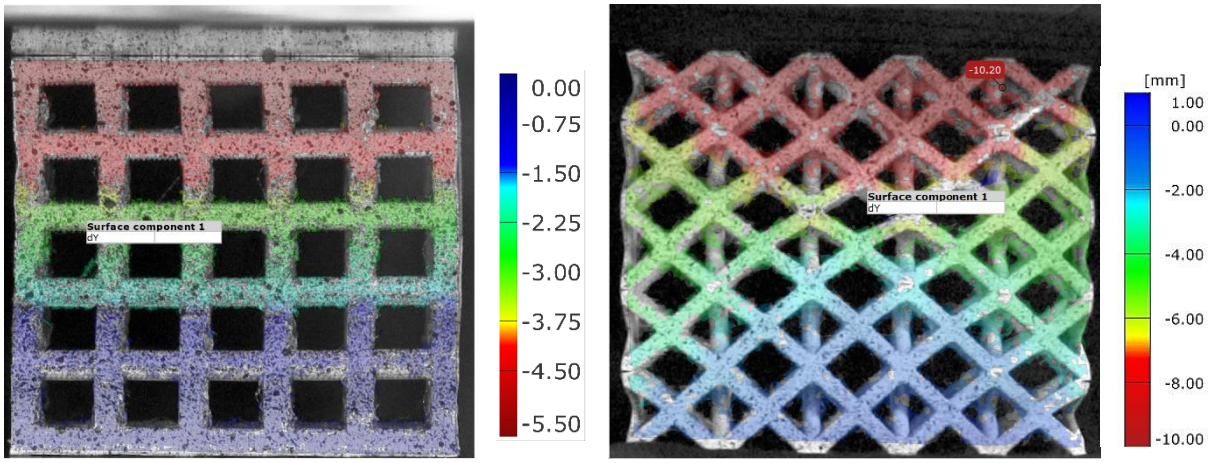


Figure 4.5: Zeiss Inspect Correlate GUI

The images are not required to be in greyscale and the videos can be straightly uploaded here for analysis. The frames of the video can be seen in “Manage Stage” option and the required frames can be selected while deleting or disabling the unnecessary ones.

4.2.1 Performance Evaluation of the Software

One of the strong points of this software is the accuracy in detecting the foreground. This software exhibits high accuracy in identifying the struts of the lattice structure from the background and providing deformation plots. Therefore, no segmentation or background removal is required in the pre-processing stage of DIC Analysis in Zeiss Inspect Correlate. However, the accuracy of the foreground detection is more accurate for Cubic Grid Lattice Structures compared to FCC or FCCZ Lattice Structures. The results obtained from the DIC analysis in Zeiss are provided in Figure 4.7.

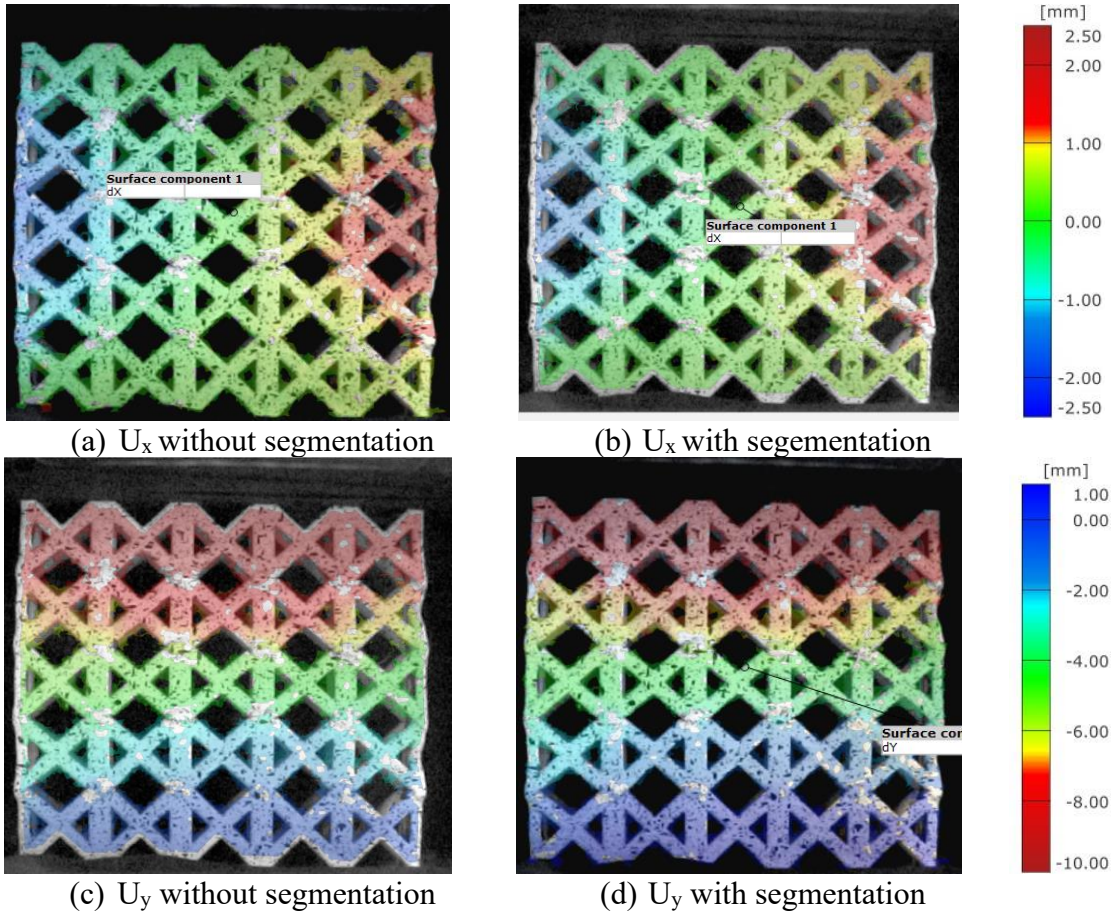


(a) Cubic Sample (b) FCC Sample

Figure 4.6: Performance evaluation of Zeiss without segmentation for U_y

In Figure 4.6, the displacement plots of deformation in the Y direction (U_y) are demonstrated for (a) Cubic Grid Lattice Structure (TPU) and (b) FCC Lattice Structure without segmentation. The images are analysed without any segmentation or background removal pre-processing. The preprocessing of these images included RGB to greyscale conversion and ROI detection. It is visually apparent from Figure 4.6(a) that the performance of Zeiss Inspect Correlate in detecting the foreground in the case of Cubic lattice structure is quite accurate. However, in Figure 4.6(b), the object detection faces the same problem as described in 4.1.1. Due to the

nature of the lattice structure and angle of view, some of the struts from the background layer of the structure are detected in the analysis.



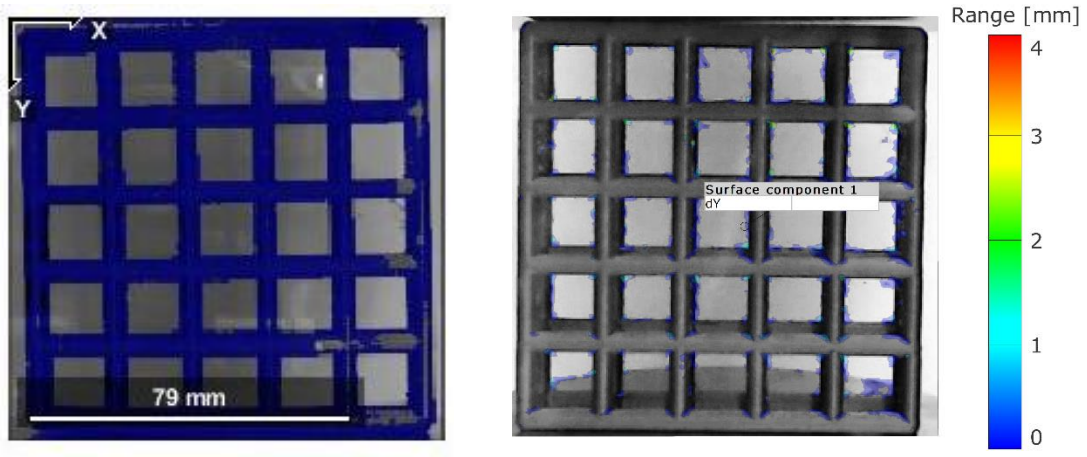
(a) U_x without segmentation (b) U_x with segementation

(c) U_y without segmentation (d) U_y with segmentation

Figure 4.7: Performance evaluation of Zeiss with and without segmentation for FCCZ

Figure 4.7 depicts the effect of segmentation in the pre-processing stage for DIC analysis in Zeiss for (a)U_x and (c)U_y without segmentation and (b) U_x and (d) U_y with segmentation respectively for FCCZ samples. For the images in Figure 4.7(b) and (d), the background subtraction model described in the previous subchapter has been applied to observe the outcome of the result. Figure 4.7(a) and (c) are provided to show the comparison between the DIC analysis including and without the background subtraction. Comparative analysis of displacement fields between segmented and non-segmented images demonstrates negligible differences in measurement accuracy and deformation plot. The deformation plots demonstrate that Zeiss has an effective segmentation capability. This functionality eliminates the necessity for additional pre-processing for complex lattice geometries.

Even though Zeiss is a the state-of-the-art commercial DIC software, it reveals limitations in pattern recognition capabilities. A significant constraint is observed in the software's ROI detection while analysing images of samples without speckle patterns. The object detection without speckle pattern visually demonstrates poor accuracy contrary to the accuracy found in Ncorr. While Zeiss demonstrates good ROI detection with standardised speckle patterns (Figure 4.6, Figure 4.7), its performance notably decreases when analysing samples with manual marker-based patterns or natural surface textures only. Figure 4.8 shows the object detection capability of (a) Ncorr and (b) Zeiss with a Cubic sample without any speckle pattern in the reference or initial image. Ncorr has more versatile detection capabilities contrary to Zeiss's ROI detection capability.



(a) DIC Analysis in Ncorr (b) DIC Analysis in Zeiss

Figure 4.8: Comparison of DIC Analysis without speckle patterns

This observation, while qualitative in nature, highlights a critical consideration in DIC software selection. It is in the case of applications where standardised speckle pattern application may be impractical or when working with specimens featuring natural surface textures. More details of the effect of speckle patterns on different image analysis techniques will be provided in section 5.3.

4.3 Calculation of Deformation through Imaging Technique

Besides two-dimensional DIC, Imaging techniques have been applied to this research to determine the deformation of the lattice-structured parts through image analysis. Two imaging techniques have been applied to the sample image datasets collected from the experiments: (a) deformation analysis through fixed points and (b) deformation analysis by tracing all the points.

4.3.1 Fixed-Points-Based Deformation Analysis

In this technique, a number of fixed points were selected on the undeformed image on X and Y coordinates shown in Figure 4.10. Those points were traced on all frames of the recorded images of deformation of an object. The distances in X and Y coordinates between the undeformed and each deformed image were measured. This distance in pixel location denotes the change of position of the object on each coordinate. A calibration factor is then used to convert the distances from pixel to physical parameters (mm). It should be mentioned that the calibration factor is material specific and depends on the distance between the camera lens and object. Therefore, different calibration factors were used for different materials. Afterwards, all of these points are plotted to obtain a deformation diagram of the whole structure. Figure 4.9 demonstrates the workflow diagram of this technique.

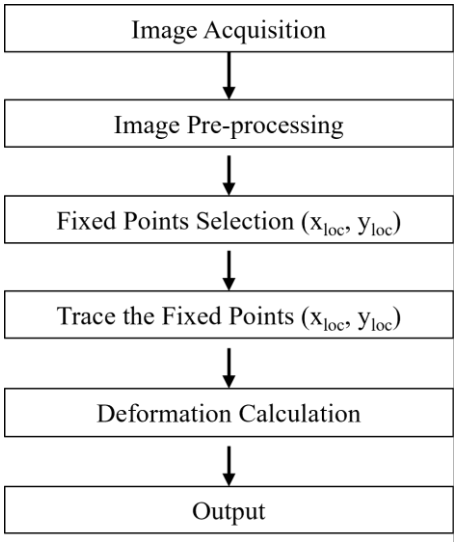


Figure 4.9: Workflow of deformation analysis through Fixed Points

The workflow presented in Figure 4.9 is implemented with MATLAB R2023a through an algorithm model developed for this research. After the image acquisition, the images are pre-

processed. The pre-processing of the images includes ROI detection, image segmentation, RGB to greyscale conversion and image binarization. The details of image acquisition and image pre-processing are discussed in Section 3.7

4.3.1.1 Fixed Point Selection and Tracing

The fixed points across the length and width of the sample are selected by taking five locations in each direction equally distanced from each other. Total five positions in the x direction (x_{loc1}, x_{loc2}, x_{loc3}, x_{loc4}, x_{loc5}) and 5 positions in the y direction (y_{loc1}, y_{loc2}, y_{loc3}, y_{loc4}, y_{loc5}) are selected. The lattice structures used in this research have five repetitions (unit cells) in x and y directions each. The five points are the midpoints of the struts of those five unit cells in both directions. This model can measure deformation at any location of the structure. These five points are chosen to determine the deformation of the midpoints of each unit cells in this approach. These five positions in each direction will trace two more points on each beam of the lattice structure. Those two points are the two edging points of the beam. For horizontal beams, those edging points are the points of the top edge (y_{top}) and bottom edge (y_{bottom}). For Vertical beams, those edging points are the points of the left edge(x_{left}) and right edge (y_{right}).

So, the fixed points set becomes:

$$\text{Top:} \quad x_{loci}, y_{locj} = x, y \in Im\,(x, y) = 1\,; \quad \begin{matrix} i = \{1,2,\ldots.,5\} \\ j = \{1,2,\ldots.,5\} \end{matrix} \qquad [4.11]$$

$$\text{Bottom:} \quad x_{loci}, y_{locj} = x, y \in Im\,(x+1, y+1) = 0\,; \quad \begin{matrix} i = \{1,2,\ldots.,5\} \\ j = \{1,2,\ldots.,5\} \end{matrix} \qquad [4.12]$$

Here, Im = Image, x = {1, 2, ..., width of the object}, y = { 1, 2, ..., height of the object}. $Im\,(x, y)$ and $Im\,(x+1, y+1)$ are the pixel coordinates of the object in the image. Similar equations are applied to determine the fixed points for deformation in x direction.

The main principle that this model follows is checking all the pixel location's value downward (for y direction) or rightward (for x direction) from the five fixed positions mentioned earlier. The binary images have a pixel value of 1 in the locations with the object and the rest of the locations in the images have a pixel value of 0. For the y direction, the model searches from top to vertically straight downward until finding the first location with pixel value 1 in x_{loci} and names it y_{top}. That point y_{top} is the top edging point of the beam of the lattice structure. The

model then moves downward until it finds pixel value 0 again, selects the last point before the 0-pixel value and names it y_{bottom}. The position with the pixel value 0 means the beam has ended and there is no beam or object in that location. The object can be found at the location just above that point and that position will be y_{bottom}. Then, the model moves downward and searches for the next location with pixel value 1. Which means the top edge of the next beam has been found. The model iterates this process for all the fixed points and beams. A similar iteration is carried out from left to right to find the fixed points to detect deformation in the x direction. The iteration stops when the model reaches the height or width of the object.

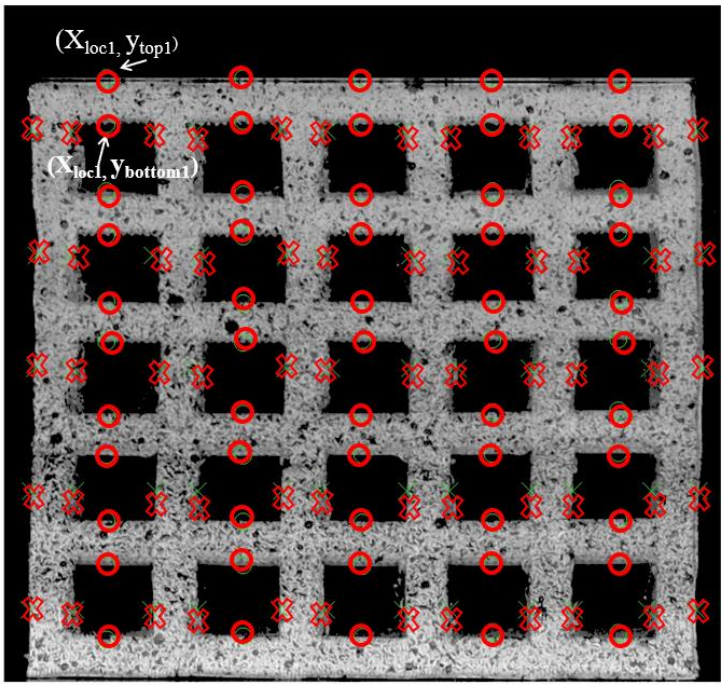


Figure 4.10: Fixed Points for deformation analysis.

The fixed points for Cubic Grid lattice-structures materials are demonstrated in Figure 4.10 The points denoted with circles in the figure display the selected points for determining deformation in the y direction. The points denoting with cross marks (x) display the selected points for determining deformation in the x direction. The algorithm explained earlier is demonstrated in the flowchart in Figure 4.11

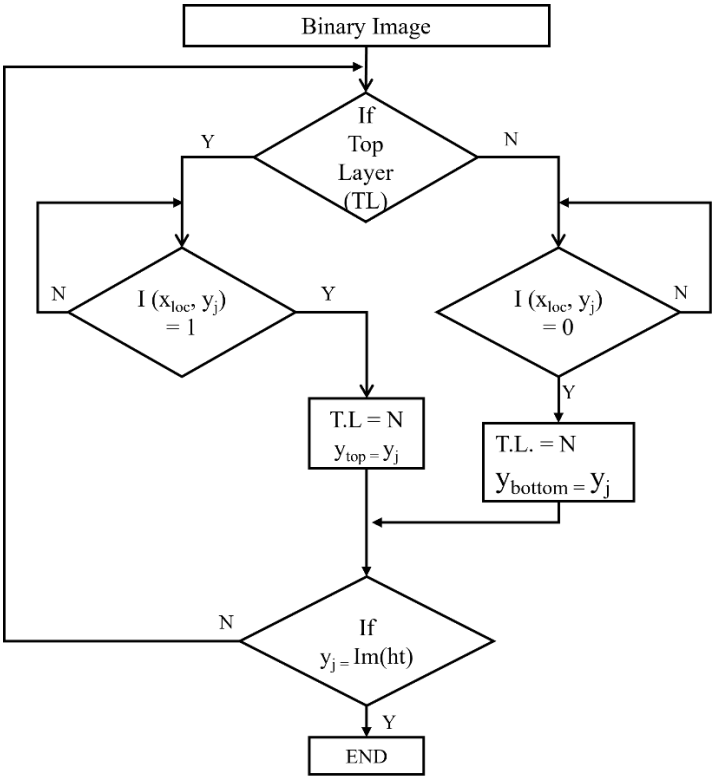


Figure 4.11: Flowchart of tracing all the fixed points

In the flowchart in Figure 4.11, y_j is the traced fixed points at the top and bottom edges of the beam of the structure, where j = {1, 2, 3 ……...55}. A total of 55 points are traced in the image to determine the deformation in the y direction. The bottom 5 points of the sample sitting on the surface are not considered here as they remain fixed on the surface without any deformation in the y direction. Similarly, 60 points are tracked on the vertical beams for deformation in the x direction.

4.3.1.2 Deformation Calculation

After all the points have been traced, the difference in location from the first image to the current image is calculated for all the points in the image. The difference is then multiplied with the calibration factor to know the deformation in mm. The deformation measurement formula used here is:

$$dist(x, y) = \{(x_2 - x_1) + (y_2 - y_1)\} \times C.F \qquad (4.13)$$

Here, x_1, y_1 = point location in the reference image, y_2 = point location in the current image, C.F= Calibration Factor.

The Calibration Factor (C.F) is determined by dividing the actual length of the object by the pixel length of the object.

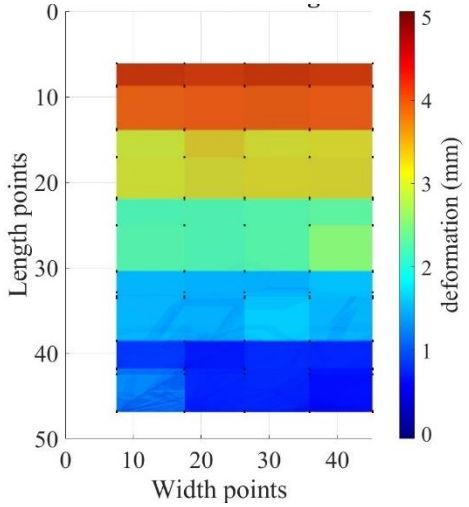
$$C.F = \frac{Actual\ Length\ of\ the\ Object}{Pixel\ Length\ of\ the\ Object} \qquad (4.14)$$

All the values found above are arranged in a x,y,z matrix where x,y are the length and width points of the object and z is the deformation value at location (x,y). To compare the results with other approaches, quantitative contour plots are developed through a three-dimensional surface plotting function in MATLAB. The surface plotting function "surf" has a solid edge colour and solid face colour. The values of z determine the colour of the surface therefore it generates a colour intensity displacement plot like the one generated in DIC analysis. However, as this model only traces a few points on the object, the output is found as some solid blocks of colour instead of the real-time colour intensity map on the image of the object. The results of this model are represented in Figure 4.12 alongside DIC results for comparison. The model provides accurate results for the selected points it traces throughout the dataset. Although those point deformation values mostly align with the DIC analysis values of those points, the fixed points sometimes trace a few background noise and illumination.

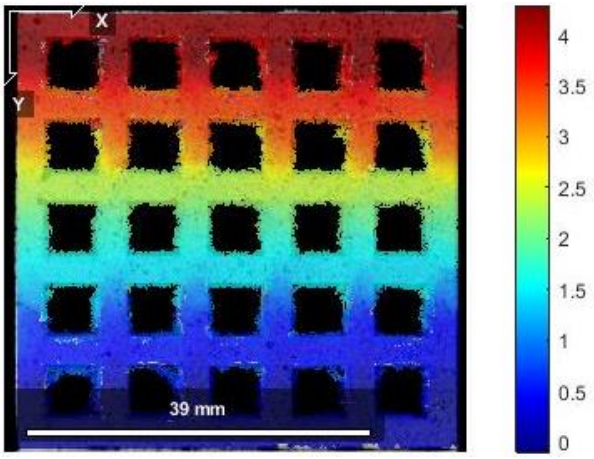
For example, the red block at the top right corner with a deformation of 0.4 mm in Figure 4.12(c) actually indicates the deformation of the hollow space between two vertical struts at the top right corner. From Figure 4.10, it can be seen that this red block at the top layer represents the gap between the 10th and 11th points from the left. Therefore, that result is not relevant for this analysis.

Furthermore, the material used here is Cubic Grid (TPU)-4 which did not exhibit symmetric deformation in the x direction after the application of large deformation in y axis resulting in local buckling. The condition of that material after compression is provided in Figure 5.5, where it can be seen that the middle portion of the sample deformed leftward while the top and bottom portion deformed to the right. This is also reflected in the DIC analysis result in Figure 4.12(d), where the U_x of the top left portion is 0 to -0.2mm. Similarly, the U_x of the top left

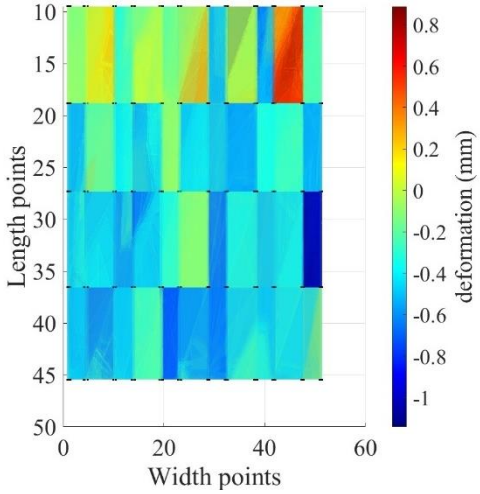
portion is 0 to -0.2mm in the fixed-points model. The U_x values on the right side also match the DIC analysis results.



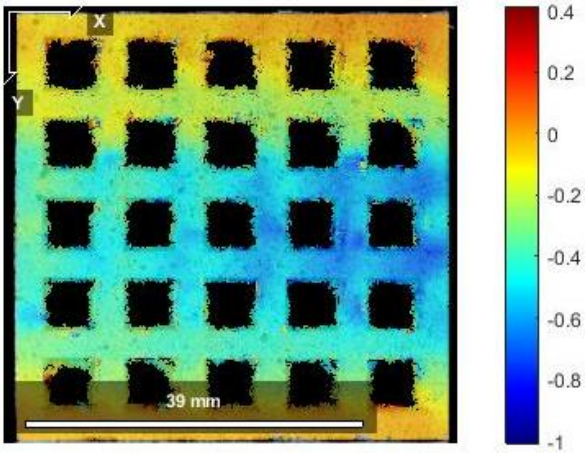
(a) U_y -Fixed Point Imaging Technique



(b) U_y - DIC Analysis Technique in Ncorr



(c) U_x - Fixed Point Imaging Technique



(d) U_x - DIC Analysis Technique in Ncorr

Figure 4.12: Results of deformation analysis through Fixed Point Imaging Technique

However, the results only portray deformation of the fixed points instead of full-field deformation similar to DIC. Hence, a second algorithm is developed to trace all the points of the object in the images which is described in Section 4.3.2.

4.3.2 All-Points-Based Deformation Analysis

In this technique, the locations of the pixel value 1 in the binary image are found and then the change in location from the reference image is calculated. This calculated change in location from the reference image represents the deformation of that object. A model is developed in

MATLAB to determine the deformation of the object through imaging techniques. This model can be explained in the workflow in Figure 4.13.

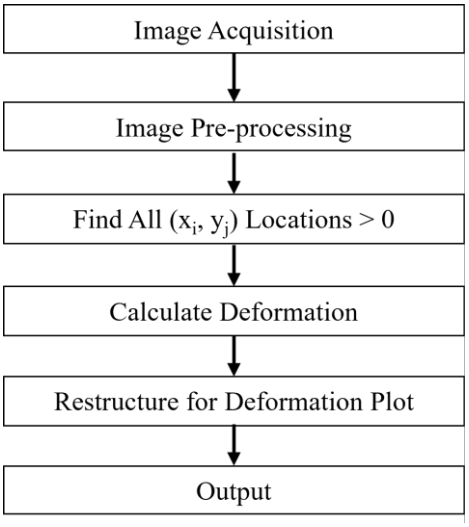


Figure 4.13: Workflow of deformation analysis through Tracing All Points

The image acquisition and image pre-processing steps are already explained in Section 3.7. The Image pre-processing for this model includes ROI detection, image segmentation/ background removal, RGB to greyscale conversion and image binarization.

4.3.2.1 Find All Locations

As explained in the previous section 4.3.1, in the binary images, the pixel values are only 0 and 1. The pixel locations in the images with pixel value 0 do not contain any object in that location and the locations with pixel value 1 contain the object. Therefore, the object is traced in each image by extracting the (x,y) locations with pixel value 1 from the binary image. The locations of the object in the image are traced, and then these locations are tracked through all the images to determine the change in location. The points with pixel value 1 are found using the following equation.

$$[x_{locs}, y_{locs}] = x_{locs}, y_{locs} \in I_{x,y} = 1 \qquad (4.15)$$

Here, x_{locs}, y_{locs} are the extracted locations with the object and $I_{x,y}$ are the locations of all pixels in the binary image. The first image is considered as the reference image, as there is no deformation.

4.3.2.2 Deformation Calculation

After tracing all the points in each image, the distance of each pixel location between the reference image and the current image is calculated. The deformation measurement equation used for this step is the Cosine Correlation Base Distance Measurement formula which can be seen below.

$$d(x,y) = \left\{ \frac{\sum(x_i \times y_j)}{\sqrt{\sum(x_i)^2 \sum(y_j)^2}} \right\} \times C.F \qquad (4.16)$$

The calculated distances are obtained in pixel values. These are converted to metric values by multiplying them with a calibration factor. The Calibration factor (C.F) is determined by dividing the actual width of the object in mm over the width of the object in pixels.

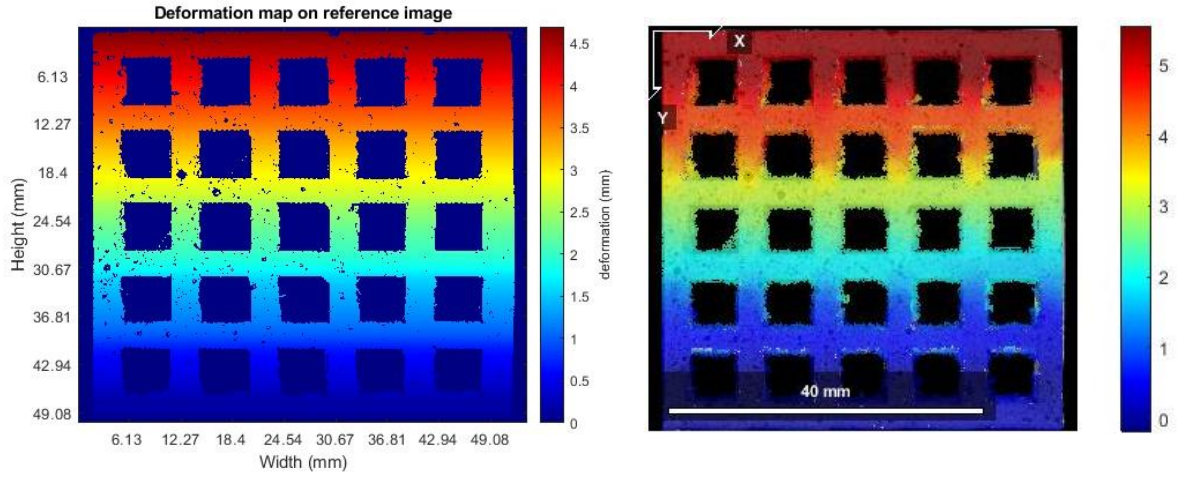
$$C.F = \frac{Actual\ Width\ of\ the\ Object\ in\ mm}{Width\ of\ the\ Object\ in\ pixels} \qquad (4.17)$$

After calculating the deformation, the values are arranged in a matrix where the columns and rows denote the x and y locations of the image. The deformation value for each location is put in their respective locations in the matrix. This deformation matrix is illustrated in a schematic diagram in Figure 4.14, where (x,y) are the coordinates in the image and (D_1, D_2, D_3.....) are the deformation values in those coordinates. D denotes the deformation value at particular (x,y) pixel location. The locations with 0 values denote locations without object.

x / y	1	2	3	4	5	6	7
1	0	0	0	0	0	0	0
2	0	0	0	D_1	D_2	D_3	0
3	0	D_4	D_5	0	0	D_6	0
4	0	D_7	D_8	0	0	D_9	D_{10}
5	0	D_{11}	D_{12}	0	0	D_{13}	0
6	0	D_{14}	D_{15}	D_{16}	D_{17}	D_{18}	0
7	0	0	0	0	0	0	0

Figure 4.14: Deformation matrix reconstruction

After the reconstruction, the results are plotted in a displacement diagram similar to the DIC analysis. The deformation values are illustrated in a colourmap where the colour intensity represent the deformation in that location. The displacement plots of this model and DIC analysis are provided in Figure 4.15.

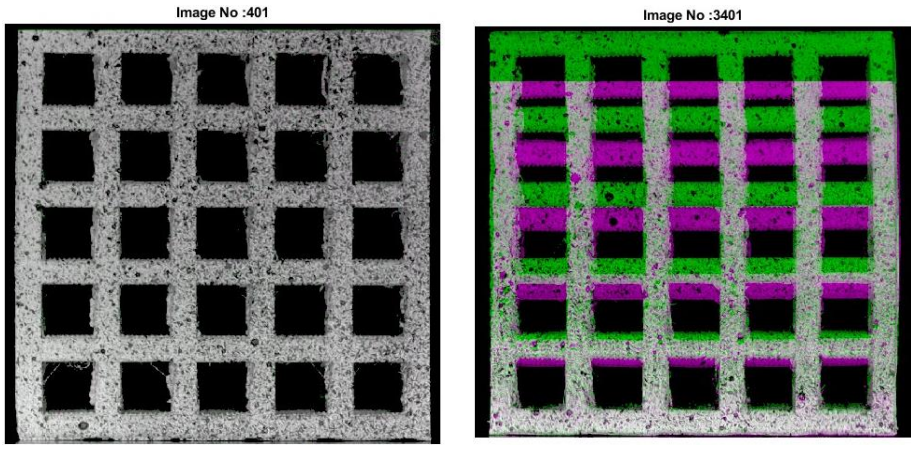


(a) Deformation Analysis with Imaging Technique (Tracing All Points)

(b) Deformation Analysis with DIC (Ncorr with Segmentation)

Figure 4.15: Deformation analysis through Imaging Technique (Tracing All Points)

As this model traces all the points with the object in the image, the displacement plots are closer to the displacement plots in DIC Analysis. This model also represents the real-time deformation of the object as shown in Figure 4.16. The green portion in Figure 4.16 represents the initial position of the object before loading and the pink portion represents the final position of the object after loading.



(a) Before Deformation Analysis

(b) After Deformation Analysis

Figure 4.16: Deformation illustration in Imaging Technique Model

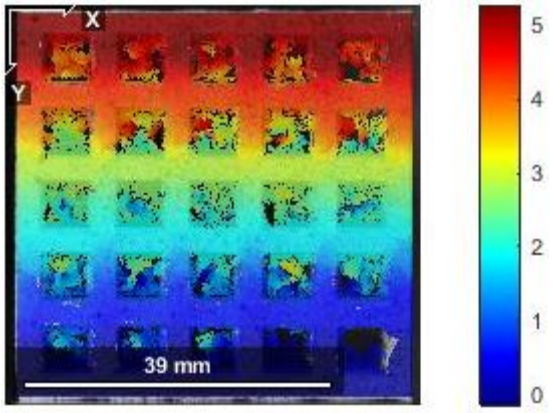
4.4 Conclusion

This chapter presented a comprehensive evaluation of various image analysis techniques for deformation measurement in lattice-structured materials. The investigation covered three primary approaches: DIC with Ncorr, DIC with Zeiss, and proposed Imaging Technique model for deformation measurement of AM lattice-structured materials through image analysis.

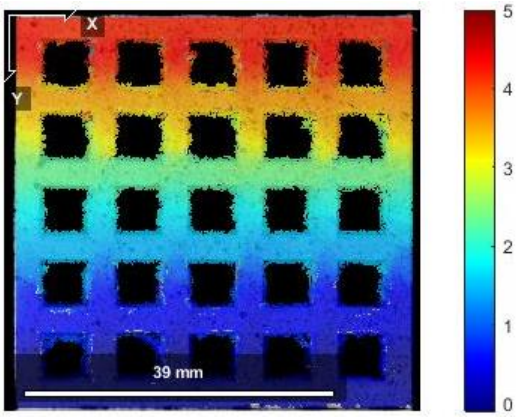
The implementation of DIC using standard Ncorr provides effective visualisation of deformation patterns. However, the background information visible through the strut gaps creates an error in deformation calculation. This limitation is addressed through the integration of background segmentation, resulting in more precise strut-specific measurements. Zeiss Inspect Correlate demonstrates excellent performance with standardised speckle patterns, featuring effective built-in background subtraction. However, it shows limitations in analysing specimens with poor quality or no speckle patterns.

Two distinct Imaging Technique models, (a) fixed-point-based deformation analysis and (b) all-points-based deformation analysis, are developed for this research. The first model encompasses the deformation of 55 points for U_y and 60 points for U_x all over the structure. The deformation plots do not represent full-field deformation like DIC. However, the point deformation results are almost identical to the DIC results. The second model incorporates segmentation and binarization in the pre-processing stage. Tracking all points with a pixel value of 1 across the images of the sample under loading conditions provides full-field deformation information. It also generates deformation contour plots comparable to established DIC techniques.

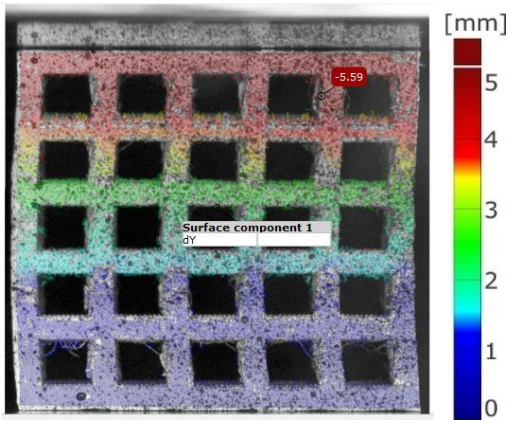
Visual representations of all techniques demonstrate consistent deformation patterns which suggest effective measuring capabilities across different approaches. Each approach has its unique advantages and limitations. The results of deformation in the Y direction for the Cubic Grid structure are compiled in Figure 4.17 for an overview. Details of the comparison on results will be discussed in the next chapter.



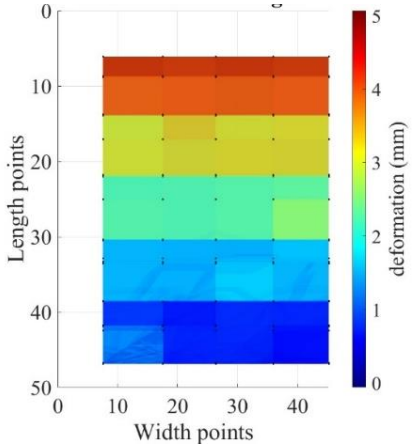
(a) DIC in NCorr without Segmentation



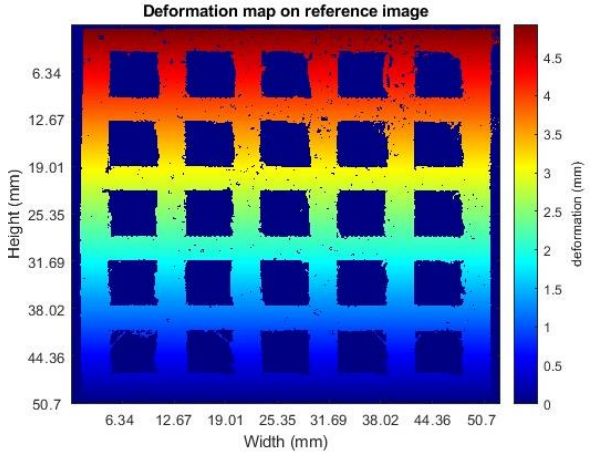
(b) DIC in Ncorr with Segmentation



(c) DIC in Zeiss



(d) Deformation analysis by Fixed Points



(e) Deformation Analysis by Tracing All Points

Figure 4.17: Comparison of U_y of Cubic sample through image analysis techniques

Chapter 5: Validation and Result Comparison

In this chapter, validation of the image analysis techniques through comparison with Finite Element Analysis (FEA) is discussed. The result comparison and summary of the whole research are covered as well. Furthermore, this chapter also discusses the effect of deformation direction, effect of speckle pattern, out of plane struts, camera, background and illumination on results. In the end, there is an analysis on the performance of the DIC software and Imaging Technique models used in this study.

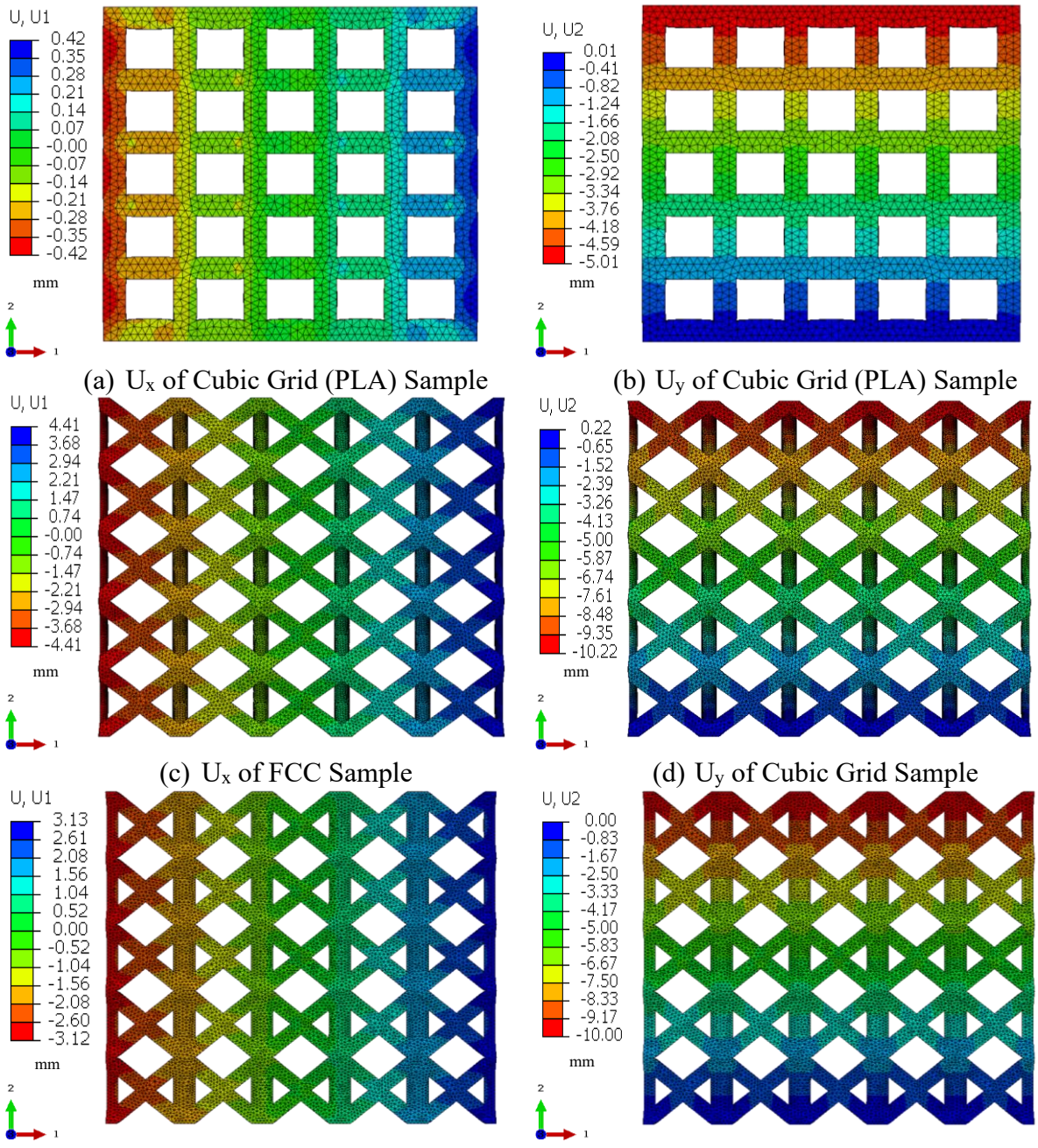
5.1 FEA of Lattice Structures

The Cubic Grid, FCC and FCCZ lattice-structured material models are evaluated through FEA based on actual compression test conditions. Section 3.8 outlines the parameters used for the FEA of this research. The deformation map generated from the analysis for deformation in X direction (U_x) and deformation in Y direction (U_y) are summarised in Figure 5.1. The actual deformation values derived from the compression test machine's output are simulated in this analysis. Although the testing machine only records the deformation result in Y direction (U_y) in this research, the simulation predicts the deformation in X direction (U_x) from the property of the material and the boundary conditions. The finite element gives the following values of deformation shown in Table 5.1, which are later compared to the DIC and Imaging Technique model outcomes to validate the result.

Table 5.1: Results of deformation in X and Y from Finite Element Analysis

Sample Name	Max U_x	U_x at the midpoint of vertical edges	Average U_x at edge	Max U_y	U_y at the midpoint of top edge	Average U_y at edge
Cubic-TPU	±0.49	±0.47	±0.42	-5.00	-5.00	-5.00
Cubic-PLA	±0.34	±0.28	±0.27	-4.01	-4.00	-4.00
FCC	±4.41	±3.99	±4.21	-10.22	-10.00	-10.00
FCCZ	±3.12	±2.71	±2.84	-10.00	-10.00	-10.00

Here, the positive (+) sign and the negative (-) sign in X direction denote the deformation towards the right and the left side respectively from the viewing perspective. Additionally, the negative (-) sign in Y direction denotes compression or downward deformation in Y direction.



(a) U_x of Cubic Grid (PLA) Sample (b) U_y of Cubic Grid (PLA) Sample

(c) U_x of FCC Sample (d) U_y of Cubic Grid Sample

(e) U_x of FCCZ Sample (f) U_y of FCCZ Sample

Figure 5.1: Deformation map of samples from FEA

5.2 Result Summary

In this section the results of the deformation analysis on additive manufactured lattice-structured materials are demonstrated. The results obtained from the (i) DIC Analysis, (ii) Imaging Technique and (iii) FEA are compared to the results from the testing machine data and the results are corroborated using different parameters.

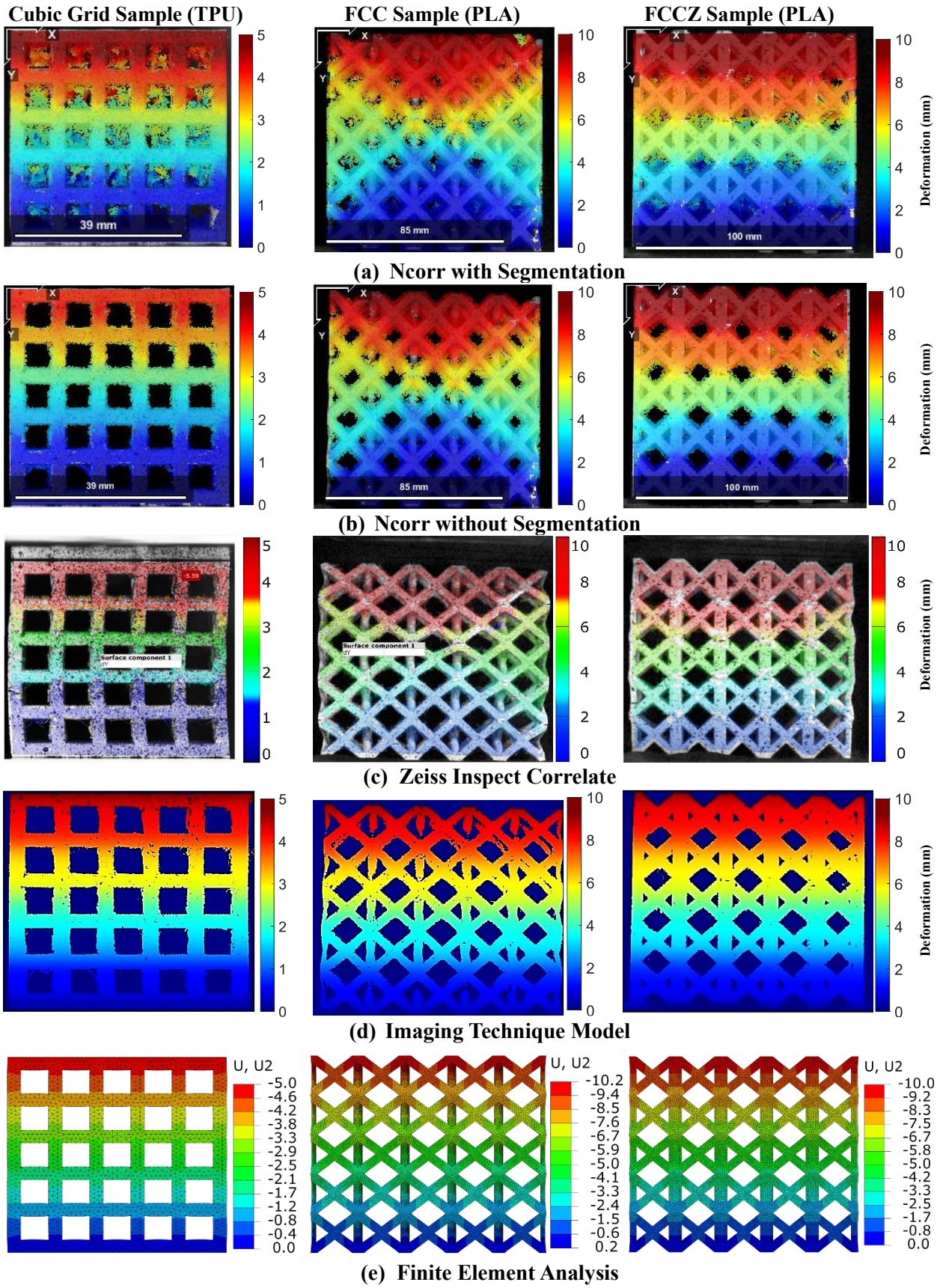


Figure 5.2: Deformation in Y direction for all materials

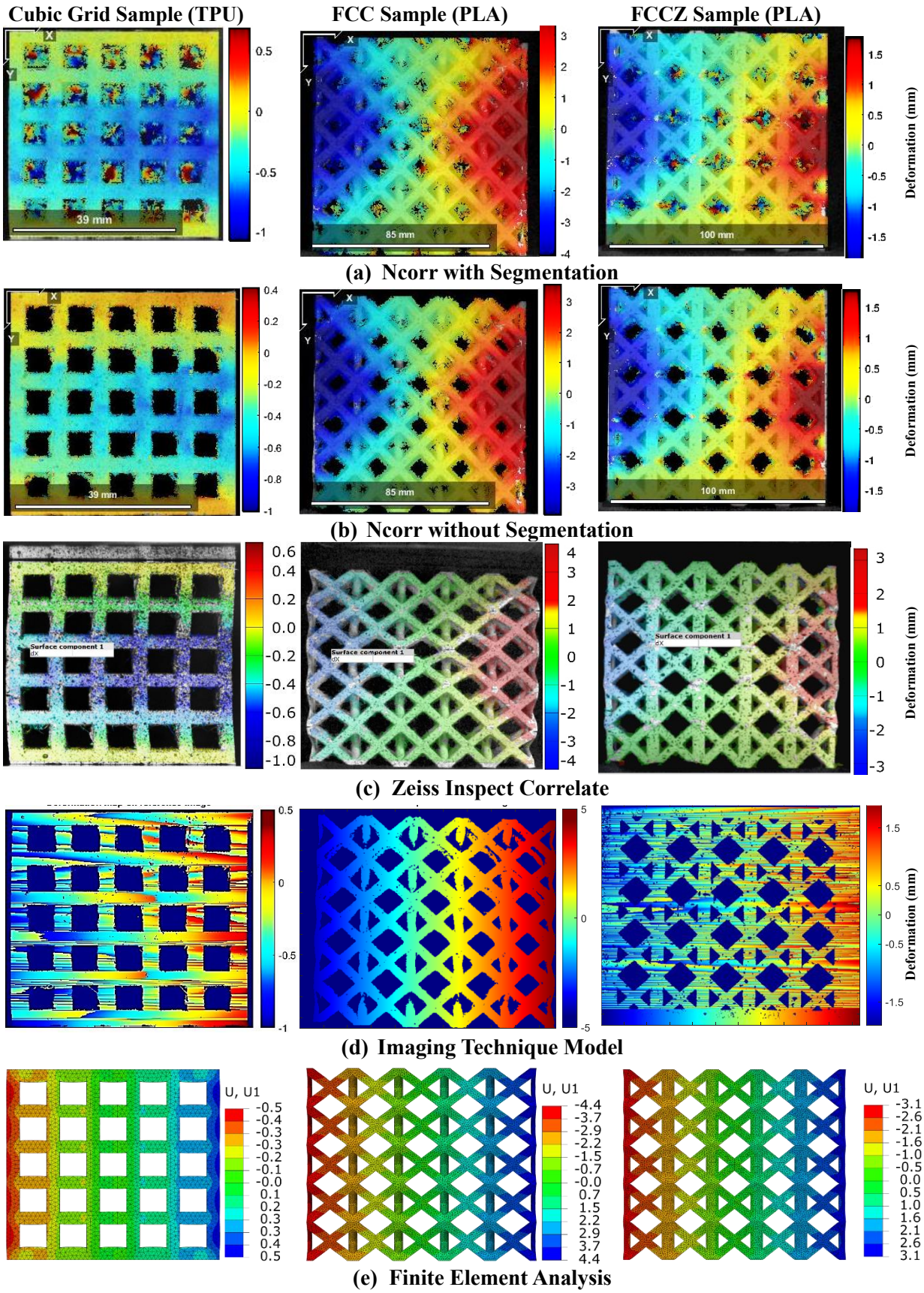
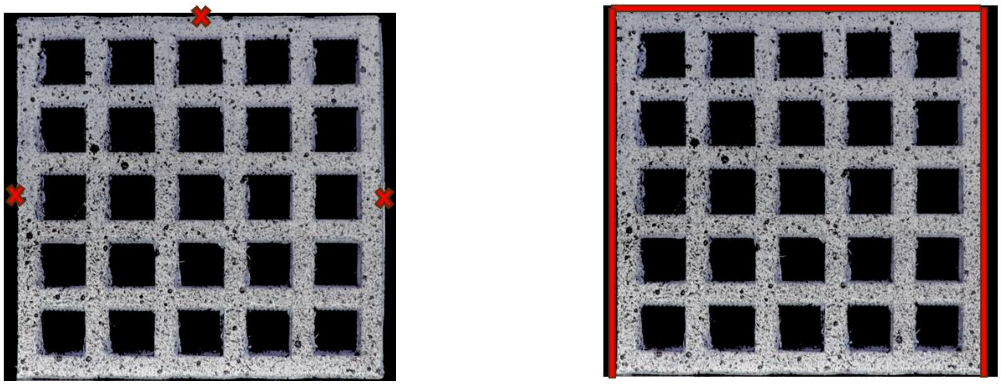


Figure 5.3: Deformation in X direction for all materials

The tracing-all-points Imaging Technique Model provides full-field deformation results and is compatible with the outcomes of DIC analysis and FEA. Therefore, this model will be used in this chapter to compare the parameters. The deformation plots in Y and X direction for all the materials used in this research are demonstrated in Figure 5.2 and Figure 5.3. The parameters for result analysis are: (i) value of deformation at midpoints of the edges, (ii) average deformation on the edges, (iii) Poisson's Ratio. The points and area determined to measure the deformation on the samples are shown in Figure 5.4.



(a) Selected points at the middle (b)Selected area over the edge

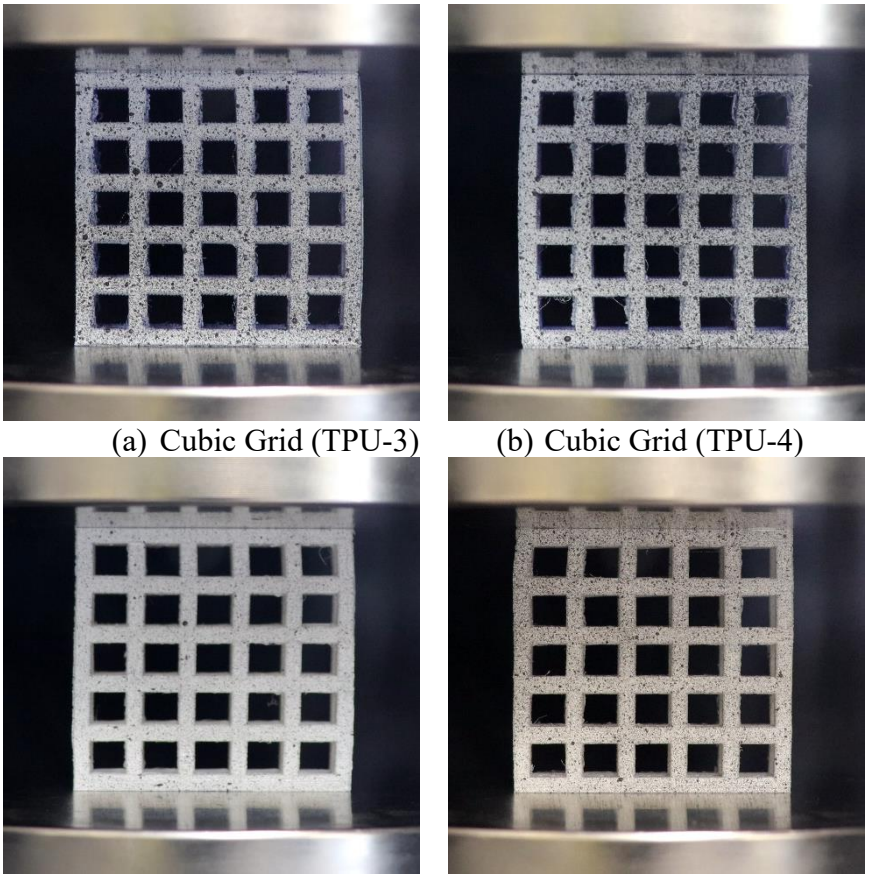
Figure 5.4: Selected (a) points and (b) area for deformation calculations

5.2.1 Effects of Deformation Direction on Results

This section discusses the variation in deformation behaviour along the X-axis observed in different samples of the same material. As discussed above, the experiments are performed under uniaxial compression loads in y direction through flat and smooth grippers. The similar condition is implemented in the FEM simulations as well. However, in some cases such as Figure 5.3 some discrepancy between FEM results and experimental DIC results on reading the deformation in x direction have been observed. This is particularly due to small defects in experimental specimens in comparison to ideal samples in FEM. For example, TPU Cubic Grid sample in Figure 5.3 tends to present a buckling mode rather than symmetrical uniaxial deformation due to micro defects or discrepancy in size of all the struts. It is acknowledged that this might affect some of the validations, however the image analysis method used is validated through several other experimental cases which is described in this chapter. Furthermore, it is recommended to prepare samples with AM methods with higher accuracy

such as Resin SLA or DLP in future works rather than FDM to minimise the existence of manufacturing discrepancies and errors.

It is observed from the analysis that the mean deformation values of vertical edges (U_x) of Cubic (TPU3) and Cubic (PLA3) do not match the mean U_x values of Cubic (TPU4) and Cubic (PLA4) respectively. Even though the mean deformation along the Y axis at the top surface (U_y) is effective in portraying the real longitudinal deformation at the top surface of the sample, the similar calculations along the X axis from the image analysis do not portray the real lateral deformation often.



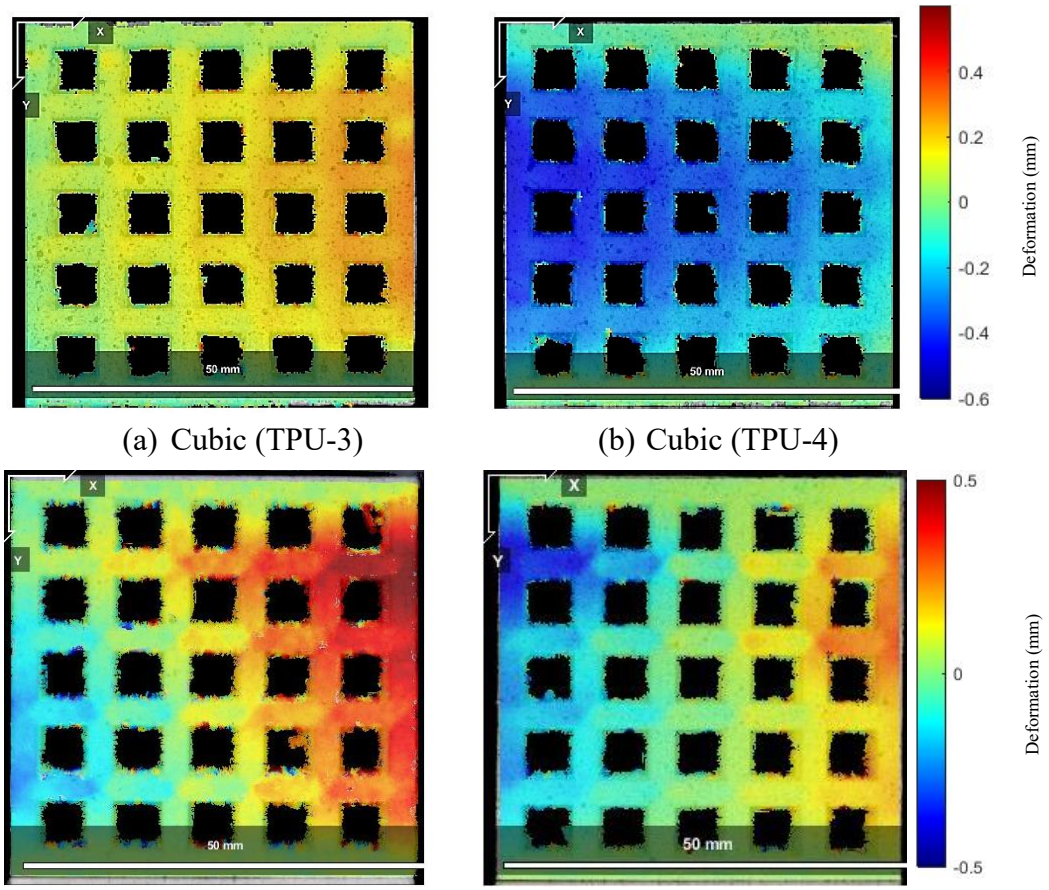
(a) Cubic Grid (TPU-3) (b) Cubic Grid (TPU-4)

(c) Cubic Grid (PLA-3) (d) Cubic Grid (PLA-4)

Figure 5.5: Deformed images of Cubic Grid samples

This error becomes evident, when the mean U_x values of Cubic (TPU3) and Cubic (TPU4) are compared to represent the common deformation behaviour of Cubic (TPU) materials. The difference in deformation direction and pattern along the Y axis for Cubic materials can be understood from the DIC analysis results in Figure 5.6.

For Cubic (PLA) samples, the PLA4 sample had a distinctive deformation pattern than PLA3. The strut joint at the left outer corner of PLA4 had a significant deformation during failure. Therefore, the U_x value around that location in Cubic (PLA4) is around 0.5 mm higher than the U_x value at the same location in Cubic (PLA3). This implies the unique deformation behaviour and the challenge of measuring the unguided deformation from image analysis.



(a) Cubic (TPU-3) (b) Cubic (TPU-4)

(c) Cubic (PLA-3) (d) Cubic (PLA-4)

Figure 5.6: DIC Analysis results of U_x for Cubic Grid samples

This also needs to be noted that all the deformation results for this research are extracted at the failure condition. Further study on compression test of lattice structures is recommended to understand the deformation behaviour.

5.2.2 Value of Deformation at Midpoints of the Edge

This section discusses the deformation results in the Y direction (Uy) at the midpoint of the top surface, and in the X direction (U_x) at the midpoints of the left and right vertical edges. The selected midpoints for the results in this section are shown in Figure 5.4(a).

5.2.2.1 Point Deformation in Y Direction

The deformation results in Y direction (U_y) at the midpoint of the top surface obtained from all approaches are compiled in Table 5.2. The results shown in this table are an average of two samples of their representative materials. Although a minimum three samples are preferred in these types of experiments to ensure repeatability, the low standard deviation observed in the two samples suggests that the deformation pattern is consistent. The standard deviation of all the samples of these four materials: Cubic (TPU), Cubic (PLA), FCC and FCCZ are provided in the table as well. The analysis techniques used in this research for deformation measurement are represented as Ncorr (DIC in Ncorr without Segmentation), Ncorr-Seg (DIC in Ncorr with Segmentation), Zeiss (DIC in Zeiss Inspect Correlate), I.T Model (deformation analysis in Imaging Technique Model by tracing-all-points) and FEA. The compression testing machine data added in Table 5.2 shows comparison with the rest of the approaches.

Table 5.2: U_y at the midpoint of the top surface of the samples

Approach	Deformation in mm				Standard Deviation (mm)			
	Cubic (TPU)	Cubic (PLA)	FCC (PLA)	FCCZ (PLA)	Cubic (TPU)	Cubic (PLA)	FCC (PLA)	FCCZ (PLA)
Ncorr	5.253	3.859	9.040	8.995	0.063	0.032	0.460	0.195
Ncorr-Seg	4.781	4.074	9.117	9.315	0.591	0.246	0.373	0.095
Zeiss	5.260	4.060	9.500	9.295	0.080	0.220	0.140	0.055
I.T Model	4.681	4.205	9.693	9.653	0.051	0.005	0.092	0.137
FEA	5.000	4.000	10.000	10.000	0.000	0.000	0.000	0.000
Test Data	5.000	4.090	10.000	10.000	0.000	0.061	0.000	0.000

The bar chart based on the results in Table 5.2 are illustrated in Figure 5.7. Only the samples with successful DIC analysis in all approaches are compared in this section. To understand the accuracy of the models, the results of the DIC analysis and Imaging Technique analysis are compared to the testing machine data and FEA results only when the material is deforming in the elastic region. This is worth mentioning that, only the elastic deformation mode is implemented in the FEM simulations and therefore the deformations beyond the elastic region observed in the experimental tests are not considered for the validation purpose with FEM. From the comparison, it can be observed that results from all the approaches are consistent with the testing machine data with 0-10% deviation rate. Among the DIC analysis software

approaches, the performances of Ncorr with segmentation and Zeiss Inspect Correlate's are noteworthy. The DIC works particularly well for Cubic PLA material with 0% error in Ncorr-seg and 1% error in Zeiss. Among all the approaches, Zeiss Inspect Correlate and Imaging Technique (I.T) model have results closest to the results obtained from tensile machine and FEA. I.T model's results are at a lower range of 3-6% compared to Zeiss with 1-7% deviation rate. The deviation percentage in results of DIC analysis and analysis through I.T Model are provided in the Table 5.3.

Table 5.3: Deviation Percentage of U_y (Top Middle) Compared to Testing Machine

Approach / Sample	Ncorr without Segmentation	Ncorr with Segmentation	Zeiss Inspect Correlate	I.T Model
Cubic (TPU)	5%	4%	5%	6%
Cubic (PLA)	6%	0%	1%	3%
FCC (PLA)	10%	9%	5%	3%
FCCZ (PLA)	10%	7%	7%	3%
Average	8%	5%	4%	4%

Furthermore, the sample type affects performance of each approach. Lattice structures have different buckling and deformation patterns because of their distinct geometry. For this reason, the approaches do not all follow the same trendline for every material. Due to complex geometry of FCC and FCCZ, the deviation percentages are higher (3-10%) for all the approaches in general compared to simple Cubic samples (0-6%). As this is a 2D image analysis, the out of plane deformation is not considered here.

Figure 5.7 depicts the deformation of different samples in Y direction (U_y) analysed through DIC, I.T model and FEA. Each bar shows the average U_y value at the top midpoint for different sample types using each approach. Additionally, the error bar represents the standard deviation of deformation results, indicating the range of actual values for the same material. The bigger error bar represents broader deformation pattern within the same material type. The average of different samples of the same materials are considered here to avoid repetition and simplify the data representation.

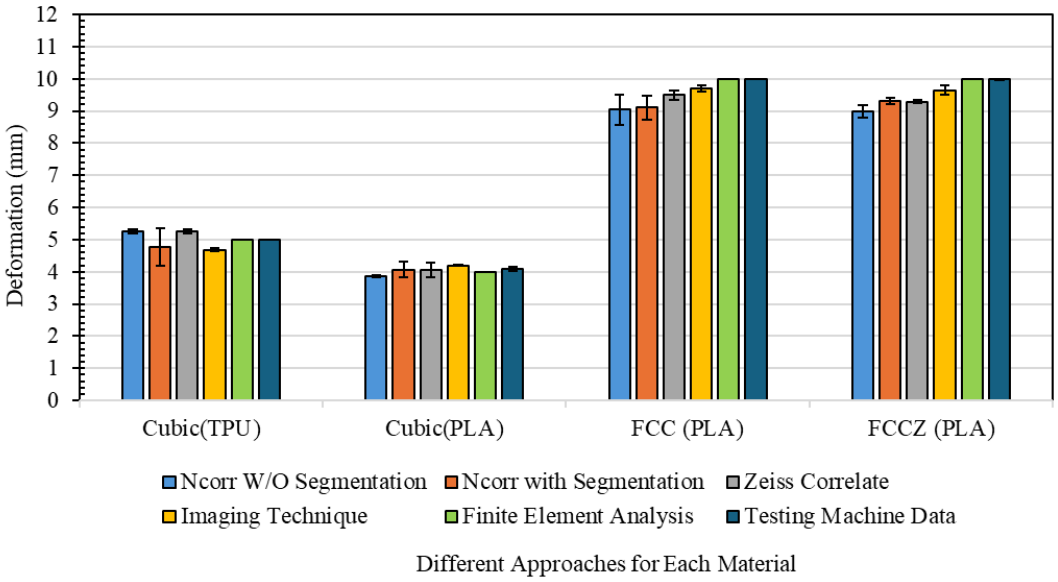


Figure 5.7: Deformation in Y direction at the middle point of the top edge of samples

Ncorr performs adequately with Cubic Grid structures. Ncorr with segmentation is more effective in calculating deformation at the top edge in average compared to Ncorr alone. But for Cubic Grid TPU materials, the deformation range varies significantly around 1.181 mm for samples within the same material group in Ncorr with segmentation, which is represented in the error bar in Figure 5.7. However, the other approaches do not detect the deformation variation range of Cubic TPU samples so broad.

For Cubic grid PLA material, the results from the I.T model are more consistent in terms of individual results and averaged results. Conversely, the error bars in Cubic PLA show that the individual results from Zeiss Correlate and Ncorr with segmentation have a broader range of deformation deviating 0.492 mm to 0.44mm from each other.

On the other hand, the deviation level in results of DIC analysis in Ncorr from the testing machine and FEA for FCC and FCCZ samples are significantly higher for Ncorr with segmentation than other approaches. As can be seen from the corresponding error bars, both Ncorr techniques' individual point deformation values vary widely for FCC samples (0.75-0.92mm). In general, both Zeiss Correlate and I.T model performed well individually on each FCC samples. For FCCZ samples, I.T model worked better than all the other approaches. The result levels are found to be consistent with each other in Ncorr and Zeiss.

It needs to be noted that the geometry of FCC and FCCZ cause the point deformation in those samples to be unpredictable. The results obtained from the testing machine is suitable for the deformation on the top surface. It does not necessarily reflect the point deformation on that top surface. The point deformation is unique to each sample and lattice geometry.

5.2.2.2 Point Deformation in X direction

The value of deformation at the midpoints of vertical and horizontal edges (as shown in Figure 5.4(a)) are obtained from the DIC Analysis, I.T model and FEA. The point deformation of each material on the midpoints of the vertical edges are given in Table 5.4 and Table 5.5. Bar charts generated from Table 5.4 and Table 5.5 showing the point deformation in X direction at the left and right edges of the materials are given in Figure 5.8.

Table 5.4: U_x at the midpoints of left and right edge- Cubic samples

Approach	Deformation (mm) at left and right edges of sample							
	Cubic (TPU3)		Cubic (TPU4)		Cubic (PLA3)		Cubic (PLA4)	
	Left	Right	Left	Right	Left	Right	Left	Right
Ncorr	0.36	0.25	-0.40	-0.55	-0.06	0.20	-0.46	-0.20
Ncorr-Seg	0.37	0.25	-0.40	-0.43	-0.06	0.23	-0.49	-0.20
Zeiss	0.41	0.36	-0.36	-0.60	-0.37	0.13	-0.43	-0.20
I.T Model	-0.36	0.33	-0.45	0.30	-0.37	0.34	-0.42	0.46
FEA	-0.47	0.47	-0.47	0.47	-0.28	0.28	-0.28	0.28

Table 5.5: U_x at the midpoints of left and right edge- FCC and FCCZ samples

Approach	Deformation (mm) at left and right edges of sample							
	FCC3		FCC4		FCCZ3		FCCZ4	
	Left	Right	Left	Right	Left	Right	Left	Right
Ncorr	-3.70	3.46	-4.14	3.65	-1.96	1.67	-1.87	2.04
Ncorr-Seg	-3.94	3.50	-4.15	3.65	-1.89	1.67	-1.91	2.03
Zeiss	-3.69	3.71	-3.94	3.84	-1.67	2.12	-2.21	1.82
I.T Model	-3.99	4.1	-3.90	4.48	-2.72	2.98	-2.77	2.81
FEA	-3.99	3.99	-3.99	3.99	-2.71	2.71	-2.71	2.71

The overview of the U_x deformation plots is provided in Figure 5.3. The deformation in Y direction is controlled through the loading process and is free to deform in X direction. The deformation of each sample is also affected by the existence of any manufacturing inaccuracies or defects in the samples. The results substantiate the discussion presented here and in section 5.2.1. Due to experimental defect, the deformation in X direction has been rightwards for TPU3

and leftwards for TPU4. Therefore, the DIC results portray the experimental condition and are not aligned with the FEA results' direction. Even after that, the magnitude of the deformation through all DIC approaches are consistent among themselves. The DIC analysis results of the Cubic (PLA3) sample is not accurate due to poor speckle patterns, so some discrepancies in DIC results are observed. But the DIC analysis of the PLA4 sample shows consistent results with 0-0.03 mm standard deviation among the three approaches.

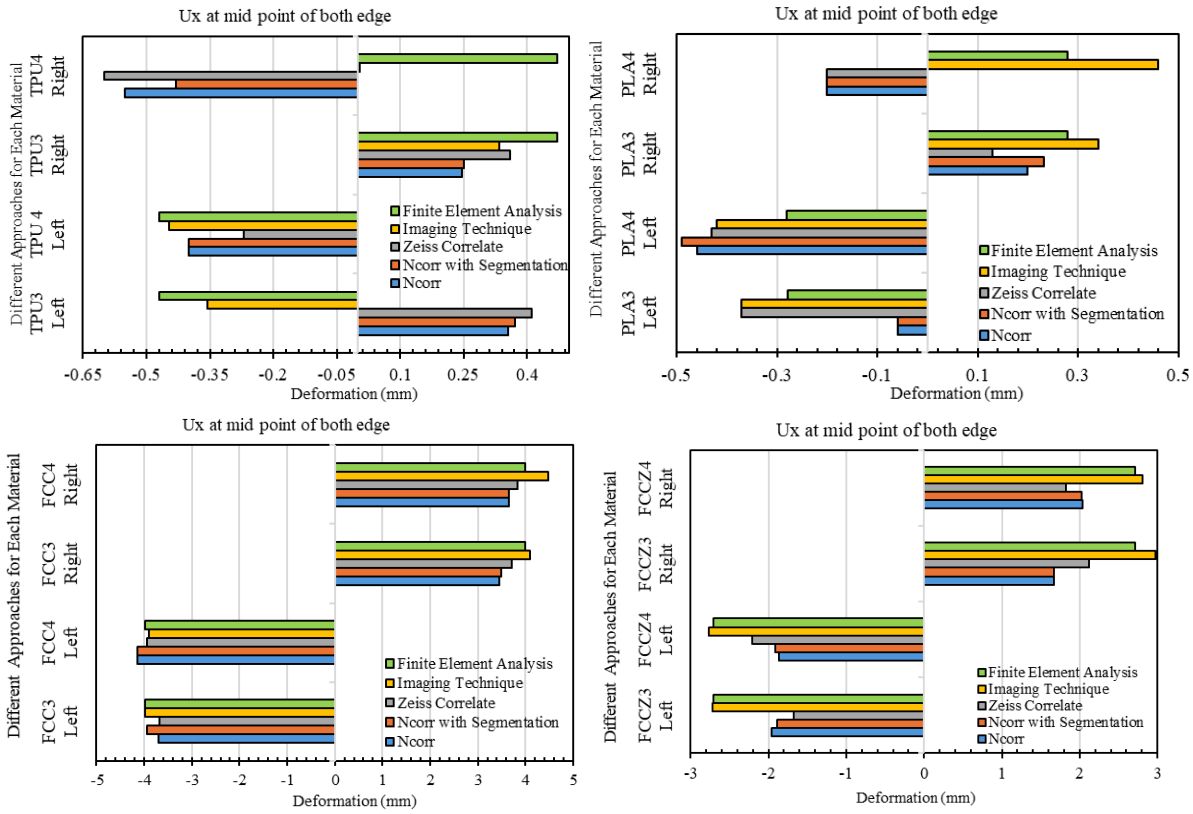


Figure 5.8: Point U_x at the midpoints of left and right vertical edges

For FCC and FCCZ samples, the deformation direction in experiment matches the FEA. Among DIC analysis approaches, Zeiss and Ncorr-seg work best with both having 1.3-38% deviation rate from FEA for these materials. For Ncorr the deviation rate is 3.8 to 38.4% which is closer to the other two techniques. I.T model has the least deviation of 0-10% from the FEA values.

From the above discussion it is evident that U_x determination for lattice structures through image analysis is challenging. Even though FEA is capable of portraying the experimental situation accurately, a few discrepancies with FEA and experimental results have been observed.

That is due to manufacturing and experimental defects causing the differing deformation pattern and local buckling. Moreover, the validation is only possible in elastic region unless the failure condition is considered in the simulation. Some of the samples were compressed until failure (Cubic PLA), which was not incorporated in the FEA simulation. Therefore, the inconsistency between experimental and FEA result occurred. Furthermore, the experimental U_y values of the samples were known from the tensile machine data, making the validation easier. Additional experiment with larger sample size and limiting the analysis for the elastic deformation are recommended for validation of U_x measurement through multiple image analysis techniques in further research. Except for this validation error of certain samples for U_x due to experimental defects, 2D DIC has been validated to measure the experimental results accurately for other samples in this research. This is to be noted as well that the midpoint U_x at the vertical edges do not portray the whole deformation of that material, it is included here for comparison purposes. The average U_x throughout the edge has a better portrayal of the deformation in X direction which is provided in section 5.2.3.2.

5.2.3 Average Deformation on the Edge

As mentioned in the previous subsection, not all points at the edge of the samples have the same deformation. Therefore, an average value of all the points on the outermost layers of the samples are calculated to compare the data. For the Y axis, the topmost horizontal edge is selected, and for the X axis, the left and right vertical edges are selected. The location of the selected edges is shown in Figure 5.4(b).

5.2.3.1 Average Deformation in Y direction

The average deformation in Y direction (U_y) on the top surface of the samples obtained from all the approaches are compiled in Table 5.6. The results shown in this table are an average of 2 samples (i.e. TPU3, TPU4) of their representative materials. The standard deviation of all the samples of these 4 materials: Cubic (TPU), Cubic (PLA), FCC and FCCZ are provided in the table as well. The bar chart based on Table 5.6 comparing the average deformation on the top surface of all the samples for each approach is illustrated in Figure 5.9.

Table 5.6: Average U_y at the top surface of the samples

Approach	Deformation in mm				Standard Deviation (mm)			
	Cubic (TPU)	Cubic (PLA)	FCC (PLA)	FCCZ (PLA)	Cubic (TPU)	Cubic (PLA)	FCC (PLA)	FCCZ (PLA)
Ncorr	5.201	3.837	9.14	9.01	0.039	0.033	0.290	0.050
Ncorr-Seg	4.784	4.096	9.120	9.225	0.600	0.292	0.290	0.015
Zeiss	5.270	4.040	9.190	9.305	0.090	0.190	0.090	0.055
I.T Model	4.680	4.209	9.735	9.620	0.050	0.002	0.075	0.260
FEA	5.000	4.000	10.000	10.000	0.000	0.000	0.000	0.000
Test Data	5.000	4.090	10.000	10.000	0.000	0.061	0.000	0.000

The average deformation U_y at the topmost layer of all samples are computed using the same dataset as in the previous subsection. To determine the accuracy of the models, the findings of the Imaging Technique and DIC analysis are compared with the data from the testing machine and the FEA results. The comparison shows that, the results of all approaches agree with the testing machine data with a variation rate of 0–10%. The error percentages are higher for complex geometry material like FCC and FCCZ. Zeiss Inspect Correlate and Ncorr with segmentation perform well among the DIC analysis software used in this research with 5% average deviation from the ground truth (testing machine data). Though, the results in Zeiss are steadier with 1-7% error compared to Ncorr with segmentation. Out of all the approaches, the Zeiss Inspect Correlate and I.T model generate results that are more aligned to those from FEA and tensile machines. Table 5.7 shows the percentage difference between the results of DIC analysis and analysis using the I.T Model:

Table 5.7: Deviation percentage of U_y (top surface average) compared to testing machine

Approach / Sample	Ncorr without Segmentation	Ncorr with Segmentation	Zeiss Inspect Correlate	I.T Model
Cubic (TPU)	4%	4%	5%	6%
Cubic (PLA)	6%	0%	1%	3%
FCC (PLA)	9%	9%	8%	3%
FCCZ (PLA)	10%	8%	7%	4%
Average	7%	5%	5%	4%

Figure 5.9 depicts the average deformation in the Y direction of various materials investigated with DIC, I.T Model and FEA. The average of the mean U_y values at the top surface for every kind of sample is presented by each bar. The average deformation is portrayed here to avoid repetition of the results of multiple samples of the same material. All the Cubic Grid (TPU)

samples' results are averaged and demonstrated as Cubic (TPU) in the charts and figures. Similarly, all the other materials are also compiled as Cubic (PLA), FCC and FCCZ in charts and figures. The actual deformation range derived from the samples of that specific material are shown by the error bar, which represents the standard deviation of multiple samples of the same material.

Every sample has its unique deformation pattern and value, therefore the outcomes of analysis through each approach are different for each sample. Ncorr performs adequately with Cubic Grid samples with 0.03mm standard deviation from the average of both samples. The deformation maps of Cubic samples generated from Ncorr are found to be consistent with the results from the other approaches as well. But for Cubic Grid TPU materials, the deformation range varies significantly around 1.2mm for samples within the same material group in Ncorr with segmentation. On the contrary, the results for this material obtained from other approaches are consistent with 0 to 0.09mm standard deviation within the samples.

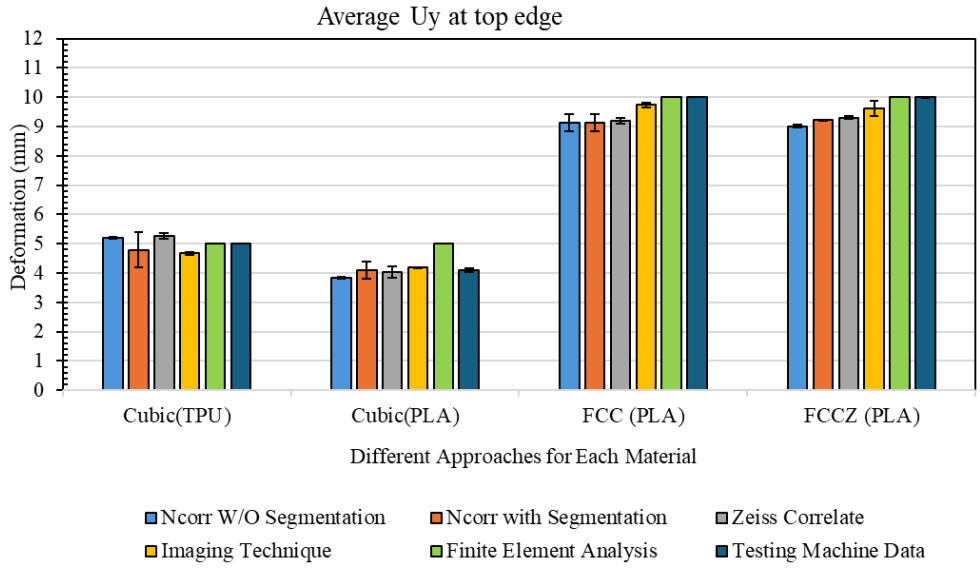


Figure 5.9: Average deformation (Y direction) of different samples at the top edge

The I.T model results are more consistent with the testing machine result and FEA for Cubic Grid PLA samples. For Ncorr with segmentation and Zeiss Correlate, the average results are quite aligned with the ground truth (testing machine data), but the individual results vary by 0.38-0.58mm.

In terms of results of FCC and FCCZ, Zeiss Correlate and I.T Model are more competent compared to the approaches in Ncorr. The deformation calculated from Ncorr differ 9-10% from the testing machine deformation value for these two types of samples. As observed from the error bar in Figure 5.9, the individual results for each FCC sample vary 0.58 mm from each other. The individual results for FCCZ are quite consistent with each other except the results of I.T Model. The deformation values of FCCZ samples fluctuate 0.52 mm from each other. Whereas the results derived from Zeiss and Ncorr appear to be consistent with one another.

5.2.3.2 Average Deformation in X direction

The average deformation in X direction (U_x) on the left and right vertical surface of the samples obtained from all the approaches are compiled in Table 5.8 and Table 5.9. The results shown in these tables are the average U_x at the left and right edges of all samples of their representative materials. The bar chart based on these tables comparing the average deformation on the top surface of all the samples for each approach are illustrated in Figure 5.10.

Table 5.8: Average U_x at the left and right edge- Cubic

Approach	Deformation (mm) at left and right edges of sample							
	Cubic (TPU3)		Cubic (TPU4)		Cubic (PLA3)		Cubic (PLA4)	
	Left	Right	Left	Right	Left	Right	Left	Right
Ncorr	0.22	0.15	-0.28	-0.36	-0.12	0.06	-0.50	-0.03
Ncorr-Seg	0.24	0.10	-0.25	-0.31	-0.12	0.29	-0.61	-0.03
Zeiss	0.36	0.22	-0.27	-0.36	-0.34	0.06	-0.42	-0.07
I.T Model	-0.36	0.26	-0.23	0.25	-0.23	0.30	-0.24	0.26
FEA	-0.42	0.42	-0.42	0.42	-0.27	0.27	-0.27	0.27

The results of DIC analysis with Ncorr and Ncorr-seg for TPU3 are consistent with each other but the Zeiss result deviates by 0.1mm. On the other hand, all the DIC results for TPU4 are well coordinated with each other. DIC analysis in Zeiss for PLA3 had partial value due to poor speckle patterns, therefore the results are not consistent with other DIC approach results. The Imaging Technique results are in better coordination with the FEA results with 15%-46% deviation for TPU materials and 4.4%-14.7% deviation for PLA. Even though the deformation direction is different, the magnitude of all the approaches is consistent to FEA.

Table 5.9: Average U_x at the left and right edge- FCC and FCCZ samples

Approach	Deformation (mm) at left and right edges of sample							
	FCC3 (PLA)		FCC4 (PLA)		FCCZ3 (PLA)		FCCZ4 (PLA)	
	Left	Right	Left	Right	Left	Right	Left	Right
Ncorr	-4.01	3.24	-4.05	3.5	-2.02	1.85	-2.04	2.10
Ncorr-Seg	-4.00	3.35	-4.05	3.53	-1.97	1.67	-1.72	1.65
Zeiss	-3.64	3.30	-3.39	3.22	-1.17	1.37	-1.54	0.96
I.T Model	-3.98	3.94	-3.86	4.44	-2.71	2.97	-2.72	2.80
FEA	-4.21	4.21	-4.21	4.21	-2.84	2.84	-2.84	2.84

The deformation directions for the practical experiment and the simulation are the same for FCC and FCCZ. The I.T Model works best in comparison to FEA with 0.5-5.6% deviation for all samples of FCC and FCCZ. Among the DIC techniques, Ncorr and Ncorr-Seg both give good results with 4.3-20% deviation from FEA results for FCC materials. Zeiss has 16.5-59% deviation rates from FEA results for FCC materials. Ncorr and Ncorr work better in FCCZ samples with 29-42% deviation in comparison to Zeiss having 52-59% deviation from FEA results. Among Ncorr and Ncorr-seg, Ncorr-seg performed better in FCC materials with 11% deviation while Ncorr had deviation of 12%. Whereas Ncorr performed better in FCCZ materials with 29% deviation compared to Ncorr-seg with 38% deviation.

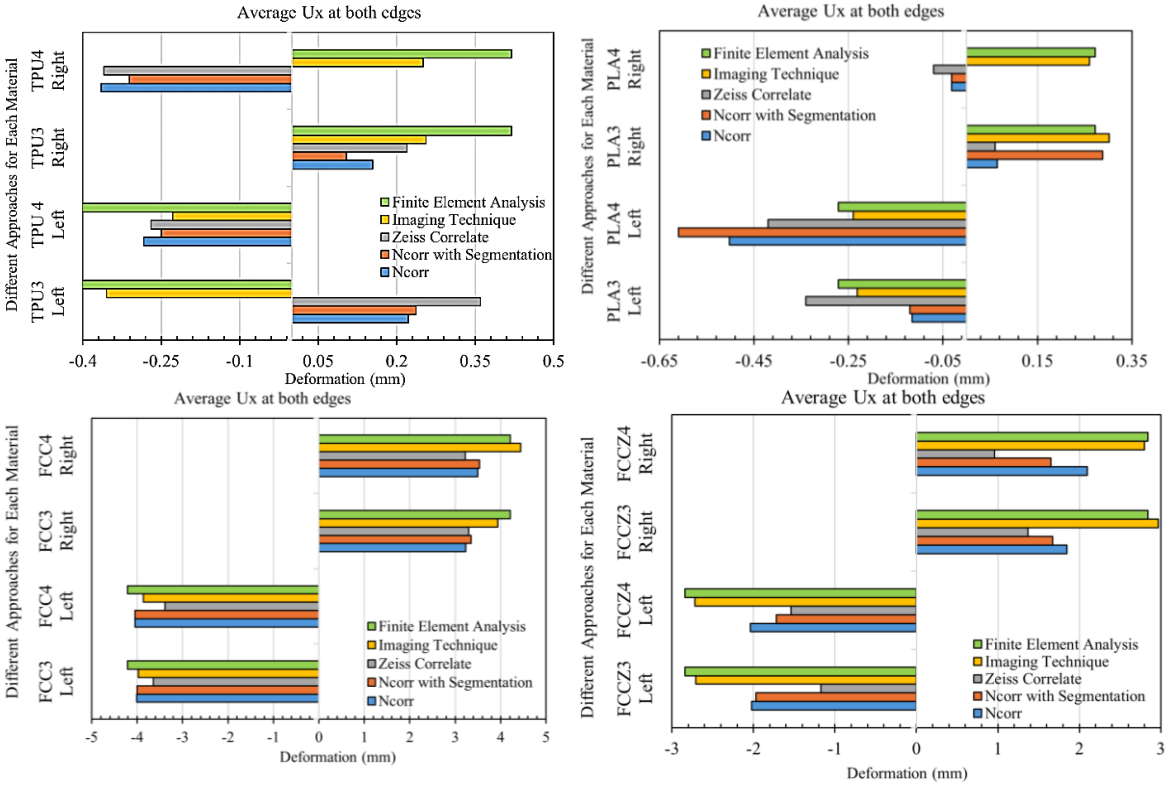


Figure 5.10: Average U_x at the left and right vertical edges

The average U_x analysis on the edges of the samples are more reliable than point deformation values to understand and compare the deformation behaviour of different materials.

5.2.4 Poisson's Ratio

For this section, the Poisson's ratio of each lattice-structured material has been calculated, and the results are discussed. The values of point and average deformation (U_x and $U_{y)}$ of the structures are used to determine the Poisson's ratio of the materials. The results are compared to validate the analysis techniques and to understand the deformation behaviour further.

The Poisson's ratio calculated here using the deformation values follows the equations below:

$$\nu = -\frac{\epsilon_x}{\epsilon_y} \qquad (5.1)$$

Here, ϵ_x = Transverse Strain (Strain in X direction), and ϵ_y = Axial Strain (Strain in Y direction). The transverse and axial strain values can be calculated from the following equation:

$$\epsilon_x = -\frac{U_x}{W} \qquad (5.2)$$

$$\epsilon_y = -\frac{U_y}{H} \qquad (5.3)$$

Here, U_x= Deformation in X direction at the selected location and U_y= Deformation in Y direction at the selected location. Moreover, W= Width of the sample and H= Height of the sample.

The transverse and axial strains for the Poisson's ratio are calculated in two methodologies- (i) from point deformation at the mid points of horizontal and vertical edges, (ii) from average deformation of the horizontal and vertical edges. The deformation measured from these locations are used in equation 5.2 and 5.3 to calculate transverse and axial strains at midpoint of the edges, average Transverse Strain at the vertical edges and average Axial Strain at the top surface. The transverse and axial strain values can be calculated from the equations like equation 5.2 and equation 5.3.

The Poisson's ratio calculated through equation 5.1 are listed in Table 5.10. Since the testing machine only produced deformation in the Y direction, its results are not considered here. For

Poisson's ratio in lattice structures, the average deformation on lateral and longitudinal surfaces are considered more accurate due to the geometry and deformation nature. However, due to the variation in deformation direction along X axis (as discussed in 5.2.1), the mean deformation value of the vertical edges differs significantly from each other.

Table 5.10: Poisson's ratio calculated from point deformation and mean deformation

Material	Ncorr without Segmentation		Ncorr with Segmentation		Zeiss Inspect Correlate		Imaging Technique		FEA	
	Point	Mean	Point	Mean	Point	Mean	Point	Mean	Point	Mean
Cubic TPU	0.12	0.12	0.12	0.13	0.16	0.13	0.13	0.11	0.17	0.17
Cubic PLA	0.11	0.12	0.14	0.12	0.13	0.12	0.15	0.14	0.14	0.14
FCC PLA	0.61	0.67	0.64	0.57	0.64	0.59	0.48	0.51	0.84	0.84
FCCZ PLA	0.39	0.47	0.36	0.49	0.42	0.35	0.69	0.55	0.54	0.57

It is noticeable from Table 5.10 that every DIC techniques and Imaging technique model results of Cubic (TPU) samples match with each other. the. While the results of the Zeiss Correlate and I.T Model (point deformation) are the most consistent with the value derived from the Finite Element Analysis with 10-26% deviation. The results derived from all the approaches deviate from the TPU and PLA materials' standard Poisson's ratio 0.45 and 0.35 respectively. The Poisson's ratio derived from the mean deformation in FEA is considered as ground truth in this research for validation. It is observed that the results of Cubic (PLA), FCC and FCCZ samples vary even though they are all made with PLA material. This is because the geometric structure of the material has great impact on properties beside Young's Modulus and Poisson's Ratio [125]. For Cubic (PLA) material, the results for all methods are well aligned with the result from FEA with the least deviation of 0-14%. The results from I.T model and Ncorr with segmentation's Poisson's ratio had 0% deviation from the FEA result for Cubic (PLA).

For FCC, Ncorr performed best with the least errors of 20%. On the other hand, the results of I.T Model are best competent with the FEA results for FCCZ materials with 4% deviation. The other DIC methods with Ncorr also provided good results with 16-28% deviation with FEA results. It needs to be noted here that the accurate determination of Poisson's Ratio for lattice structures is mostly challenging, especially for the structures with complex geometry like FCC and FCCZ. Cubic Grid structures have chance of less error due to its smooth surface on the edge. Nevertheless, due to the uncertain outcome of U_x for structure property, not all the samples of the same material provide similar results. Table 5.11 demonstrates the standard deviation of the results for all the samples and Figure 5.11 and Figure 5.12 illustrates the results

with these standard deviations for each material represented by the error bars. As the results of FEA do not deviate for all samples of same material, the standard deviation is not applicable for this approach. From these results it can be observed that the complex geometry structures like FCC and FCCZ have higher standard deviation within the same materials. Between these two materials, FCCZ samples provided more consistent results due to having Z struts along the left and right vertical surfaces. The deformation in X direction due to the solid struts have been more regulated and the deviations are lower for each material and each technique.

Table 5.11: Standard deviation of Poisson's Ratio (point and average) for all samples

Material	Ncorr without Segmentation		Ncorr with Segmentation		Zeiss Inspect Correlate		Imaging Technique	
	Point	Mean	Point	Mean	Point	Mean	Point	Mean
Cubic TPU	0.045	0.010	0.045	0.005	0.005	0.005	0.005	0.035
Cubic PLA	0.030	0.040	0.030	0.040	0.035	0.010	0.070	0.050
FCC PLA	0.110	0.080	0.020	0.020	0.005	0.060	0.325	0.285
FCCZ PLA	0.040	0.020	0.030	0.035	0.035	0.040	0.115	0.005

As for Cubic Grid structures, Figure 5.5 of deformed images of these structures show that they had different deformation patterns in X direction for each material. Therefore, the results vary highly within the samples of the same material. The outcomes of the above discussed calculations are portrayed in bar charts in Figure 5.11 and Figure 5.12.

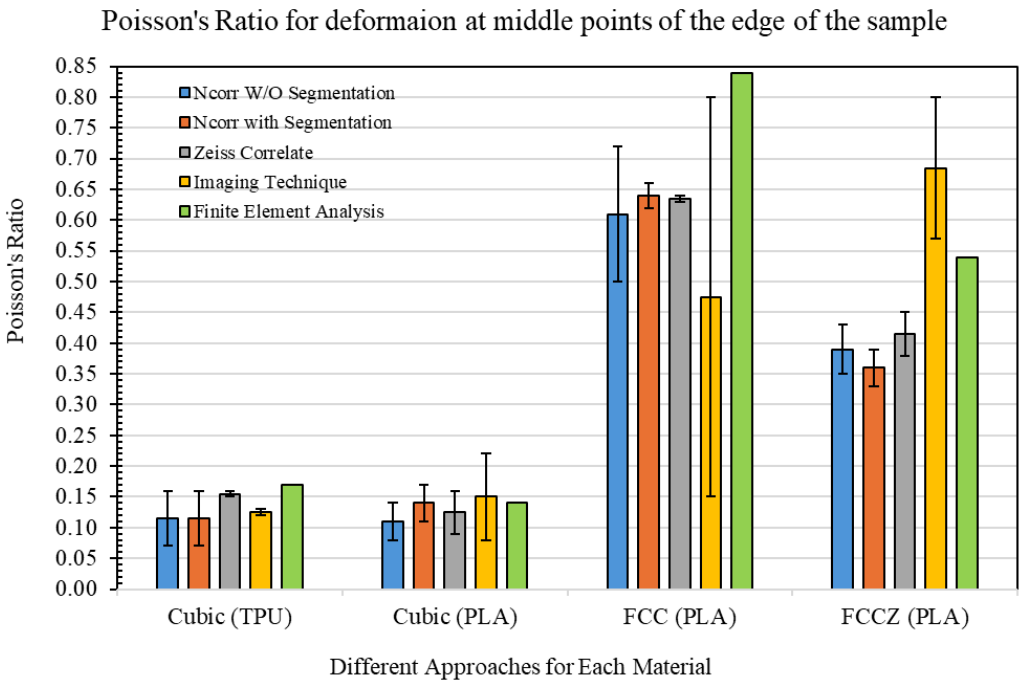


Figure 5.11: Poisson's ratio for deformation at the middle points of the sample edges

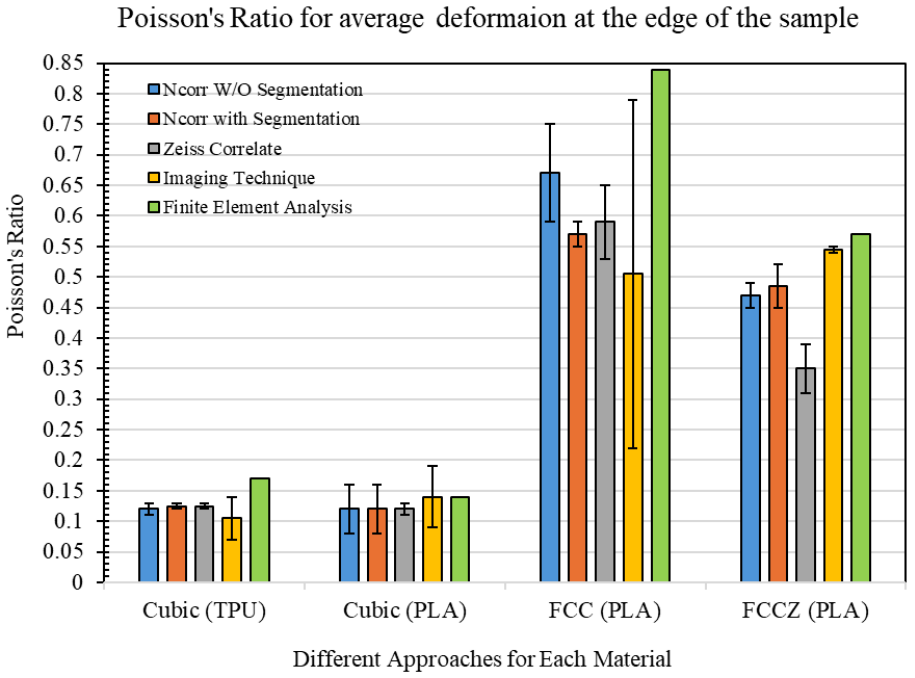


Figure 5.12: Poisson's ratio for average deformation along the edges of each sample

The overall observation on the Poisson's ratio of different lattice-structured materials implies that this property can vary based on measurement conditions and material state. It also exhibits the challenges of deformation measurement of lattice structures. The complex geometry of these materials and test conditions makes the unguided deformation unpredictable. Hence the Poisson's ratio varies largely among the same material.

5.3 Effects of Speckle Pattern on Result

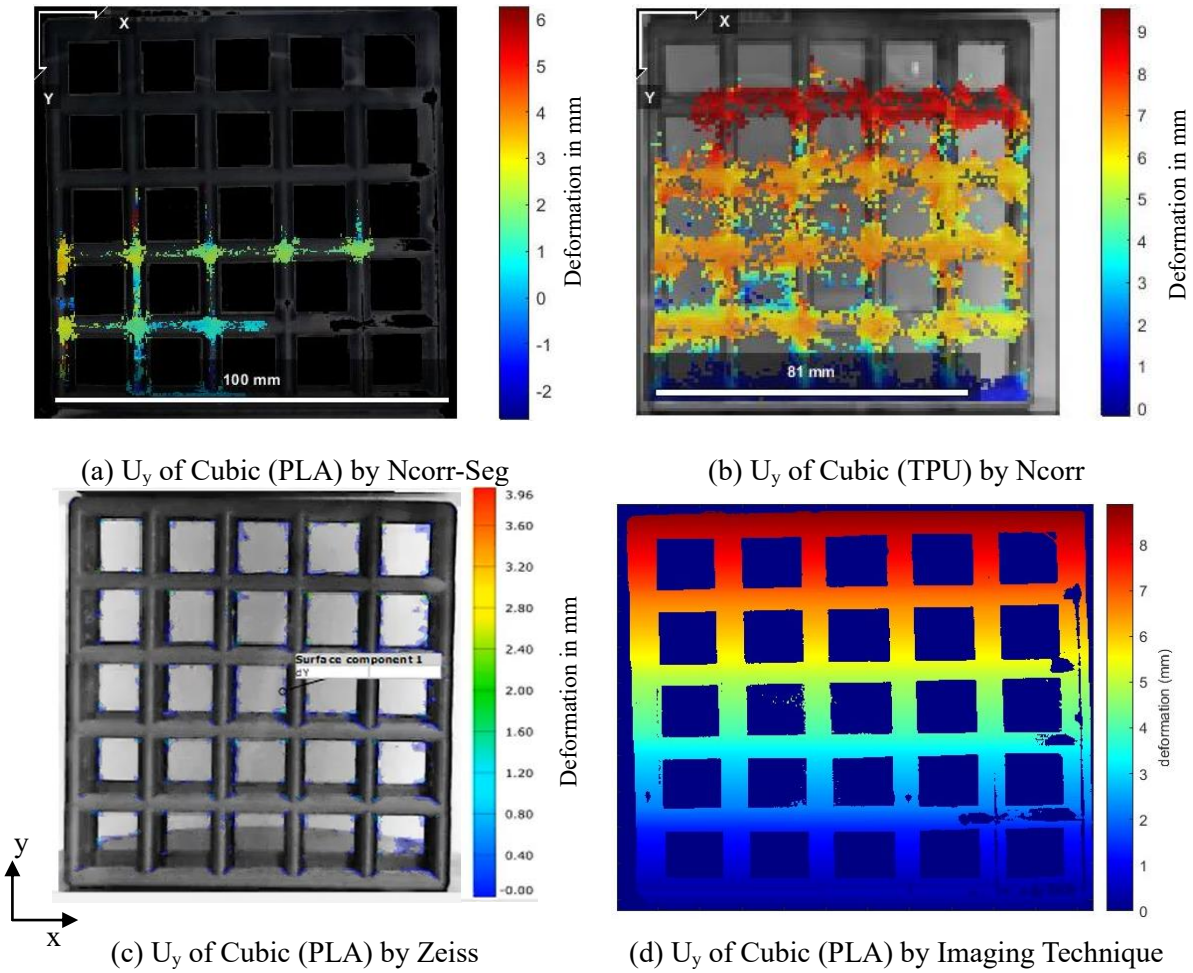
A good distinctive natural pattern on the surface or good quality speckle pattern is essential for DIC analysis. This research is conducted with both; natural patterns and speckle patterns. The speckle patterns are also provided in two different manners: speckle pattern through spray painting and speckle pattern through manual dots with sign pens. The detail of the speckling process is described in Chapter 3.3.2. The effect of speckle patterns on the results in this research is discussed here.

5.3.1 Deformation Analysis without Speckle Pattern

The DIC technique can be applied to samples without any speckle pattern. However, the results are ideal if the surface of the sample has some distinguishing pattern of its own. In this case, four Cubic Grid samples have been used to conduct DIC analysis without speckle patterns. Here, the surface of the Cubic Grid samples with PLA material have been smooth and uniform. Whereas the surface of the Cubic Grid samples with TPU material have been rough with a bit of a pattern. Both Ncorr and Zeiss Inspect Correlate fail to detect any surface component or Region of Interest (ROI) on samples with PLA material. For both PLA and TPU materials, Ncorr manages to detect the ROI in the initial picture but fails to trace it through the current images. Figure 5.13 demonstrates deformation at the end of the compression test of samples without speckle patterns in Y direction (U_y). The results of DIC analysis of Cubic Grid (PLA) samples can be seen in Figure 5.13(a) and Figure 5.13(c).

In case of DIC analysis with Cubic Grid (TPU) samples, Ncorr detects the ROI and gives a deformation analysis successfully as seen in Figure 5.13(b). On the other hand, Zeiss Inspect Correlate fails to detect any Surface Component or ROI for DIC analysis with Cubic Grid (TPU) samples. Figure 5.13(c) shows the initial image or reference image of the deformed sample with insignificant ROI detection by Zeiss Inspect Correlate.

On the other hand, the Imaging Technique do not require any speckle pattern for deformation analysis. Rather, the smooth and uniform surface makes it easier for the model to conduct the segmentation. However, the contrast between the foreground and the background needs to be higher for the model to achieve perfect segmentation. If the pixel value of the object and the background is similar, some portion of the object is also subtracted during background subtraction. The deformation analysis result from the I.T model through tracing all points is presented in Figure 5.13 (d).



(a) U_y of Cubic (PLA) by Ncorr-Seg

(b) U_y of Cubic (TPU) by Ncorr

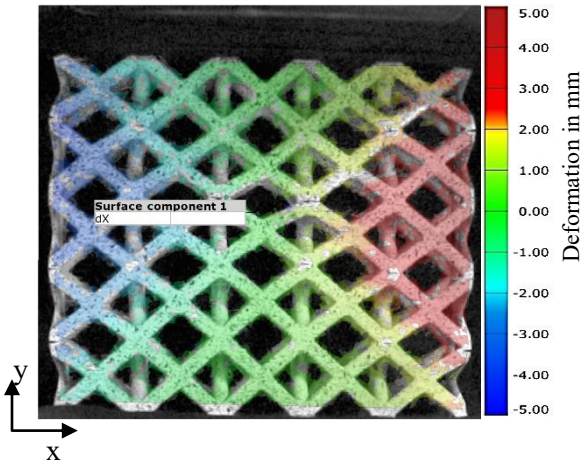
(c) U_y of Cubic (PLA) by Zeiss

(d) U_y of Cubic (PLA) by Imaging Technique

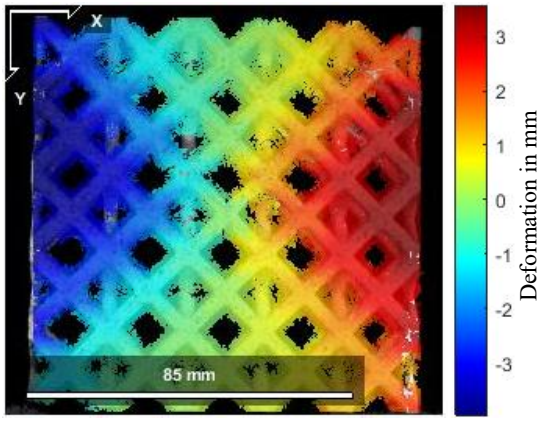
Figure 5.13: Deformation analysis of samples without speckle patterns

5.3.2 Deformation Analysis with Speckle Pattern

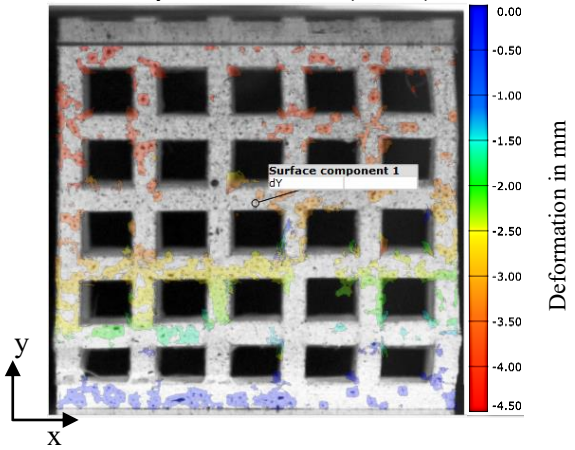
The DIC analysis results of the samples with random speckle patterns created by spray paint are good in both Ncorr and Zeiss. Figure 5.14 illustrates deformation in X Direction (U_x) and Y direction (U_y) at the end of the compression test of samples with speckle patterns.



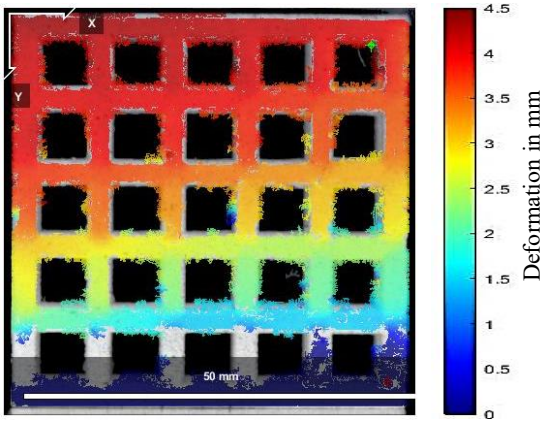
(a) U_x of FCC in X direction with Spray Speckle Pattern (Zeiss)



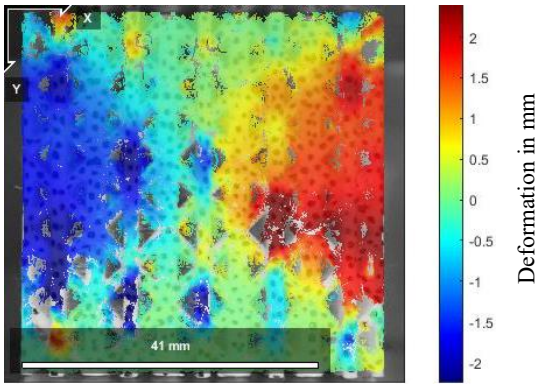
(b) U_x of FCC in X direction with Spray Speckle Pattern (Ncorr)



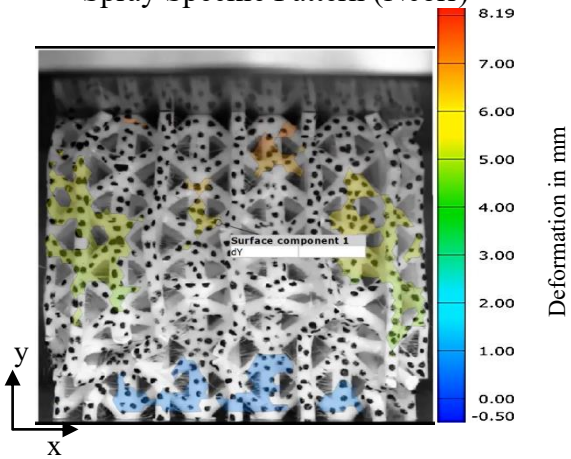
(c) U_y of Cubic (PLA) in Y direction with Spray Speckle Pattern (Zeiss)



(d) U_y of Cubic (PLA) in Y direction with Spray Speckle Pattern (Ncorr)



(e) U_x of BCCZ in X direction with Manual Speckle Pattern (Ncorr)



(f) U_y of BCCZ in Y direction with Manual Speckle Pattern (Zeiss)

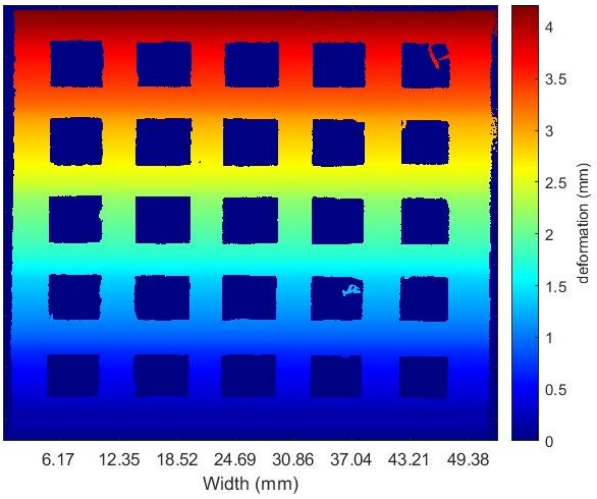
Figure 5.14: Deformation analysis with speckle pattern

From Figure 5.14(a) and Figure 5.14(b), it can be observed that the ROI detection is suitable for both of the software with spray painted random speckle patterns. However, the quality of the speckle pattern is an important consideration in DIC analysis; especially in Zeiss Inspect Correlate software. Low quality of speckle generates poor results on the software. One of the Cubic Grid (PLA) sample's pattern quality has been kept poor to observe that effect. Zeiss Inspect Correlate performs poorly in the case of that sample as shown in Figure 5.14(c). On the other hand, Figure 5.14(d) illustrates the result from DIC analysis in Ncorr providing a ROI coverage of 90%.

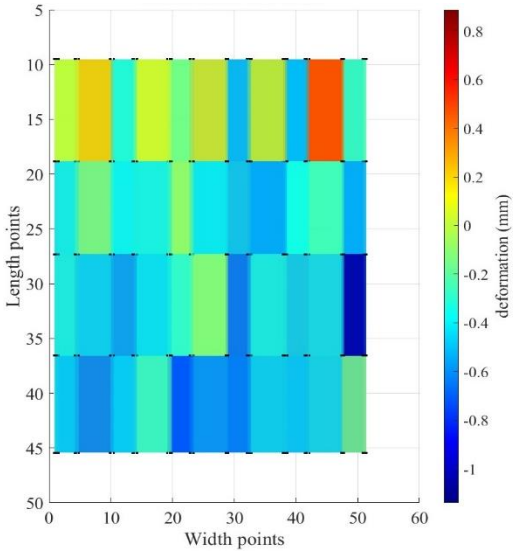
The DIC analysis results of samples with manually dotted speckle patterns are demonstrated in Figure 5.14(e) and Figure 5.14(f). The outcome for DIC analysis in Ncorr is better compared to the results from Zeiss inspect correlation. Ncorr detects the ROI well and generates a satisfactory deformation map. Whereas Zeiss Inspect Correlate detects the surface component or ROI on the reference image but fails to trace it through all the current images.

From the above discussion and results in Figure 5.14, it is evident that Ncorr provides better deformation map for both good quality speckle patterned samples and poor quality speckle patterned samples. Furthermore, this software generates moderate deformation map in case of naturally rough surface patterned samples without putting any artificial speckle pattern. However, it provides poor results in the case of smooth textured samples without any speckle patterns.

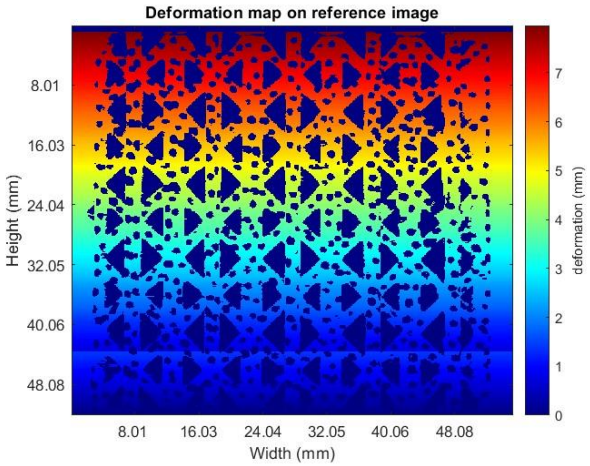
On the other hand, Zeiss Inspect Correlate generates an accurate deformation map only for samples with high quality speckle pattern. The software does not perform well with low-quality speckle patterns, whether spray painted or manually dotted. The outcomes for both smooth and rough textured samples without artificial speckle patterns are poor as well.



(a) U_y of Cubic (PLA) Sample with Poor Quality Speckle (Trace All Points)



(b) U_x of Cubic (TPU) Sample with Good Quality Speckle (Fixed Points)



(c) U_y of BCCZ Sample with Manually Dotted Speckle (Trace All Points)

Figure 5.15: Deformation map of samples with speckle pattern through Imaging Technique

On the contrary, the deformation analysis through Imaging Technique models developed for this research works well with any speckle pattern quality. The results in Figure 5.15 denote the results of analysis through Imaging Technique models for deformation in X direction (U_x) and deformation in Y direction (U_y). The results for Cubic grid (PLA) samples with poor speckle quality are found to be better with the Imaging Technique model (Figure 5.15(a)) than the results shown in Figure 5.14(b), (d). The model performs well with the Cubic grid (TPU) sample with good speckle quality as illustrated in Figure 5.15(b). The model also works moderately well on samples with manually dotted speckle pattern which is shown in Figure

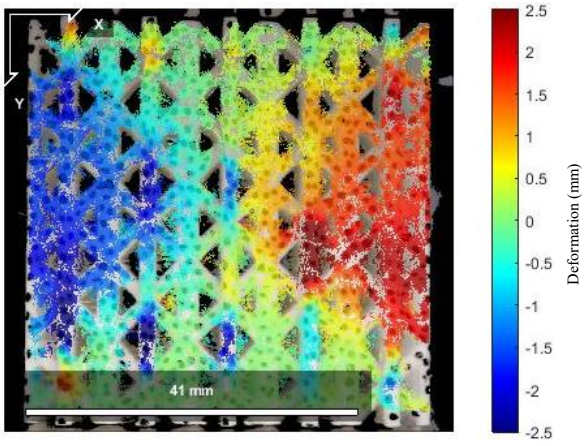
5.15(c). However, there is some error in background subtraction due to low contrast between the foreground and background.

Therefore, it is clear that the model created for this research can function effectively without speckle patterns on the sample. However, good background subtraction is required for the model to perform well, which necessitates a high contrast between the background and the object.

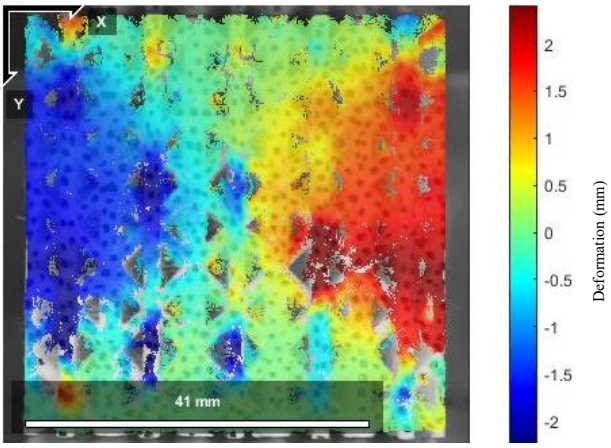
5.4 Effects of Out-of-Plane Struts

The BCC and BCCZ lattice-structured parts have been used in this research to observe the results of out-of-plane struts of lattice structures in 2D DIC and other image analysis techniques. Figure 5.16 shows the results of the DIC analysis of the BCCZ sample using Ncorr and Zeiss Inspect Correlate. Figure 5.16(a) and Figure 5.16(b) represent the U_x obtained from the DIC analysis in Ncorr with and without segmentation, respectively. Similarly, the U_y obtained from DIC analysis in Ncorr with and without segmentation are shown in Figure 5.16(c) and Figure 5.16(d), respectively. In addition, the DIC results in Zeiss Inspect Correlate for U_y at the end of the crush (60%) and at the initial level of the crush is demonstrated in Figure 5.16(e) and Figure 5.16(f), respectively.

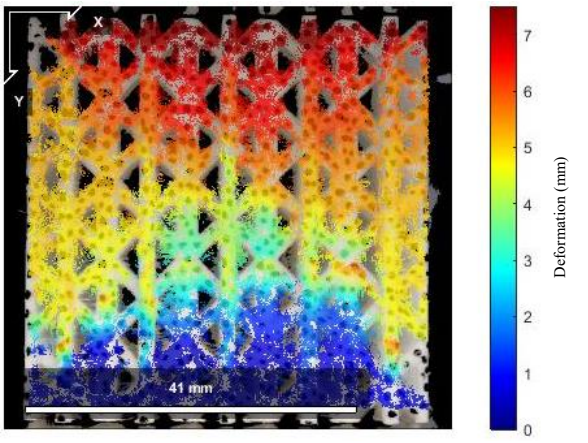
2D DIC analysis treats the out-of-plane struts on (x,y) plane surface as part of the planar struts on the surface plane. It does not consider the 3D effect of the BCC and BCCZ struts. Besides, there has been out of plane deformation during the crush which can be observed from the image of the sample at the end of the compression test in Figure 5.16(e). However, 2D DIC simply considers those deformations as planar deformation in X and Y directions. The results do not reflect the deformation in the sample that is perpendicular to the (x,y) plane. For samples with out-of-plane struts and deformation in the Z direction, the 3D DIC technique is more suitable.



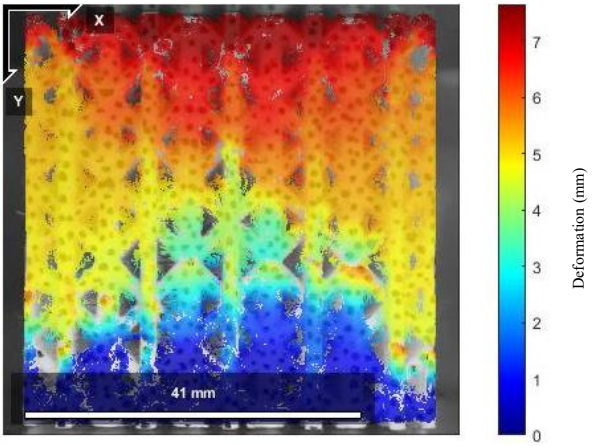
(a) U_x of BCCZ Sample in Ncorr (Segment)



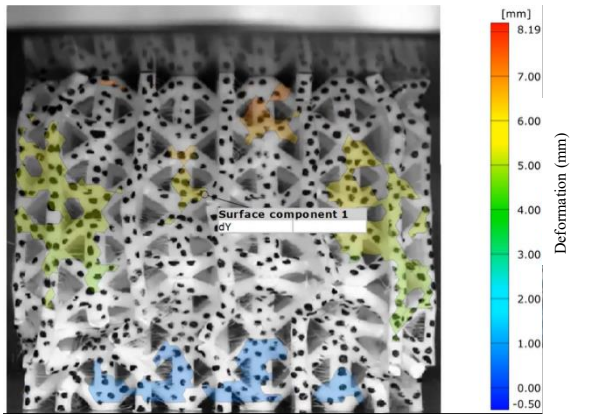
(b) U_x of BCCZ Sample in Ncorr



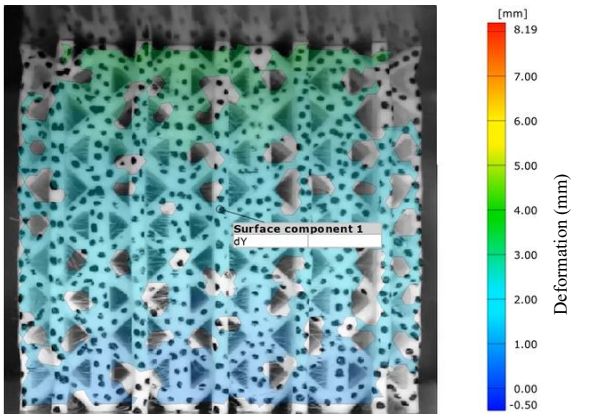
(c) U_y of BCCZ Sample in Ncorr (Segment)



(d) U_y of BCCZ Sample in Ncorr



(e) U_y of BCCZ Sample in Zeiss (Failure)

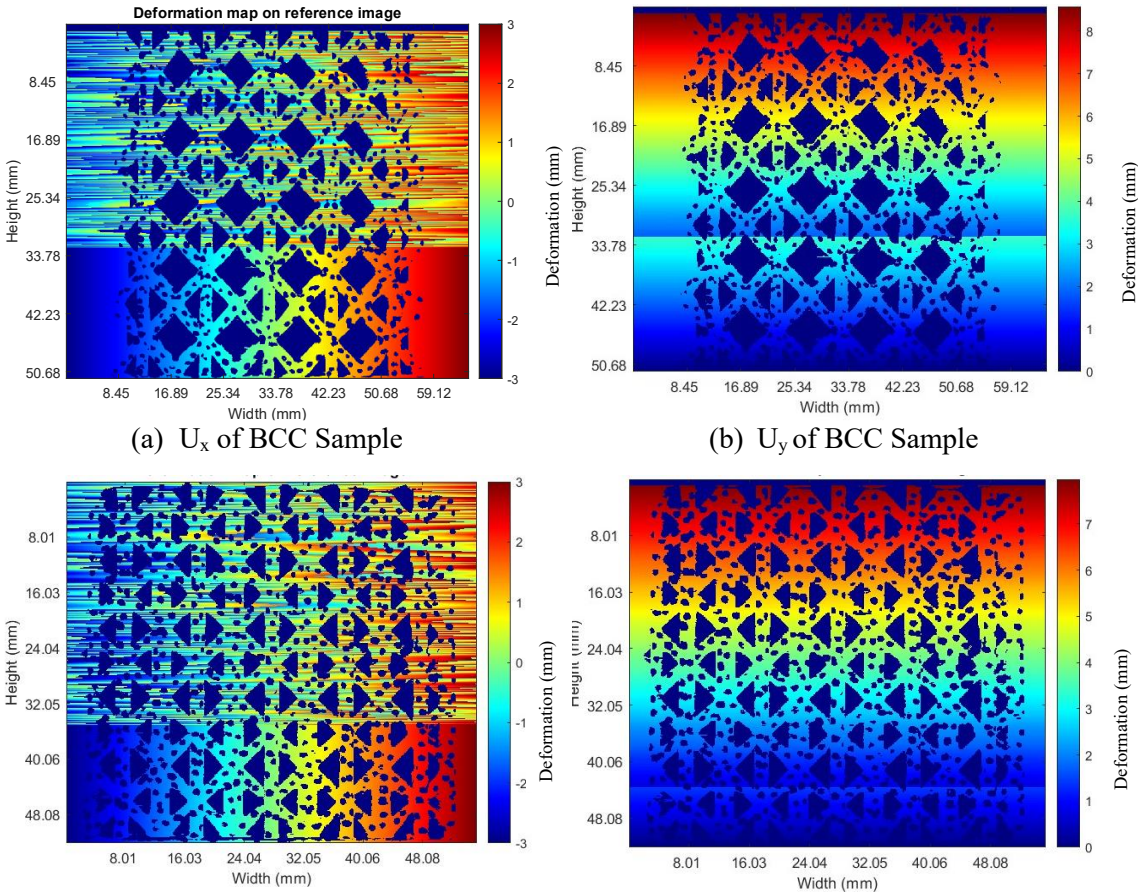


(f) U_y of BCCZ Sample in Zeiss (Initial)

Figure 5.16: DIC analysis in BCCZ lattice-structured materials with out-of-plane struts

From the results of the DIC analysis, it is observed that Zeiss Inspect Correlate successfully traces the ROI in the initial stages of the compression. The DIC analysis result of the initial stage of compression is provided in Figure 5.16(f). However, as the crush (%) increases, the

out-of-plane deformation also increases, leading the sample to failure. Therefore, the Zeiss software fails to recognize the ROI at the later stages of compression test.



(a) U_x of BCC Sample (b) U_y of BCC Sample

(c) U_x of BCCZ Sample (d) U_y of BCCZ Sample

Figure 5.17: Results of deformation analysis on samples with out of plane struts in All-Points-Model (Imaging Technique)

On the other hand, the BCC and BCCZ samples are representatives of samples with inexpensive hand-dotted speckle patterns. Ncorr successfully analyses these kinds of samples while Zeiss initially detects the ROI but fails to detect at 60% failure stage. The results of deformation analysis through tracing all points Imaging Technique model are also observed. The deformation in X and Y direction (U_x and U_y) of BCC lattice-structured sample in Imaging Technique model are illustrated in Figure 5.17(a) and Figure 5.17(b), respectively. Figure 5.17(c) and Figure 5.17(d) depict the deformation in X and Y direction (U_x and U_y) for the BCCZ lattice-structured sample through Imaging Technique model. This Imaging Technique works well for this type of samples and speckle patterns, in terms of ROI detection and tracking all the current images. The model has a similar limitation to DIC, as it does not represent the

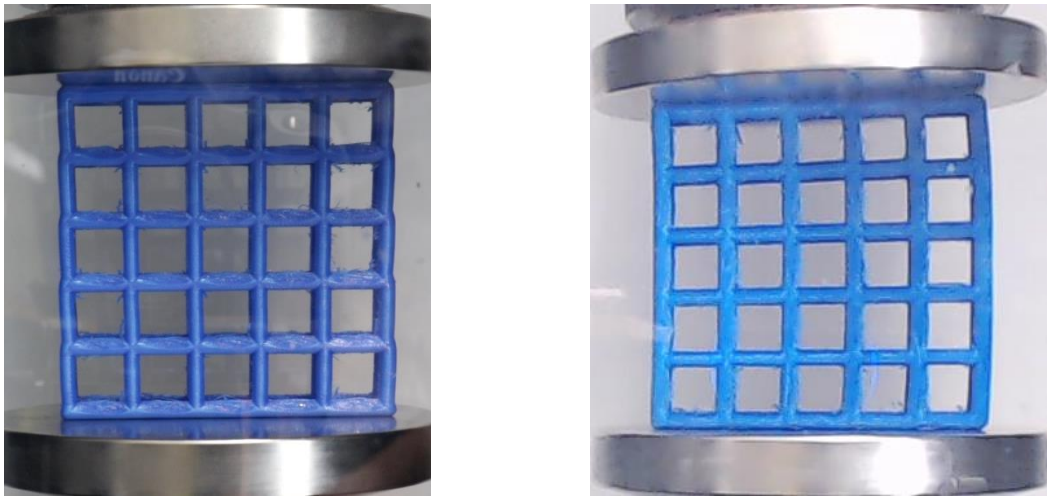
out-of-plane deformation or differentiate between struts on the (x,y) surface plane and struts outside of that plane.

5.5 Effects of Cameras

To observe the effects of different types of cameras on image analysis results, the images of the compression tests of two Cubic Grid (PLA and TPU) samples have been acquired through Logitech C920 HD Pro webcam. The technical specifications of the cameras are discussed in section 3.4. The other fourteen samples have been acquired through a DSLR camera. The DIC analysis software and the Imaging Technique models work well with the DSLR camera. The results from both techniques have been displayed in the previous sub-sections.

The image resolution is important for image analysis because the higher resolution provides better results. DIC analysis in Ncorr provides satisfactory result for TPU samples without speckle pattern as discussed in sub-section 5.3.1, which has been captured through a DSLR camera. Since the high-resolution camera provides more details of the natural pattern on the 3D-printed material, the DIC analysis has performed well. However, the DIC method has performed poorly for Cubic Grid (TPU) sample captured through webcam. This is due to the lower resolution of the webcam which could not display the textures on the sample properly for good DIC analysis. Therefore, no DIC results have been obtained for the Cubic Grid (TPU) sample without any speckles captured through webcam. Figure 5.18 displays the images of the Cubic Grid (TPU) samples captured through both cameras, showing that the DSLR image provides more information about the surface texture than the webcam image. However, further research on DIC analysis with speckle patterned sample images captured through webcam is recommended for developing cost efficient deformation measurement technique.

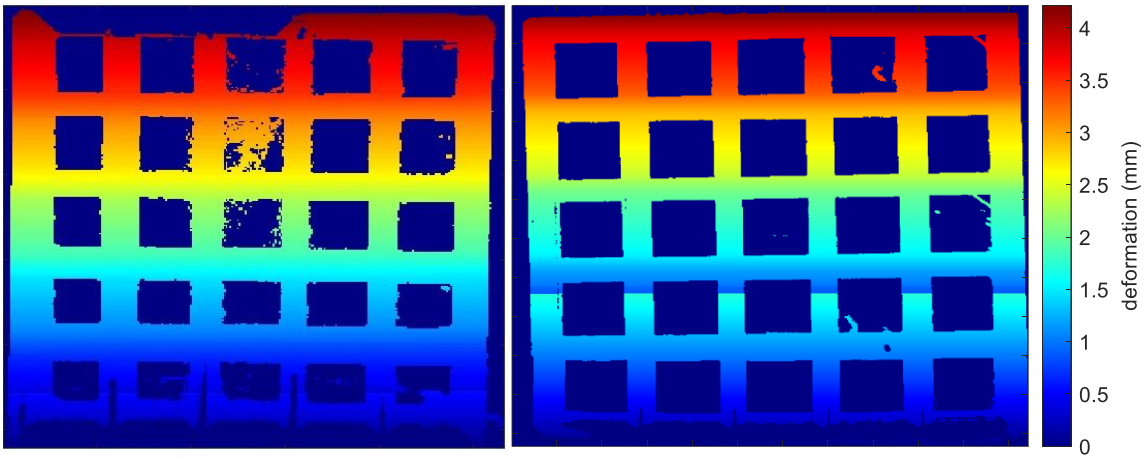
The results of the samples portrayed in Figure 5.18 represent buckling of Cubic TPU material in the same direction under loading instead of uniaxial symmetrical deformation like FEA results. This is due to the manufacturing defects and larger loading scenarios. These results are reported in this thesis only to compare the effect of cameras used in this research. The result in the elastic region is only utilised for validation purposes wherever possible.



(a) Sample Captured through DSLR (b) Sample Captured through Webcam

Figure 5.18: Images of Cubic Grid (TPU) samples during compression acquired through different cameras

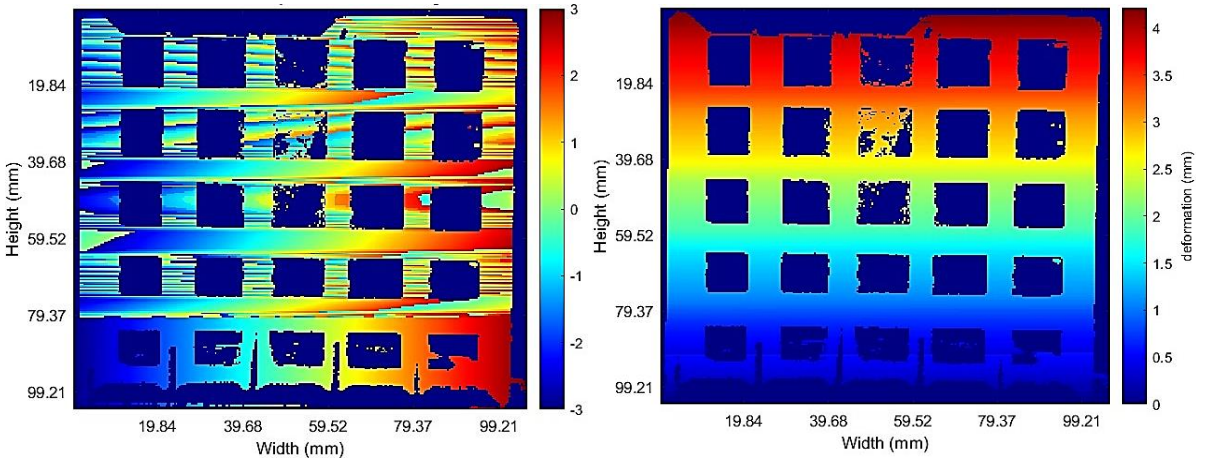
On the other hand, the Imaging Technique model functions effectively with both cameras. A comparison of deformation mapping through Imaging Technique Model using images from both of the cameras are shown in Figure 5.19.



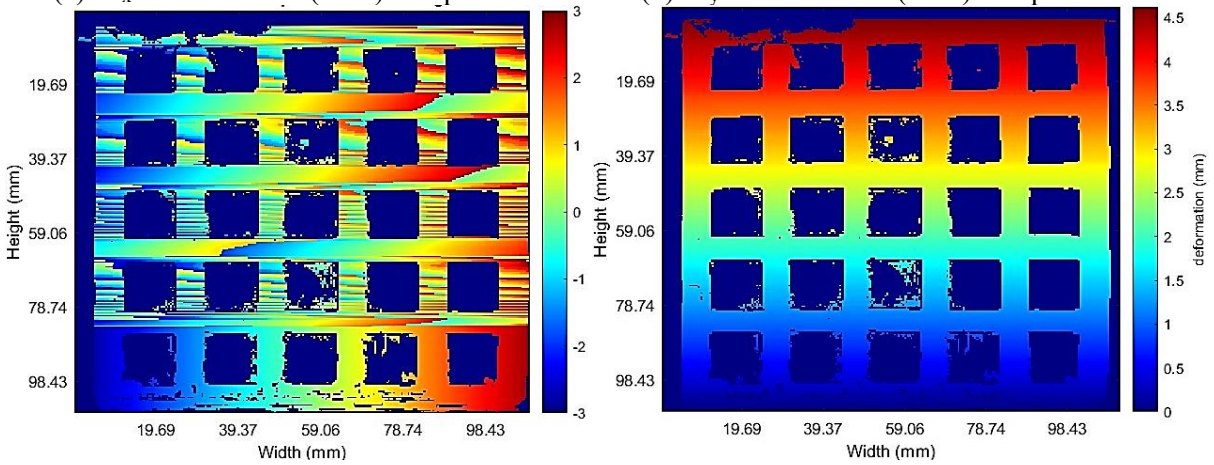
(a) Image acquired through webcam (b) Image acquired through DSLR camera

Figure 5.19: U_y of Cubic Grid (PLA) sample through I.T Model

The results of deformation in X (U_x) and Y (U_y) direction for samples collected through webcam is demonstrated in Figure 5.20. Since there is no requirement for unique surface texture or speckle patterns in the Imaging Technique model, the resolution of the webcam is adequate for the deformation analysis.



(a) U_x of Cubic Grid (PLA) Sample (b) U_y of Cubic Grid (PLA) Sample



(c) U_x of Cubic Grid (TPU) Sample (d) U_y of Cubic Grid (TPU) Sample

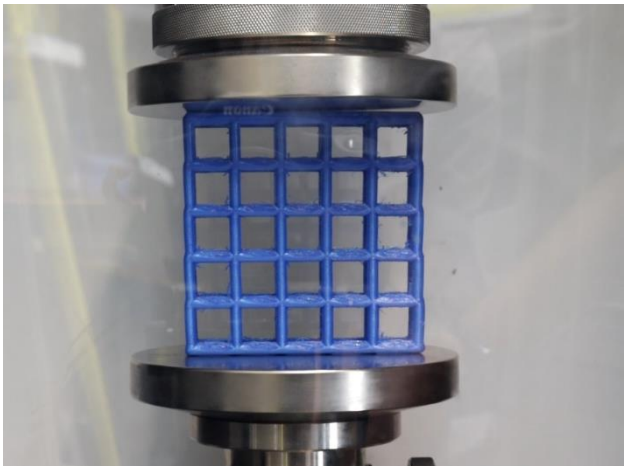
Figure 5.20: Deformation analysis in Imaging Technique Model of images acquired through webcam

In addition, webcam is preferable to DSLR in terms of being easily portable, controllable and for being economically feasible. Therefore, the webcam is recommended to consider for a low-cost deformation analysis option. Besides, the Imaging Technique model developed for this research is versatile with cameras as well. However, DSLR cameras are a suitable choice for projects with no financial constraints because they provide high-resolution images and improve DIC analysis results.

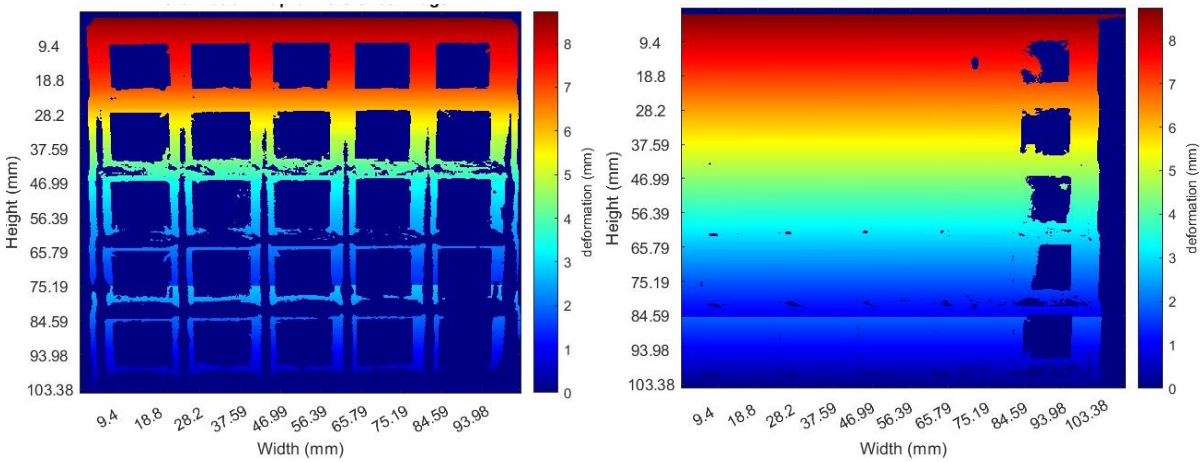
5.6 Effects of Background and Illumination

The details of background information and contrast on the images have been discussed in subsection 3.3.4.2 and subsection 4.2.1. In this subsection, the results of the effects on Tracing-all-points Imaging Technique Model are discussed.

During segmentation of object from the background, certain pixel value threshold is used to segment the pixel locations with the object. If the pixel value on the object is similar to the background, the following error occurs as shown in Figure 5.21. Due to illumination, some pixel location values of the object are similar to the pixel values of the background. Therefore, the error in deciding the threshold value for segmentation occurs.



(a) Reference Image



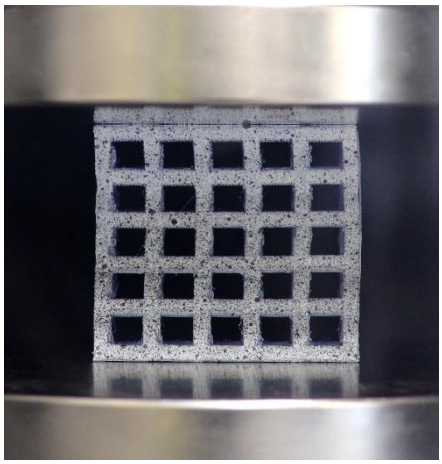
(b)Model with Lower Threshold (G>90) (c) Model with Higher Threshold (G>150)

Figure 5.21: Effects of background on results in Imaging Technique Model

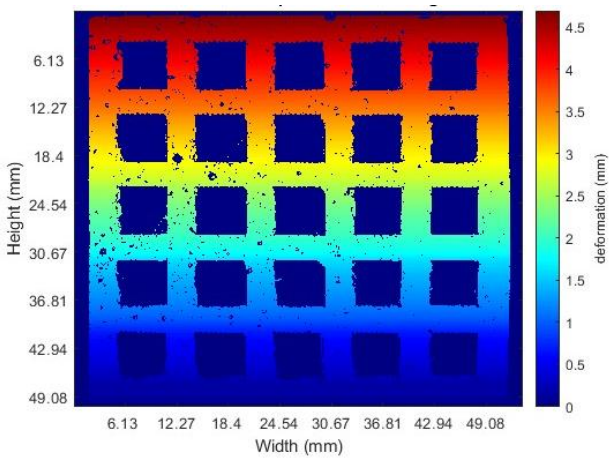
In this analysis, the locations with green colour pixel value > 90 have been removed for segmentation in Figure 5.21(b) which result in loss of object in the image. Subsequently, the locations with green colour pixel value > 150 have been removed in Figure 5.21(c) which result in including the background information in the result. Therefore, it is important to reduce the

effect of illumination and have a higher contrast in pixel values between the object and the background.

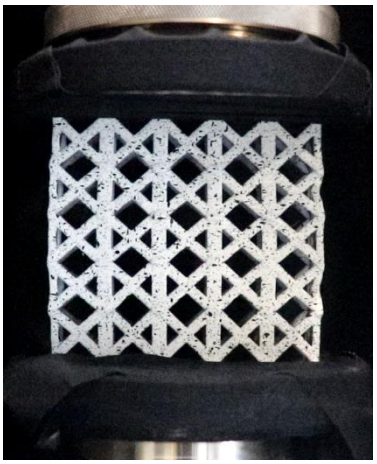
In order to eliminate the error, black backdrop in the background of the object and black tape on the compression pistons have been used. The results of Imaging Technique model with elimination of background effect and illumination are shown in Figure 5.22. From the figure, it is evident that the use of black backdrop for reducing background effect and use of black tape for reducing illumination improve the result significantly in Imaging Technique Model.



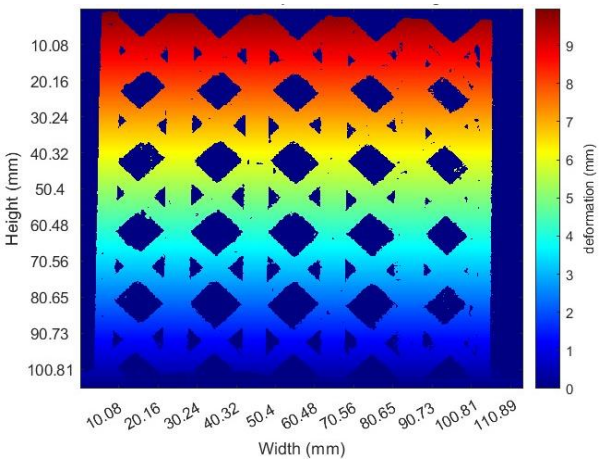
(a) Cubic (TPU) Current Image (Final)



(b) U_y of Cubic (TPU) in Imaging Technique



(c) FCCZ Current Image (Final)



(d) U_y of FCCZ in Imaging Technique

Figure 5.22: Results in Imaging Technique of samples after elimination of background effect and illumination

5.7 Discussion

The performance of the three approaches used for deformation analysis in this research will be discussed in this section. Even though every sample tested in this research has its own complexity, the approaches serve adeptly in calculating the 2D deformation across x,y plane surface.

5.7.1 Discussion on Ncorr

Ncorr is a Matlab-based open-source software with a simple GUI and program workflow. Even though it does not provide many options to customize the results, it provides good DIC analysis results that are compatible with the other DIC software. Additionally, Ncorr does not require powerful computers, making it cost-effective for common use. One of the most mentionable features of Ncorr is that it performs well with low quality speckle-patterned object. It also performs better than the other commercial software that has been used in this research for non-speckled samples.

There are two "Load Current Image" option in Ncorr: Load All and Load Lazy. If the Load All option is chosen, the software will store all the images in the workspace. This takes up more space in the RAM and slows down the performance. Therefore, Load Lazy is preferred to save RAM memory. However, it only stores the name and path of the images in "Load Lazy" mode. The images are later loaded on demand from their stored location in the computer and the DIC analysis cannot be run later if that directory is changed. In this regard, one of the limitations of Ncorr is that the saved DIC analysis cannot be run on different computers. On the other hand, Zeiss and Imaging Technique model in Matlab can run their already saved analysis later in other devices as long as the computer has the run file stored in them. The image directory can be changed as well for approaches other than Ncorr.

Overall, the performance of Ncorr is satisfactory in terms of accuracy in result, ease of use and economic feasibility.

5.7.2 Discussion on Zeiss Correlate

Zeiss Inspect Correlate is a commercially successful software which has been known formerly as GOM Correlate. The range of options for customization before and after the DIC analysis is exceptional. The GUI of the software and result modification options are found to be more

versatile compared to the open-source software. The software also has the ability to process videos for DIC analysis.

Nevertheless, the software performs inadequately for samples with low quality speckle pattern or samples without any speckle pattern. However, one of the reasons for worse results of the hand speckle patterned sample can be due to the percentage of crushing. The manually speckled sample set with BCC, BCCZ, FCC and FCCZ materials have been crushed until 60% failure unlike the other samples which have been crushed until 10% failure. Zeiss correlate serves sufficiently at the elastic deformation range of the compression test. But it has its limitation to detect deformation in those samples with high level of failure.

Additionally, the workspace window of Zeiss Inspect Correlate does not provide the pixel locations or coordinates on the current images. On the other hand, Matlab figures make it simple to find the pixel locations. Zeiss only supplies coordinates in the event that an Excel file was exported from the findings. Even so, the coordinates do not correspond to the locations of the pixels in Matlab. As a result, comparing the point deformation at a specific location on the image becomes challenging.

The performance evaluation on Zeiss Correlated discussed here is based on the 2D DIC Analysis option which is freely available. Zeiss also has a subscription-based version with additional features and 3D DIC analysis capabilities. For 2D DIC analysis of lattice-structured materials, Zeiss Inspect Correlate is often efficient because of its short computing time, accessibility, and extensive customisation possibilities.

5.7.3 Discussion on Imaging Technique Model

The Imaging Technique model developed for this research is based on the simple Cosine Correlation Based Distance Measurement formula. This model has potential to be customised for more complex calculations if given time. This model is highly customizable with low computational cost and high flexibility.

Despite the unique geometry and complex deformation pattern of the lattice-structured parts, the Imaging Technique model has been competent in calculating 2D deformation on the front surface of the lattice-structured materials. The results obtained from this model are compatible with the results from commercially successful DIC software and a well-known open-source

DIC software. In some cases, this model provides better outcomes than the DIC analysis. Therefore, it can be said that the Imaging Technique model developed for this research succeeds adequately in deformation analysis of 3D-printed lattice-structured materials.

Nonetheless, the model has its limitation in measuring deformation in images with low contrast between the object and background. Further exploration on this model can be done to eliminate this error. Moreover, there is scope of improvement in detecting deformation in X direction (U_x) more effectively.

5.8 Conclusion

A comprehensive discussion on the outcomes of this research is presented in this chapter. FEA consistently predicts symmetric deformation (equal magnitude but opposite signs), while a few experimental methods show varying asymmetry due to manufacturing or experimental error. DIC portrays the actual experimental outcomes accurately despite the defects. The FEA validation is applicable only for deformation in the elastic region and the deformation beyond elastic region is not considered for validation purposes in this research. Keeping this in mind, DIC is found to be a reliable technique for deformation measurement of AM lattice-structured materials. Although DIC has some limitations in specific conditions (such as analysis of untextured/plain samples), those limitations are overcome by the Imaging Technique model. The Imaging Technique model developed for this research works particularly well for deformation in the Y direction for all kinds of materials and conditions. However, the Imaging Technique model could be improved further for deformation measurement in the X direction. Due to its unique deformation direction and susceptibility to environmental error, deformation measurement in the X direction is more challenging. DIC techniques are successful in portraying the actual deformation U_x. Further experiments incorporating samples with higher accuracy in 3D printing, focusing on results from the elastic zone and avoiding experimental defects, are required to validate the DIC analysis results with FEA for U_x in the future.

Chapter 6: Conclusions and Future Work

6.1 Conclusions

This research investigated the deformation behaviour of 3D-printed lattice-structured materials through advanced image analysis techniques and Finite Element modelling. The study used multiple lattice configurations such as Cubic, Face-Centred Cubic (FCC), and Face-Centred Cubic with Z struts (FCCZ) to visually analyse their mechanical responses under compression loading. By developing and comparing different approaches from DIC to proposed Imaging Technique model, this research addressed the critical need for reliable deformation analysis technique in 3D-printed lattice-structured materials. The findings contribute to the understanding of complex geometric deformation patterns while establishing a comprehensive dataset for future investigations in this field.

The experimental results show non-uniform deformation due to complex loading conditions and geometry. On the other hand, the FEA results show uniform deformation on each surface layer (top, left and right) of the sample. The FEA results are compared with the DIC and Imaging Technique model results and the deformation plots of U_y for all the materials are visually aligned with the FEA diagrams. However, the U_x deformation plots of Cubic samples visually deviate from the FEA plots due to different deformation direction in experimental conditions. This is particularly due to small defects in experimental specimens, discrepancy in size of struts in comparison to ideal samples in FEM. The point and average U_y values at the edges of all the image analysis approaches deviate 1-10% from the testing machine and FEA results. The U_y from the testing machine and FEA are considered the ground truth for validation of other approaches for U_y. Zeiss Inspect and Imaging Technique model work best among all the methods for U_y with a maximum 7% and 6% deviation from the ground truth, respectively. The average deviations from the ground truth for each approach are 7.5% for Ncorr, 5% for Ncorr with segmentation, 4.5% for Zeiss and 4% for the Imaging Technique model. The deviation percentage ranges are higher for FCC and FCCZ materials due to the complex geometry. Even then, the Imaging Technique model exhibits 3-4% deviation from the FEA and testing machine results. It is also observed that incorporating the novel segmentation approach in this research improves the performance of Ncorr.

The deformation in the X direction is unguided during the compression test and the experimental methods show asymmetric U_x unlike FEA. Despite this, the DIC analysis approaches are compared with each other, and the deformation plots are visually in agreement with each other. Ncorr and Ncorr-seg produce very similar results with variation typically within 0.05mm and Zeiss produces higher deformation values than these two. Although the magnitudes of the DIC results are compared with FEA results, Zeiss's results have proven to be closer. The Imaging Technique model results for Cubic samples align with the FEA results with a 4.4-42% average deviation. On the other hand, the U_x results, and deformation direction of the experiment align with the FEA results for FCC and FCCZ materials. The Imaging Technique model works best for FCC and FCCZ samples with a 0.5-5.6% deviation from FEA results. Whereas Ncorr has a 12-29%, Ncorr-seg has a 11-38%, Zeiss has a 19.5-56% deviation from FEA results. The deviations of experimental values from FEA in FCCZ structures are found to be higher which could be due to complex stress interactions from additional Z-struts.

Additionally, the validation of U_x for all the approaches is challenging due to the lack of experimental data for the X direction deformation. Another challenge present for average U_x calculation is due to bidirectional deformation values for each material types and the unique deformation of each sample due to experimental and material printing discrepancies. Therefore, establishing material-specific averages and overall performance metrics for different approaches is challenging.

The comparison of Poisson's Ratio highlights the challenges of full-field deformation measurement of 3D-printed lattice-structured parts. Due to varied outcomes of U_x within the same materials, the Poisson's Ratio of that material varies significantly. Although the Poisson's ratio from average deformation is considered more ideal, the Poisson's Ratio from point deformation values is closer to the FEA values, with a deviation of 4-13%. In contrast, the average deformation Poisson's ratio deviates by up to 25% from FEA results. This implies that the FEA generates uniform values across the surface layer, similar to the experimental deformation at the surface midpoints. Additionally, the average results of Poisson's ratio for different approaches indicate that the Imaging Technique model has the best result, with a deviation of 16-19% from the FEA results. Among the DIC approaches, Zeiss and Ncorr-seg have similar results of 17% deviation from FEA results.

To summarise, Zeiss has performed best among the DIC software, while Ncorr's performance has improved with the integration of segmentation. The Imaging Technique shows promising results for U_y in tracing-all-points algorithm; further research could improve the performance of U_x detection as well. The fixed points model also successfully provides point deformation results competitive with DIC and FEA for simple Cubic Grid lattice. Furthermore, DIC portrays experimental outcomes accurately, making it a reliable technique for full-field deformation measurement technique for lattice-structured parts. Additionally, it is observed that different factors affect the results of different image analysis techniques. Some of the parameters affecting the results are as follows:

- While Ncorr works great with standard-quality or low-quality speckle patterns, Zeiss's performance is limited to standard quality speckle patterns on the surface only. Ncorr even partially detects and analyses samples with natural textured surfaces without speckle patterns, but Zeiss fails to do so. On the other hand, Imaging Technique model performs perfectly with all types of surfaces even without speckle patterns.
- The research observes the effect of out-of-plane strut samples such as BCC and BCCZ on the 2D DIC analysis system. The system identifies the out-of-plane struts as planar surface and generates the result as planar surface deformation. 3D DIC is recommended for further investigation of the deformation measurement of these materials.
- Image resolution is an important factor in DIC analysis. DIC analysis has performed better with high-resolution images from DSLR cameras compared to images from the webcam.
- On the contrary, the Imaging Technique model does not require a high-resolution camera, hence the combination of Imaging Technique and webcam could be a good option for low-budget research projects.
- High contrast pixel values between background and object are necessary for segmentation and deformation measurement in the Imaging Technique model. The high contrast is created by using a black backdrop as the background.
- The illumination on the object highly affects the results which are resolved by use of a black backdrop and black tape on the reflecting surfaces nearby.

6.2 Recommendations for Future Work

The limitations of this study include constraints related to time and budget. The complex nature of the material, highly sensitive experimental setup and processing of large number of images have been particularly challenging as well. There are scopes for improvements and further studies on this research topic. A few of the recommendations for future research are:

- Explore the measurement of unguided deformation in X direction by incorporating methods to measure experimental ground truth which is a benchmark to evaluate the performance of the models.
- Implement 3D or Stereo DIC technique on 3D-printed lattice-structured materials. Explore different sizes, more complicated shapes and configurations to enhance the verification further.
- Enhance the Imaging Technique model further for improvement of results in the X direction
- Conduct more research to understand the reasons behind significant result deviation in different samples of the same material by incorporating resin SLA materials or other AM technologies with higher accuracy in printing and different experimental condition and sample size.

References

[1] G. Liu *et al.*, "Additive manufacturing of structural materials," Jul. 01, 2021, *Elsevier Ltd*. doi: 10.1016/j.mser.2020.100596.

[2] Y. Huang, M. C. Leu, J. Mazumder, and A. Donmez, "Additive manufacturing: Current state, future potential, gaps and needs, and recommendations," *Journal of Manufacturing Science and Engineering, Transactions of the ASME*, vol. 137, no. 1, 2015, doi: 10.1115/1.4028725.

[3] A. Hussain, A. H. Sakhaei, and M. Shafiee, "A Data-Driven Constitutive Model for 3D Lattice-Structured Material Utilising an Artificial Neural Network," *Applied Mechanics*, vol. 5, no. 1, pp. 212–232, Mar. 2024, doi: 10.3390/applmech5010014.

[4] H. Zhong, T. Song, C. Li, R. Das, J. Gu, and M. Qian, "The Gibson-Ashby model for additively manufactured metal lattice materials: Its theoretical basis, limitations and new insights from remedies," *Curr Opin Solid State Mater Sci*, vol. 27, no. 3, Jun. 2023, doi: 10.1016/j.cossms.2023.101081.

[5] A. Modir and I. Tansel, "Structural Health Monitoring of Additively Manufactured Parts by Combining Infill Design, Multiple Pulse Width Excitation (MPWE), and Deep Learning," *Journal of Vibration Engineering and Technologies*, vol. 10, no. 8, pp. 3227–3238, Nov. 2022, doi: 10.1007/s42417-022-00553-5.

[6] O. Holzmond and X. Li, "In situ real time defect detection of 3D printed parts," *Addit Manuf*, vol. 17, pp. 135–142, Oct. 2017, doi: 10.1016/j.addma.2017.08.003.

[7] S. S. Murugan, "Mechanical Properties of Materials: Definition, Testing and Application," *International Journal of Modern Studies in Mechanical Engineering (IJMSME)*, vol. 6, no. 2, pp. 28–38, 2020, doi: 10.20431/2454-9711.0602003.

[8] L. J. Gibson, M. F. Ashby, and B. A. Harley, *Cellular materials in nature and medicine*. Cambridge University Press, 2010.

[9] P. Köhnen, C. Haase, J. Bültmann, S. Ziegler, J. H. Schleifenbaum, and W. Bleck, "Mechanical properties and deformation behavior of additively manufactured lattice

structures of stainless steel," *Mater Des*, vol. 145, pp. 205–217, May 2018, doi: 10.1016/j.matdes.2018.02.062.

[10] K. Hoffmann, "An Introduction to Stress Analysis and Transducer Design using Strain Gauges," 2012. [Online]. Available: www.hbm.com

[11] G. İRSEL, "Research on electrical strain gages and experimental stress analysis: Case study for a full wheatstone bridge," *DÜMF Mühendislik Dergisi*, pp. 783–792, Dec. 2021, doi: 10.24012/dumf.1051434.

[12] C. Ferraris, G. Amprimo, and G. Pettiti, "Computer Vision and Image Processing in Structural Health Monitoring: Overview of Recent Applications," *Signals*, vol. 4, no. 3, pp. 539–574, Jul. 2023, doi: 10.3390/signals4030029.

[13] Y. Bao, Z. Tang, H. Li, and Y. Zhang, "Computer vision and deep learning–based data anomaly detection method for structural health monitoring," *Struct Health Monit*, vol. 18, no. 2, pp. 401–421, Feb. 2018, doi: 10.1177/1475921718757405.

[14] C.-Z. Dong and F. N. Catbas, "A review of computer vision–based structural health monitoring at local and global levels," *Struct Health Monit*, vol. 20, no. 2, pp. 692–743, Jul. 2020, doi: 10.1177/1475921720935585.

[15] A. S. Dickinson, A. C. Taylor, H. Ozturk, and M. Browne, "Experimental Validation of a Finite Element Model of the Proximal Femur Using Digital Image Correlation and a Composite Bone Model," *J Biomech Eng*, vol. 133, no. 1, Dec. 2010, doi: 10.1115/1.4003129.

[16] D. Zhang, C. D. Eggleton, and D. D. Arola, "Evaluating the mechanical behavior of arterial tissue using digital image correlation," *Exp Mech*, vol. 42, no. 4, pp. 409–416, Dec. 2002, doi: 10.1007/BF02412146

[17] C. Rehrl, S. Kleber, T. Antretter, and R. Pippan, "A methodology to study crystal plasticity inside a compression test sample based on image correlation and EBSD," *Mater Charact*, vol. 62, no. 8, pp. 793–800, 2011, doi: 10.1016/j.matchar.2011.05.009.

[18] B. Reedlunn, S. Daly, L. Hector, P. Zavattieri, and J. Shaw, “Tips and tricks for characterizing shape memory wire part 5: Full-field strain measurement by digital image correlation,” *Exp Tech*, vol. 37, no. 3, pp. 62–78, May 2013, doi: 10.1111/j.1747-1567.2011.00717.x.

[19] A. Antoniou, P. R. Onck, and A. F. Bastawros, “Experimental analysis of compressive notch strengthening in closed-cell aluminum alloy foam,” *Acta Mater*, vol. 52, no. 8, pp. 2377–2386, May 2004, doi: 10.1016/j.actamat.2004.01.028.

[20] M. Jerabek, Z. Major, and R. W. Lang, “Strain determination of polymeric materials using digital image correlation,” *Polym Test*, vol. 29, no. 3, pp. 407–416, May 2010, doi: 10.1016/j.polymertesting.2010.01.005.

[21] Y. Wang and A. M. Cuitiño, “Full-field measurements of heterogeneous deformation patterns on polymeric foams using digital image correlation,” *Int J Solids Struct*, vol. 39, no. 13–14, pp. 3777–3796, Jun. 2002, doi: 10.1016/S0020-7683(02)00176-2.

[22] J. Blaber, B. Adair, and A. Antoniou, “Ncorr: Open-Source 2D Digital Image Correlation Matlab Software,” *Exp Mech*, vol. 55, no. 6, pp. 1105–1122, Jul. 2015, doi: 10.1007/s11340-015-0009-1.

[23] G. M. Hassan, “Deformation measurement in the presence of discontinuities with digital image correlation: A review,” Feb. 01, 2021, *Elsevier Ltd*. doi: 10.1016/j.optlaseng.2020.106394.

[24] B. Pan, “Digital image correlation for surface deformation measurement: Historical developments, recent advances and future goals,” Jun. 28, 2018, *Institute of Physics Publishing*. doi: 10.1088/1361-6501/aac55b.

[25] Y. Zhu, E. Polyzos, and L. Pyl, “Stiffness optimisation of sandwich structures with elastically isotropic lattice core,” *Thin-Walled Structures*, vol. 195, Feb. 2024, doi: 10.1016/j.tws.2023.111408.

[26] P. L. Reu *et al.*, “DIC Challenge: Developing Images and Guidelines for Evaluating Accuracy and Resolution of 2D Analyses,” *Exp Mech*, vol. 58, no. 7, pp. 1067–1099, Sep. 2018, doi: 10.1007/s11340-017-0349-0.

[27] S. F. Iftekar, A. Aabid, A. Amir, and M. Baig, “Advancements and Limitations in 3D Printing Materials and Technologies: A Critical Review,” Jun. 01, 2023, *MDPI*. doi: 10.3390/polym15112519.

[28] G. P. Borikar, A. R. Patil, and S. B. Kolekar, “Additively Manufactured Lattice Structures and Materials: Present Progress and Future Scope,” Nov. 01, 2023, *SpringerOpen*. doi: 10.1007/s12541-023-00848-x.

[29] M. K. Thompson *et al.*, “Design for Additive Manufacturing: Trends, opportunities, considerations, and constraints,” *CIRP Ann Manuf Technol*, vol. 65, no. 2, pp. 737–760, 2016, doi: 10.1016/j.cirp.2016.05.004.

[30] U. Maheshwaraa, D. Bourell, and C. C. Seepersad, “Design and freeform fabrication of deployable structures with lattice skins,” *Rapid Prototyp J*, vol. 13, no. 4, pp. 213–225, 2007, doi: 10.1108/13552540710776160.

[31] G. Reinhart, S. Teufelhart, and F. Riss, “Investigation of the Geometry-Dependent Anisotropic Material Behavior of Filigree Struts in ALM-Produced Lattice Structures,” in *Physics Procedia*, Elsevier B.V., 2012, pp. 471–479. doi: 10.1016/j.phpro.2012.10.063.

[32] J. Hulme, A. H. Sakhaei, and M. Shafiee, “Mechanical analysis and additive manufacturing of 3D-printed lattice materials for bone scaffolds,” *Mater Today Proc*, 2023, doi: 10.1016/j.matpr.2023.02.278.

[33] D. Qin, L. Sang, Z. Zhang, S. Lai, and Y. Zhao, “Compression Performance and Deformation Behavior of 3D-Printed PLA-Based Lattice Structures,” *Polymers (Basel)*, vol. 14, no. 5, Mar. 2022, doi: 10.3390/polym14051062.

[34] A. Modir and I. Tansel, “Analysis of Force Sensing Accuracy by Using SHM Methods on Conventionally Manufactured and Additively Manufactured Small Polymer Parts,” *Polymers (Basel)*, vol. 14, no. 18, Sep. 2022, doi: 10.3390/polym14183755.

[35] B. Bahrami Babamiri, H. Askari, and K. Hazeli, “Deformation mechanisms and post-yielding behavior of additively manufactured lattice structures,” *Mater Des*, vol. 188, Mar. 2020, doi: 10.1016/j.matdes.2019.108443.

[36] D. G. Firsov, S. D. Konev, O. N. Dubinin, S. A. Evlashin, and I. V. Shishkovsky, “Localization of Deformation in Lattice Structures of 3D-Printed Samples of 03X17H14M2 Steel,” *Technical Physics Letters*, vol. 46, no. 7, pp. 683–686, Jul. 2020, doi: 10.1134/S1063785020070160.

[37] L. Ngeljaratan and M. A. Moustafa, “Structural health monitoring and seismic response assessment of bridge structures using target-tracking digital image correlation,” *Eng Struct*, vol. 213, Jun. 2020, doi: 10.1016/j.engstruct.2020.110551.

[38] S. Ri, M. Fujigaki, and Y. Morimoto, “Sampling Moiré Method for Accurate Small Deformation Distribution Measurement,” *Exp Mech*, vol. 50, no. 4, pp. 501–508, Apr. 2010, doi: 10.1007/s11340-009-9239-4.

[39] B. Pan, K. Qian, H. Xie, and A. Asundi, “Two-dimensional digital image correlation for in-plane displacement and strain measurement: A review,” *Meas Sci Technol*, vol. 20, no. 6, 2009, doi: 10.1088/0957-0233/20/6/062001.

[40] F. L. Dai and Z. Y. Wang, “Geometric micron-moiré,” *Opt Lasers Eng*, vol. 31, no. 3, pp. 191–198, Mar. 1999, doi: 10.1016/S0143-8166(99)00020-2.

[41] Q. Wang, S. Kishimoto, and Y. Yamauchi, “Structural Analysis of a Micro Hexagonal Mesh Using a Three-way Grating by Hexagonal Digital Moire Method,” *Journal of the Japanese Society for Experimental Mechanics*, vol. 13, Jul. 2013.

[42] Y. Morimoto and M. Fujigaki, “MOIRÉ METHODS FOR SHAPE, DISPLACEMENT AND STRAIN ANALYSIS,” *Opt. Eng*, vol. 50, 2011.

[43] S. Ri, Q. Wang, H. Tsuda, H. Shirasaki, and K. Kuribayashi, “Deflection Measurement of Bridge Using Images Captured Under the Bridge by Sampling Moiré Method,” *Exp Tech*, vol. 47, no. 5, pp. 1085–1095, Oct. 2023, doi: 10.1007/s40799-022-00616-y.

[44] C. Z. Dong, X. W. Ye, and T. Jin, “Identification of structural dynamic characteristics based on machine vision technology,” *Measurement (Lond)*, vol. 126, pp. 405–416, Oct. 2018, doi: 10.1016/j.measurement.2017.09.043.

[45] Y.-H. Tseng, J.-J. Tzen, K.-P. Tang, and S.-H. Lin, “Image-to-image registration by matching area features using Fourier descriptors and neural networks,” *Photogramm Eng Remote Sensing*, vol. 63, no. 8, pp. 975–983, Aug. 1997.

[46] B. Zitová and J. Flusser, “Image registration methods: A survey,” *Image Vis Comput*, vol. 21, no. 11, pp. 977–1000, 2003, doi: 10.1016/S0262-8856(03)00137-9.

[47] P. Rutesic and Zorana Stosic, “Image registration based on normalized cross correlation and discrete cosine transform,” *International Journal of Signal Processing*, vol. 3, Mar. 2018.

[48] X. Tong *et al.*, “Image Registration with Fourier-Based Image Correlation: A Comprehensive Review of Developments and Applications,” *IEEE J Sel Top Appl Earth Obs Remote Sens*, vol. 12, no. 10, pp. 4062–4081, Oct. 2019, doi: 10.1109/JSTARS.2019.2937690.

[49] J. Wu, Z. Cui, V. S. Sheng, P. Zhao, D. Su, and S. Gong, “A comparative study of SIFT and its variants,” *Measurement Science Review*, vol. 13, no. 3, pp. 122–131, Jun. 2013, doi: 10.2478/msr-2013-0021.

[50] H. Bay, A. Ess, T. Tuytelaars, and L. Van Gool, “Speeded-Up Robust Features (SURF),” *Computer Vision and Image Understanding*, vol. 110, no. 3, pp. 346–359, Jun. 2008, doi: 10.1016/j.cviu.2007.09.014.

[51] Z. Wang, H. Kieu, H. Nguyen, and M. Le, “Digital image correlation in experimental mechanics and image registration in computer vision: Similarities, differences and

complements," *Opt Lasers Eng*, vol. 65, pp. 18–27, Feb. 2015, doi: 10.1016/j.optlaseng.2014.04.002.

[52] N. Sudarsanan, A. Arulrajah, R. Karpurapu, and V. Amrithalingam, "Digital Image Correlation Technique for Measurement of Surface Strains in Reinforced Asphalt Concrete Beams under Fatigue Loading," *Journal of Materials in Civil Engineering*, vol. 31, no. 8, Aug. 2019, doi: 10.1061/(ASCE)MT.1943-5533.0002743.

[53] S. Sankarasrinivasan, E. Balasubramanian, K. Karthik, U. Chandrasekar, and R. Gupta, "Health Monitoring of Civil Structures with Integrated UAV and Image Processing System," in *Procedia Computer Science*, Elsevier, 2015, pp. 508–515. doi: 10.1016/j.procs.2015.06.058.

[54] Y. Su, Q. Zhang, X. Xu, and Z. Gao, "Quality assessment of speckle patterns for DIC by consideration of both systematic errors and random errors," *Opt Lasers Eng*, vol. 86, pp. 132–142, Nov. 2016, doi: 10.1016/j.optlaseng.2016.05.019.

[55] Z. Sun, J. S. Lyons, and S. R. McNeill, "Measuring Microscopic Deformations with Digital Image Correlation," *Opt Lasers Eng*, vol. 27, no. 4, pp. 409–428, Jul. 1997, doi: 10.1016/S0143-8166(96)00041-3.

[56] C. Franck, S. Hong, S. A. Maskarinec, D. A. Tirrell, and G. Ravichandran, "Three-dimensional full-field measurements of large deformations in soft materials using confocal microscopy and digital volume correlation," *Exp Mech*, vol. 47, no. 3, pp. 427–438, Jun. 2007, doi: 10.1007/s11340-007-9037-9.

[57] M. A. Sutton *et al.*, "Scanning electron microscopy for quantitative small and large deformation measurements Part II: Experimental validation for magnifications from 200 to 10,000," *Exp Mech*, vol. 47, no. 6, pp. 789–804, 2007, doi: 10.1007/s11340-007-9041-0.

[58] X. Li, W. Xu, M. A. Sutton, and M. Mello, "In Situ nanoscale In-plane deformation studies of ultrathin polymeric films during tensile deformation using atomic force microscopy and digital image correlation techniques," *IEEE Trans Nanotechnol*, vol. 6, no. 1, pp. 4–12, Jan. 2007, doi: 10.1109/TNANO.2006.888527.

[59] G. Vendnroux, N. Schmidt, and W. G. Knauss, “Submicron deformation field measurements: Part 3. Demonstration of deformation determinations,” *Exp Mech*, vol. 38, no. 3, pp. 154–160, Sep. 1998, doi: 10.1007/BF02325737.

[60] V. Tiwari, M. A. Sutton, and S. R. McNeill, “Assessment of high speed imaging systems for 2D and 3D deformation measurements: Methodology development and validation,” *Exp Mech*, vol. 47, no. 4, pp. 561–579, Aug. 2007, doi: 10.1007/s11340-006-9011-y.

[61] B. Pan, L. Yu, and D. Wu, “High-Accuracy 2D Digital Image Correlation Measurements with Bilateral Telecentric Lenses: Error Analysis and Experimental Verification,” *Exp Mech*, vol. 53, no. 9, pp. 1719–1733, Nov. 2013, doi: 10.1007/s11340-013-9774-x.

[62] B. Pan, L. Yu, and D. Wu, “High-accuracy 2D digital image correlation measurements using low-cost imaging lenses: Implementation of a generalized compensation method,” *Meas Sci Technol*, vol. 25, no. 2, Feb. 2014, doi: 10.1088/0957-0233/25/2/025001.

[63] B. Pan, L. Yu, D. Wu, and L. Tang, “Systematic errors in two-dimensional digital image correlation due to lens distortion,” *Opt Lasers Eng*, vol. 51, no. 2, pp. 140–147, 2013, doi: 10.1016/j.optlaseng.2012.08.012.

[64] P. Lava, S. Coppieters, Y. Wang, P. Van Houtte, and D. Debruyne, “Error estimation in measuring strain fields with DIC on planar sheet metal specimens with a non-perpendicular camera alignment,” *Opt Lasers Eng*, vol. 49, no. 1, pp. 57–65, Jan. 2011, doi: 10.1016/j.optlaseng.2010.08.017.

[65] S. Ma, J. Pang, and Q. Ma, “The systematic error in digital image correlation induced by self-heating of a digital camera,” *Meas Sci Technol*, vol. 23, no. 2, 2012, doi: 10.1088/0957-0233/23/2/025403.

[66] B. Pan, D. Wu, and Y. Xia, “An active imaging digital image correlation method for deformation measurement insensitive to ambient light,” *Opt Laser Technol*, vol. 44, no. 1, pp. 204–209, Feb. 2012, doi: 10.1016/j.optlastec.2011.06.019.

[67] R. Ravanelli *et al.*, “A new digital image correlation software for displacements field measurement in structural applications,” in *International Archives of the*

Photogrammetry, Remote Sensing and Spatial Information Sciences - ISPRS Archives, International Society for Photogrammetry and Remote Sensing, Jul. 2017, pp. 139–145. doi: 10.5194/isprs-archives-XLII-4-W2-139-2017.

[68] "Zeiss Inspect Correlate Website." Accessed: Oct. 24, 2024. [Online]. Available: https://www.zeiss.co.uk/metrology/products/software/inspect/correlate.html.

[69] "Metrology beyond colors | MatchID | Make metrology count." Accessed: Jan. 13, 2025. [Online]. Available: https://www.matchid.eu/en.

[70] "Correlated Solutions Digital Image Correlation." Accessed: Jan. 13, 2025. [Online]. Available: https://www.correlatedsolutions.com/.

[71] "Industrial Metrology: ZEISS Industrial Quality Solutions." Accessed: Jan. 13, 2025. [Online]. Available: https://www.zeiss.com/metrology/en/home.html.

[72] J. C. A. D. Filho, L. C. S. Nunes, and J. Xavier, "An Open-Source 2D Digital Image Correlation Software: Case Study on the Hyperelastic Behaviour of Silicone-Based Material," 2023, pp. 397–407. doi: 10.1007/978-3-031-29191-3_33.

[73] H. Remesan and M. Ramji, "Adaptation of Open Source 2D DIC Software Ncorr for Solid Mechanics Applications," in *9th International Symposium on Advanced Science and Technology*, New Delhi: Experimental Mechanics, Nov. 2014.

[74] J. Yang and K. Bhattacharya, "Augmented Lagrangian Digital Image Correlation," *Exp Mech*, vol. 59, no. 2, pp. 187–205, Feb. 2019, doi: 10.1007/s11340-018-00457-0.

[75] K. Kumarapu, S. Mesapam, V. R. Keesara, A. K. Shukla, N. V. S. K. Manapragada, and B. Javed, "RCC Structural Deformation and Damage Quantification Using Unmanned Aerial Vehicle Image Correlation Technique," *Applied Sciences (Switzerland)*, vol. 12, no. 13, Jul. 2022, doi: 10.3390/app12136574.

[76] *NCORR* (no date) *Ncorr - File Exchange - MATLAB Central*. Available at: https://uk.mathworks.com/matlabcentral/fileexchange/43130-ncorr (Accessed: 13 January 2025).

[77] J. G. Diez, J. Holtmannspötter, E. Arikan, and P. Höfer, “Combination of scanning electron microscopy and digital image correlation for micrometer-scale analysis of shear-loaded adhesive joints,” *Journal of Adhesion*, 2024, doi: 10.1080/00218464.2024.2370788.

[78] A. Abdelmeguid and M. Trigub, “Pydic: 2D-DIC Code Accuracy Evaluation for Strain Field Measurements,” in *International Conference of Young Specialists on Micro/Nanotechnologies and Electron Devices, EDM*, IEEE Computer Society, 2024, pp. 980–983. doi: 10.1109/EDM61683.2024.10615130.

[79] A. F. Abouellail, Digital image correlation (DIC): Decorrelation problem due to large strains, in *Перспективы развития фундаментальных наук: сборник научных трудов XXI Международной конференции студентов, аспирантов и молодых ученых, г. Томск, 23-26 апреля 2024 г. Т. 7: IT-технологии и электроника* (pp. 6-8), Available: http://earchive.tpu.ru/handle/11683/80460.

[80] J. Winkler and C. Hendy, “Improved structural health monitoring of London’s Docklands Light Railway bridges using Digital image correlation,” *Structural Engineering International: Journal of the International Association for Bridge and Structural Engineering (IABSE)*, vol. 27, no. 3, pp. 435–440, Aug. 2017, doi: 10.2749/101686617X14881937384648.

[81] M. Kalaitzakis, S. R. Kattil, N. Vitzilaios, D. Rizos, and M. Sutton, “Dynamic Structural Health Monitoring using a DIC-enabled drone,” in *2019 International Conference on Unmanned Aircraft Systems (ICUAS)*, IEEE, Jun. 2019, pp. 321–327. doi: 10.1109/ICUAS.2019.8798270.

[82] M. A. Mousa *et al.*, “Application of digital image correlation in structural health monitoring of bridge infrastructures: A review,” Dec. 01, 2021, *MDPI*. doi: 10.3390/infrastructures6120176.

[83] B. Pan, L. Tian, and X. Song, “Real-time, non-contact and targetless measurement of vertical deflection of bridges using off-axis digital image correlation,” *NDT and E International*, vol. 79, pp. 73–80, Apr. 2016, doi: 10.1016/j.ndteint.2015.12.006.

[84] Y. H. Huang, L. Liu, F. C. Sham, Y. S. Chan, and S. P. Ng, “Optical strain gauge vs. traditional strain gauges for concrete elasticity modulus determination,” *Optik (Stuttg)*, vol. 121, no. 18, pp. 1635–1641, Oct. 2010, doi: 10.1016/j.ijleo.2009.03.002.

[85] Z. Jorge, P. Ronny, and O. Sotomayor, “On the digital image correlation technique,” in *Materials Today: Proceedings*, Elsevier Ltd, 2022, pp. 79–84. doi: 10.1016/j.matpr.2021.07.476.

[86] P. Wang *et al.*, “Experimental investigation on the strain-rate effect and inertia effect of closed-cell aluminum foam subjected to dynamic loading,” *Materials Science and Engineering: A*, vol. 620, pp. 253–261, Jan. 2015, doi: 10.1016/j.msea.2014.10.026.

[87] A. M. Pankonien, R. Durscher, J. D. Deaton, A. Piedel, and N. Bhagat, “Multi-material printing integral digital image correlation patterns,” in *2018 Aerodynamic Measurement Technology and Ground Testing Conference*, American Institute of Aeronautics and Astronautics Inc, AIAA, 2018. doi: 10.2514/6.2018-3801.

[88] T. Yu, H. Hyer, Y. Sohn, Y. Bai, and D. Wu, “Structure-property relationship in high strength and lightweight AlSi10Mg microlattices fabricated by selective laser melting,” *Mater Des*, vol. 182, Nov. 2019, doi: 10.1016/j.matdes.2019.108062.

[89] M. R. Vaziri Sereshk, E. J. Faierson, and B. D. Nelson, “Design of experiment and analysis of deformation for compression test of lattices using digital image correlation,” *The International Journal of Advanced Manufacturing Technology*, Dec. 2024, doi: 10.1007/s00170-024-14900-1.

[90] N. Vanderesse, I. Ky, F. Quevedo González, N. Nuño, and P. Bocher, “Image analysis characterization of periodic porous materials produced by additive manufacturing,” *Mater Des*, vol. 92, pp. 767–778, Feb. 2016, doi: 10.1016/j.matdes.2015.12.062.

[91] J. Schindelin et al., “Fiji: An open-source platform for biological-image analysis,” *Nature Methods*, vol. 9, no. 7, pp. 676–682, Jun. 2012. doi:10.1038/nmeth.2019

[92] N. Vanderesse, M. Lagacé, F. Bridier, and P. Bocher, “An Open Source Software for the Measurement of Deformation Fields by Means of Digital Image Correlation,”

Microscopy and Microanalysis, vol. 19, no. S2, pp. 820–821, Aug. 2013, doi: 10.1017/s1431927613006090.

[93] N. Vanderesse, A. Richter, N. Nuño, and P. Bocher, "Measurement of deformation heterogeneities in additive manufactured lattice materials by Digital Image Correlation: Strain maps analysis and reliability assessment," *J Mech Behav Biomed Mater*, vol. 86, pp. 397–408, Oct. 2018, doi: 10.1016/j.jmbbm.2018.07.010.

[94] L. Boniotti, S. Beretta, S. Foletti, and L. Patriarca, "Strain concentrations in BCC micro lattices obtained by AM," in *Procedia Structural Integrity*, Elsevier B.V., 2017, pp. 166–173. doi: 10.1016/j.prostr.2017.11.074.

[95] W. Radlof, C. Benz, and M. Sander, "Numerical and experimental investigations of additively manufactured lattice structures under quasi-static compression loading," *Material Design and Processing Communications*, vol. 3, no. 3, Jun. 2021, doi: 10.1002/mdp2.164.

[96] L. Xiao and W. Song, "Additively-manufactured functionally graded Ti-6Al-4V lattice structures with high strength under static and dynamic loading: Experiments," *Int J Impact Eng*, vol. 111, pp. 255–272, Jan. 2018, doi: 10.1016/j.ijimpeng.2017.09.018.

[97] X. Li *et al.*, "Investigation of compressive and tensile behavior of stainless steel/dissolvable aluminum bimetallic composites by finite element modeling and digital image correlation," *Materials*, vol. 14, no. 13, Jul. 2021, doi: 10.3390/ma14133654.

[98] S. Gothivarekar, S. Coppieters, A. Van de Velde, and D. Debruyne, "Advanced FE model validation of cold-forming process using DIC: Air bending of high strength steel," *International Journal of Material Forming*, vol. 13, no. 3, pp. 409–421, May 2020, doi: 10.1007/s12289-020-01536-1.

[99] E. M. C. Jones, E. Corona, A. R. Jones, W. M. Scherzinger, and S. L. B. Kramer, "Anisotropic plasticity model forms for extruded Al 7079: Part II, validation," *Int J Solids Struct*, vol. 213, pp. 148–166, Mar. 2021, doi: 10.1016/j.ijsolstr.2020.11.031.

[100] A. Peshave, F. Pierron, P. Lava, D. Moens, and D. Vandepitte, “Practical Uncertainty Quantification Guidelines for DIC-Based Numerical Model Validation,” *Exp Tech*, 2024, doi: 10.1007/s40799-024-00758-1.

[101] H. W. Schreier and M. A. Sutton, “Systematic errors in digital image correlation due to undermatched subset shape functions,” *Exp Mech*, vol. 42, no. 3, pp. 303–310, Sep. 2002, doi: 10.1007/BF02410987.

[102] H. Lu and P. D. Cary, “Deformation measurements by digital image correlation: Implementation of a second-order displacement gradient,” *Exp Mech*, vol. 40, no. 4, pp. 393–400, Dec. 2000, doi: 10.1007/BF02326485.

[103] M. Debella-Gilo and A. Kääb, “Sub-pixel precision image matching for measuring surface displacements on mass movements using normalized cross-correlation,” *Remote Sens Environ*, vol. 115, no. 1, pp. 130–142, Jan. 2011, doi: 10.1016/j.rse.2010.08.012.

[104] “VIC-2D Website.” Accessed: Oct. 24, 2024. [Online]. Available: https://www.correlatedsolutions.com/vic-2d

[105] L. Wittevrongel, P. Lava, S. V. Lomov, and D. Debruyne, “A Self Adaptive Global Digital Image Correlation Algorithm,” *Exp Mech*, vol. 55, no. 2, pp. 361–378, Feb. 2015, doi: 10.1007/s11340-014-9946-3.

[106] L. T. Avellar, “Observations of Failure Phenomena in Periodic Media,” CALIFORNIA INSTITUTE OF TECHNOLOGY, Pasadena, 2018.

[107] N. Dixit and P. K. Jain, “Effect of Fused Filament Fabrication Process Parameters on Compressive Strength of Thermoplastic Polyurethane and Polylactic Acid Lattice Structures,” *J Mater Eng Perform*, vol. 31, no. 7, pp. 5973–5982, Jul. 2022, doi: 10.1007/s11665-022-06664-0.

[108] R. Singh, R. Kumar, M. Singh, and P. Preet, “On compressive and morphological features of 3D printed almond skin powder reinforced PLA matrix,” *Mater Res Express*, vol. 7, no. 2, 2020, doi: 10.1088/2053-1591/ab5e61.

[109] D. Qin, L. Sang, Z. Zhang, S. Lai, and Y. Zhao, “Compression Performance and Deformation Behavior of 3D-Printed PLA-Based Lattice Structures,” *Polymers (Basel)*, vol. 14, no. 5, Mar. 2022, doi: 10.3390/polym14051062.

[110] C. Ursini and L. Collini, “Fdm layering deposition effects on mechanical response of tpu lattice structures,” *Materials*, vol. 14, no. 19, Oct. 2021, doi: 10.3390/ma14195645.

[111] M. Palanca, G. Tozzi, and L. Cristofolini, “The use of digital image correlation in the biomechanical area: A review,” 2016, *Taylor and Francis Ltd.* doi: 10.1080/23335432.2015.1117395.

[112] Y. L. Dong and B. Pan, “A Review of Speckle Pattern Fabrication and Assessment for Digital Image Correlation,” *Exp Mech*, vol. 57, no. 8, pp. 1161–1181, Oct. 2017, doi: 10.1007/s11340-017-0283-1.

[113] D. Zhang and D. D. Arola, “Applications of digital image correlation to biological tissues,” *J Biomed Opt*, vol. 9, no. 4, p. 691, 2004, doi: 10.1117/1.1753270.

[114] G. Quino *et al.*, “Speckle patterns for DIC in challenging scenarios: Rapid application and impact endurance,” *Meas Sci Technol*, vol. 32, no. 1, Jan. 2021, doi: 10.1088/1361-6501/abaae8.

[115] D. Pollicelli, M. Coscarella, and C. Delrieux, “RoI detection and segmentation algorithms for marine mammals photo-identification,” *Ecol Inform*, vol. 56, Mar. 2020, doi: 10.1016/j.ecoinf.2019.101038.

[116] L. Liu, P. Kamm, F. García-Moreno, J. Banhart, and D. Pasini, “Elastic and failure response of imperfect three-dimensional metallic lattices: the role of geometric defects induced by Selective Laser Melting,” *J Mech Phys Solids*, vol. 107, pp. 160–184, Oct. 2017, doi: 10.1016/j.jmps.2017.07.003.

[117] F. J. Quevedo González and N. Nuño, “Finite element modelling approaches for well-ordered porous metallic materials for orthopaedic applications: cost effectiveness and geometrical considerations,” *Comput Methods Biomech Biomed Engin*, vol. 19, no. 8, pp. 845–854, Jun. 2016, doi: 10.1080/10255842.2015.1075009.

[118] G. Campoli, M. S. Borleffs, S. Amin Yavari, R. Wauthle, H. Weinans, and A. A. Zadpoor, "Mechanical properties of open-cell metallic biomaterials manufactured using additive manufacturing," *Mater Des*, vol. 49, pp. 957–965, 2013, doi: 10.1016/j.matdes.2013.01.071.

[119] H. Lei *et al.*, "Evaluation of compressive properties of SLM-fabricated multi-layer lattice structures by experimental test and μ-CT-based finite element analysis," *Mater Des*, vol. 169, May 2019, doi: 10.1016/j.matdes.2019.107685.

[120] M. Grasso, L. Azzouz, P. Ruiz-Hincapie, M. Zarrelli, and G. Ren, "Effect of temperature on the mechanical properties of 3D-printed PLA tensile specimens," *Rapid Prototyp J*, vol. 24, no. 8, pp. 1337–1346, Nov. 2018, doi: 10.1108/RPJ-04-2017-0055.

[121] A. Gaweł, S. Kuciel, A. Liber-Kneć, and D. Mierzwiński, "Examination of Low-Cyclic Fatigue Tests and Poisson's Ratio Depending on the Different Infill Density of Polylactide (PLA) Produced by the Fused Deposition Modeling Method," *Polymers (Basel)*, vol. 15, no. 7, Apr. 2023, doi: 10.3390/polym15071651.

[122] T. Shepherd, K. Winwood, P. Venkatraman, A. Alderson, and T. Allen, "Validation of a Finite Element Modeling Process for Auxetic Structures under Impact," *Phys Status Solidi B Basic Res*, vol. 257, no. 10, Oct. 2020, doi: 10.1002/pssb.201900197.

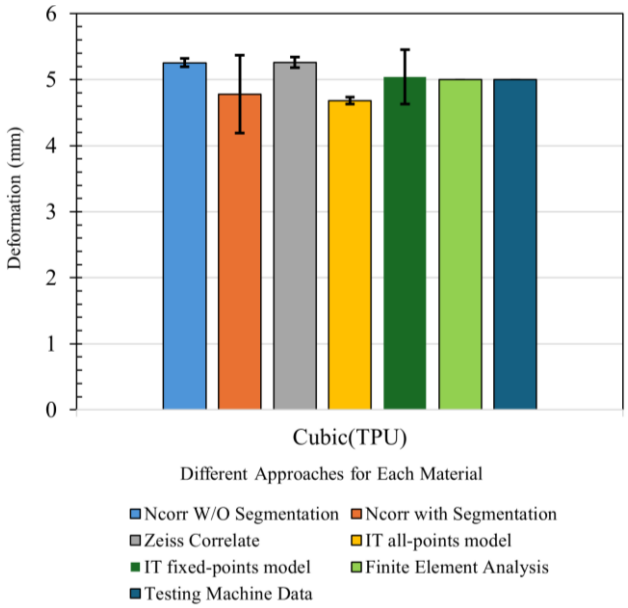
[123] "Ncorr Website." Accessed: Oct. 24, 2024. [Online]. Available: https://www.ncorr.com/

[124] "GOM Software is now Zeiss Inspect." Accessed: Oct. 24, 2024. [Online]. Available: https://www.zeiss.com/metrology/en/software/metrology-software.html#:~:text=Contact-,Same%20solution%2C%20different%20name,for%20metrological%20inspections%20and%20evaluations.

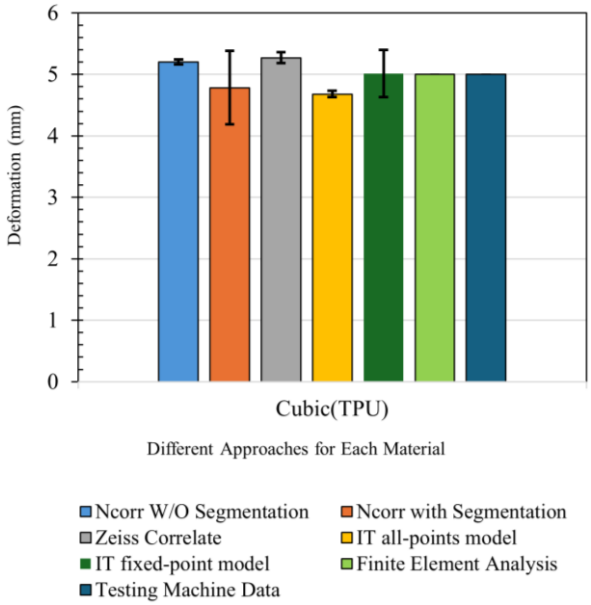
[125] T. Strek and H. Jopek, "Effective mechanical properties of concentric cylindrical composites with auxetic phase," *Phys Status Solidi B Basic Res*, vol. 249, no. 7, pp. 1359–1365, 2012, doi: 10.1002/pssb.201084218.

Appendices

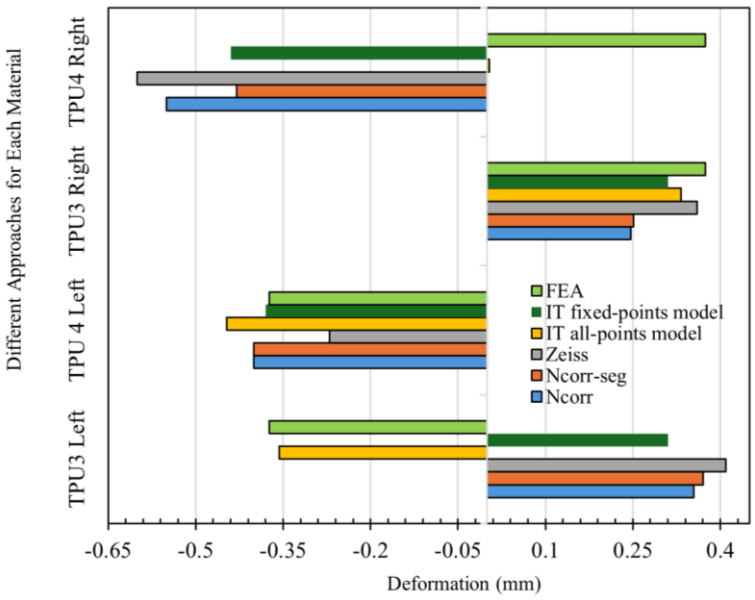
Appendix A: U_x and U_y from Fixed-Points Imaging Technique Model



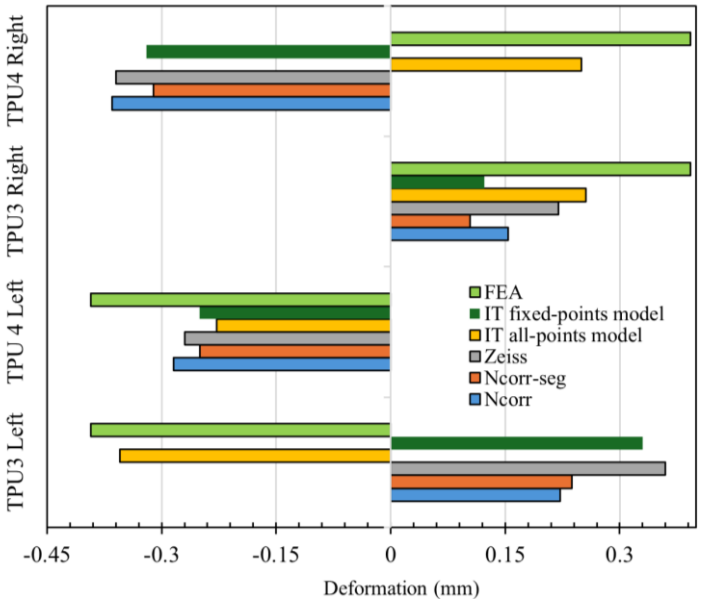
(a) U_y at top midpoint



(b) Average U_y at the top surface



(c) U_x at midpoints of both edges



(d) Average U_x at both edges

Appendix Figure 1: Deformations of Cubic TPU sample using all approaches (including fixed-point model)

Appendix B: Image pre-processing (MATLAB Code)

```
%Create VideoReader Object
v = VideoReader('video_location'); %loads the recorded video of deformation
%Create Image Sequence
n = 1; %Frame number
interval = 100; %interval between each frame while extracting
counter = 0; %This variable keeps track of the number of frames extracted.

while hasFrame(v) %This loop iterates through each frame within the loaded video to
extract.
   img = readFrame(v); %Frame extraction
   if counter == interval
      imwrite(img,strcat('image_', num2str(n), '.tif')); %Saving the extracted frame
      counter = 0;
   end
   counter = counter+1;
   if (n < 4000) %This condition breaks the loop when expected number of frames are
extracted
   n = n+1;
   else
      break;
   end
end
n = n+1;
disp('===images has been extracted from video===');
%%%%%%%%%%%%%%%%%Image Cropping
and  Greyscale%%%%%%%%%%%%%%%%
sampleImg = rgb2gray(imread('image_101.tif')); %Converts RGB image to Gray scale
figure(), imshow(sampleImg);

clc;
close all;
clear all;

%%%%%%%%%%%%%%%%%%%%Image
acquisition%%%%%%%%%%%%%%%%%%%%

ogrImgLoc = 'Z:\ES826\Experiment\22 May 2024\TPU4\*.tif';
cropdImgLoc = 'Z:\ES826\Experiment\22 May 2024\TPU4\TPU4 cropped gray images';
datastore = imageDatastore(ogrImgLoc);
n = 101;
while hasdata(datastore)
    imgName = strcat('image_', num2str(n), '.tif');
    inpImg = imread(imgName);
    processedImg = rgb2gray(inpImg);
   %%%%%%%%%%%%%%%%%%End of Image
acquisition %%%%%%%%%%%%%%%%%%

   %%%%%%%%%%%Image preprocessing%%%%%%%%%%%%%%%
   cropedImg = imcrop(processedImg, [xLoc, yLoc, xWidth, yHeight]); %Crops the image
                                                imwrite(cropedImg,strcat('croppedimage_',
num2str(n), '.tif')); %Saves the cropped image
    if(n <3301)
```

```
        n = n+100;
    else
        break;
    end
end
disp('===images has been cropped===');
%%%%%%%%%%%%%%%%%%%%%End of image
preprocessing%%%%%%%%%%%%%%%%%%%%%
```

Appendix C: Image Segmentation function (MATLAB Code)

```
function segmentedImg = segmentImg(inpImg, cropWindow, rgbCol, segmentThresh) %This
function segments the image and detects the region of interest through background
substraction

    %%%%%%%%%%%%%%%%% Image
preprocessing %%%%%%%%%%%%%%%%%
    segmentedImg = imcrop(inpImg, cropWindow); %Crops the image based on
the
    redImg = segmentedImg(:, :, rgbCol); %Column no for Red = 1, Green = 2, Blue = 3%
    %%%%%%%%%%%%%%%%% End of Image
preprocessing %%%%%%%%%%%%%%%%%

    %%%%%%%%%%%%%%%%%% Image
segmentation %%%%%%%%%%%%%%%%%%
    [row, col] = size(redImg);

    for i = 1 : row %Iterates through the image pixel by pixel.
        for j = 1 : col
            if(redImg(i, j) < segmentThresh) %Threshold to remove background%
                segmentedImg(i, j, :) = 0;
            end
        end
    end
    %%%%%%%%%%%%%%%% End of Image segmentation %%%%%%%%%%%%%%%%
end
```

Appendix D: Imaging Technique Model: Fixed-Points (MATLAB Code)

```
%%%%%%%%%%%%%%%% ROI detection %%%%%%%%%%%%%%%%
cropWindow = [1560, 1025, 830, 800]; %Locations of the object within the image.
colorSpace = 2; %Selection of RGB color space to remove background
thresh = 60; %Threshold of remove background
segmentFlag = 1; %1 to perform image segmentation or 0 otherwise
reflectionindex = 8; %Threshold to remove reflection from image.
calFactor = 50/789; %Calibration factor to convert measurements from pixel to mm
fontSize = 25;

%%%%%%%%% Reference image preparation %%%%%%%%%%
%image acquisition
firstImg = 301; %Reading the undeformed image.
refImg = imread(strcat(datapath, 'image_', num2str(firstImg), '.tif'));
refImg = segmentImg_TPU4(refImg, cropWindow, colorSpace, thresh);
refImg(1 : reflectionindex, :, :) = 0;
% Convert to grayscale if the images are in colour
if size(refImg, 3) == 3
    refImg = rgb2gray(refImg); %Converts RGB image to Gray scale
end
binImg1 = refImg(:, :) > 0; %binarization
%%%%%%%%% End of Reference image preparation %%%%%%%%%%

%Determining points to track in X and Y coordinates.
xloc1 = ceil(width(binImg1)/7);
xloc2 = ceil(width(binImg1)/3);
xloc3 = ceil(width(binImg1)/2);
xloc4 = ceil((width(binImg1)*3)/4.4);
xloc5 = ceil((width(binImg1)*3)/3.5);
xLocs(:,1) = [xloc1, xloc2, xloc3, xloc4, xloc5];

yloc1 = ceil(height(binImg1)/7) + 35;
yloc2 = ceil(height(binImg1)/3) + 30;
yloc3 = ceil(height(binImg1)/2) + 30;
yloc4 = ceil((height(binImg1)*3)/4.4) + 30;
yloc5 = ceil((height(binImg1)*3)/3.5) + 30;
yLocs(:, 1) = [yloc1, yloc2, yloc3, yloc4, yloc5];

counter = 1;
%figure(); %Uncomment this line to visualise changes in real-time.
for imageNo = 301 : 100 : 3301 %Iterating through the dataset
    %%%%%%%%% Image acquisition %%%%%%%%%
    currentImg = imread(strcat(datapath, 'image_', num2str(imageNo), '.tif')); %deformed
image
    %%%%%%%%% End of image acquisition %%%%%%%%%

    %%%%%%%%% Image pre-processing %%%%%%%%%
    if(segmentFlag == 1)
        currentImg = segmentImg(currentImg, cropWindow, colorSpace, thresh); %segmenting
image
    end
    currentImg(1 : reflectionindex, :, :) = 0;
    if size(currentImg, 3) == 3
```

```
        currentImg = rgb2gray(currentImg);
    end
    % Resize the images to the same size if they are different
    if size(refImg) ~= size(currentImg)
        currentImg = imresize(currentImg, size(refImg));
    end
    binImg2 = currentImg(:, :) > 0;
    %%%%%%%% End of image pre-processing %%%%%%%%

    xLocs = findPointLocX(binImg2, xLocs); %Locating X positions in the image
    yLocs = findPointLocY(binImg2, yLocs); %Locating Y positions in the image

    for p = 2 : width(xLocs)
        currentImg = insertMarker(currentImg, [xLocs(:, 1) xLocs(:, p)], "o", Size=10);
        currentImg = insertMarker(currentImg, [yLocs(:, p) yLocs(:, 1)], "x", Size=10);
    end
    currentImg = insertMarker(currentImg, [yLocs(:, p+1) yLocs(:, 1)], "x", Size=10);
    imshow(currentImg);

    %     subplot(2, 2, 1), imshow(currentImg);
    %     xlabel('Width (mm)'), ylabel('Height (mm)'); title('Sample');
    reflectionindex = reflectionindex + 3;

    %posMat is a structure that records the given X and Y axis deformations of all images
    posMat{counter, 1} = imageNo;
    posMat{counter, 2} = xLocs;
    posMat{counter, 3} = yLocs;
    if(counter > 1)
        posMat{counter, 4} = posMat{counter, 2}(:, :) - posMat{1, 2}(:, :); %Height
deformation
        posMat{counter, 5} = posMat{counter, 3}(:, :) - posMat{1, 3}(:, :); %Width
deformation

        posMat{counter, 6} = claculateDistance(xLocs, posMat, counter, 2, calFactor);
        posMat{counter, 7} = claculateDistance(yLocs, posMat, counter, 3, calFactor);

    counter = counter + 1;
end

figure(); %Plotting the deformation measurements

iter = 1;
for i = 2 : height(posMat)
    X = posMat{i, 6}(:, 2 : p);
    Y = posMat{i, 7}(:, 2 : p + 1);
    Z = posMat{i, 1};

    xLocValues = xLocs(iter, 2 : p).*calFactor;
    yLocValues = yLocs(iter, 2 : p  +1).*calFactor;

    [hX, hY] = meshgrid(xLocValues, xLocs(:, 1).*calFactor);
    [wX, wY] = meshgrid(yLocValues, yLocs(:, 1).*calFactor);
```

```
    subplot(1, 2, 1), surf(xLocValues, xLocs(:, 1).*calFactor, X, 'FaceAlpha', 0.2, 'EdgeColor',
'none');
    subplot(1, 2, 2), surf(yLocValues, yLocs(:, 1).*calFactor, Y, 'FaceAlpha', 0.2, 'EdgeColor',
'none');
    iter = iter + 1;
    if (iter > 5)
        iter = 1;
    end
    drawnow;
end
```

Appendix E: Imaging Technique Model: Trace-All-Points (MATLAB Code)

```
%%%%%%%%%%%%%%%% ROI detection %%%%%%%%%%%%%%%%
cropWindow = [1560, 1025, 830, 800]; %Locations of the object within the image.
colorSpace = 2; %Selection of RGB color space to remove background
thresh = 60; %Threshold of remove background
segmentFlag = 1; %1 to perform image segmentation or 0 otherwise
reflectionindex = 10; %Threshold to remove reflection from image.
objWidthPx = 789;
calFactor = 50/objWidthPx;
calRange = objWidthPx/10;
deform = calRange*calFactor; %Calibration factor to convert measurements from pixel to
mm

counter = 1;
figure();
for imageNo = 101 : 100 : 3301 %Iterating through the image dataset
    %%%%%%%%% Image acquisition %%%%%%%%%
    currentImg = imread(strcat(datapath, 'image_', num2str(imageNo), '.tif'));
    %%%%%%%%% End of image acquisition %%%%%%%%%

    %%%%%%%%% Image pre-processing %%%%%%%%%
    if(segmentFlag == 1) %segmenting image
        currentImg = segmentImg_TPU4(currentImg, cropWindow, colorSpace, thresh);
    end
    currentImg(1 : reflectionindex, :, :) = 0;
    if size(currentImg, 3) == 3
        currentImg = rgb2gray(currentImg);
    end

    binImg = currentImg(:, :) > 0; %Binarization
    [y, x]= find(binImg' > 0); %Extracting locations X and Y locations with pixel value 1

    if(counter == 1)
        refImg = currentImg; %Undeformed image

        xLocs(:, counter) = x(:, 1); %X locations of undeformed image
        yLocs(:, counter) = y(:, 1); %Y locations of undeformed image

        x1 = xLocs(:, 1);
        y1 = yLocs(:, 1);
    end
    %%%%%%%%% End of image pre-processing %%%%%%%%%
    if(counter > 1)
        xLocs(:, counter) = xLocs(:, 1); %X locations of deformed image
        yLocs(:, counter) = yLocs(:, 1); %Y locations of deformed image

        points = height(x); %Length on vector X
        xLocs(1 : points, counter) = x(1 : points, 1);
        yLocs(1 : points, counter) = y(1 : points, 1);

        x2 = xLocs(:, counter);
        y2 = yLocs(:, counter);

        %Cosine correlation base distance measurement
```

```
        distX(:, counter) = (x1 + x2) ./ (sqrt(sum(x1.^2)) .* sqrt(sum(x2.^2))); % deformation
in Y
        distY(:, counter) = (y1 + y2) ./ (sqrt(sum(y1.^2)) .* sqrt(sum(y2.^2))); % deformation
in X
        %End of cosine correlation base distance measurement

        dist = distX; yFlag = 0; % For Y deformation.
        dist = distY; yFlag = 1; % For X deformation.

        for i = 1 : height(dist)
            dicImg(xLocs(i, 1), yLocs(i, 1)) = dist(i, counter); %Image reconstruction with
colormap
        end

        end

    reflectionindex = reflectionindex + 2;
    counter = counter + 1;
end

%%%%%%%%%%% Data presentation %%%%%%%%%%%%
deform = 5 %for restructuring
dicImg = rescale(dicImg, 0, deform);
if (yFlag == 0)
    for i = 1 : height(dicImg)
        for j = 1 : width(dicImg)
            if(dicImg(i, j) > 0)
                dicImg2(i, j) = deform - dicImg(i,j);
            else
                dicImg2(i, j) = dicImg(i, j);
            end
        end
    end
else
    dicImg2 = dicImg;
end
figure();
imagesc(dicImg2);
colormap('jet');
xt = get(gca, 'XTick');
set(gca, 'XTick', xt, 'XTickLabel', round(xt*calFactor, 2));
yt = get(gca, 'YTick');
set(gca, 'YTick', yt, 'YTickLabel', round(yt*calFactor, 2));
cb = colorbar;
cb.FontSize = 10;

%%%%%%%%%%% End of data presentation %%%%%%%%%%%%
```